



Cite as

Nano-Micro Lett.
(2023) 15:6

A Rising 2D Star: Novel MBenes with Excellent Performance in Energy Conversion and Storage

Tianjie Xu¹, Yuhua Wang¹ ✉, Zuzhao Xiong¹, Yitong Wang¹, Yujin Zhou¹, Xifei Li^{2,3} ✉Received: 16 August 2022
Accepted: 26 October 2022
© The Author(s) 2022

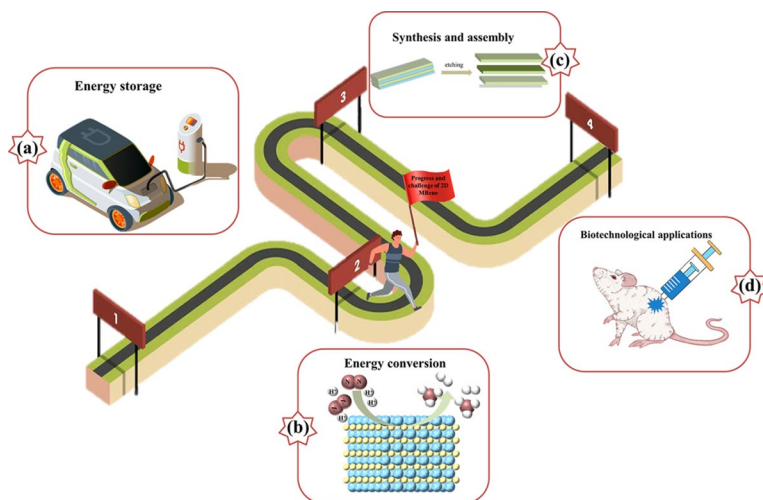
HIGHLIGHTS

- Two-dimensional transition metal borides have high mechanical stability, high charge carrier mobility and great electrochemical performance.
- The potential applications of two-dimensional transition metal borides in the direction of energy conversion and storage have not been systematically reviewed.
- We summarize the research on the role of two-dimensional transition metal borides in catalysis and ion batteries, and put forward the new opportunities in preparation and biotechnology.

ABSTRACT As a flourishing member of the two-dimensional (2D) nanomaterial family, MXenes have shown great potential in various research areas. In recent years, the continued growth of interest in MXene derivatives, 2D transition metal borides (MBenes), has contributed to the emergence of this 2D material as a latecomer. Due to the excellent electrical conductivity, mechanical properties and electrical properties, thus MBenes attract more researchers' interest. Extensive experimental and theoretical studies have shown that they have exciting energy conversion and electrochemical storage potential. However, a comprehensive and systematic review of MBenes applications has not been available so far. For this reason, we present a comprehensive summary of recent advances in MBenes research. We

started by summarizing the latest fabrication routes and excellent properties of MBenes. The focus will then turn to their exciting potential for energy storage and conversion. Finally, a brief summary of the challenges and opportunities for MBenes in future practical applications is presented.

KEYWORDS MBenes; Energy storage and conversion; Catalyst; Anode material; Machine learning



✉ Yuhua Wang, wangyuhua@wust.edu.cn; Xifei Li, xfli2011@hotmail.com

¹ Hubei Province Key Laboratory of Science in Metallurgical Process, Wuhan University of Science and Technology, Wuhan 430081, People's Republic of China

² Institute of Advanced Electrochemical Energy and School of Materials Science and Engineering, Xi'an University of Technology, Xi'an 710048, People's Republic of China

³ Center for International Cooperation On Designer Low-Carbon and Environmental Materials (CDLCEM), Zhengzhou University, Zhengzhou 450001, Henan, People's Republic of China



1 Introduction

The irresistible evolution of human society towards informatization and intelligence puts forward higher requirements for energy storage and transformation. The intermittence and randomness of renewable energy such as solar energy, wind energy, tidal energy and geothermal energy promote the development of energy storage system [1–3]. Electrochemical energy storage is considered as an ideal energy storage method because of its high energy density, high cycle efficiency and flexible application. In many applications involving electronic devices and electric machine [4, 5], the most efficient and practical technology is rechargeable batteries owing to excellent energy efficiency and long cycle life [6–8]. As a major energy storage technology, batteries currently offer high energy density, but their low power density hinders their application in areas where high power is required [9]. The performance of rechargeable batteries depends to a large extent on the composition, structure and properties of their battery materials, especially the anode materials. Therefore, finding high-performance anode materials has become one of the main elements in developing rechargeable batteries.

Among the many electrode materials, two-dimensional (2D) materials are of interest because of their atomic-level thickness, excellent specific surface area, high charge carrier mobility, intriguing chemical activity, and superior

mechanical strength [10–12]. To date, 2D materials have grown rapidly (Fig. 1). Since the discovery of graphene in 2004, graphene has attracted wide attention in the field of energy storage because of its high specific surface area and excellent electrical conductivity, and has shown a wide range of application prospects [13]. However, the zero-band gap of graphene hinders the application of graphene in electronic components. Fortunately, many monoelemental 2D nanosheets have been discovered, such as silicene [14, 15], phosphorene [16, 17], and borophene [18–20]. Especially, the discovery of borophene enriches the physical and chemical properties of boron. As an element adjacent to carbon in the periodic table, boron has strong bonding ability, which is equivalent to carbon. New properties of boron-olefins, such as mechanical flexibility, optical transparency, anisotropic plasma, ultra-high thermal conductivity, 1D near-free electron state, the existence of metal Dirac fermions and superconductivity, have aroused strong theoretical and experimental interest [21–23]. In addition, there are some common 2D materials such as transition metal dichalcogenides (TMDCs) [24, 25], metal oxides [26, 27], nitrides [28], phosphides [29], and 2D gold [30], which has attracted a lot of attention from researchers due to their unique properties. Table 1 shows the class of 2D materials including Xenes (graphene, borophene, phosphorene, silicene, germanene, stanene, etc.), TMCs, 2D TM Oxides, 2D TM Nitrides, 2D TM Phosphides, halides, etc. Recently, transition metal

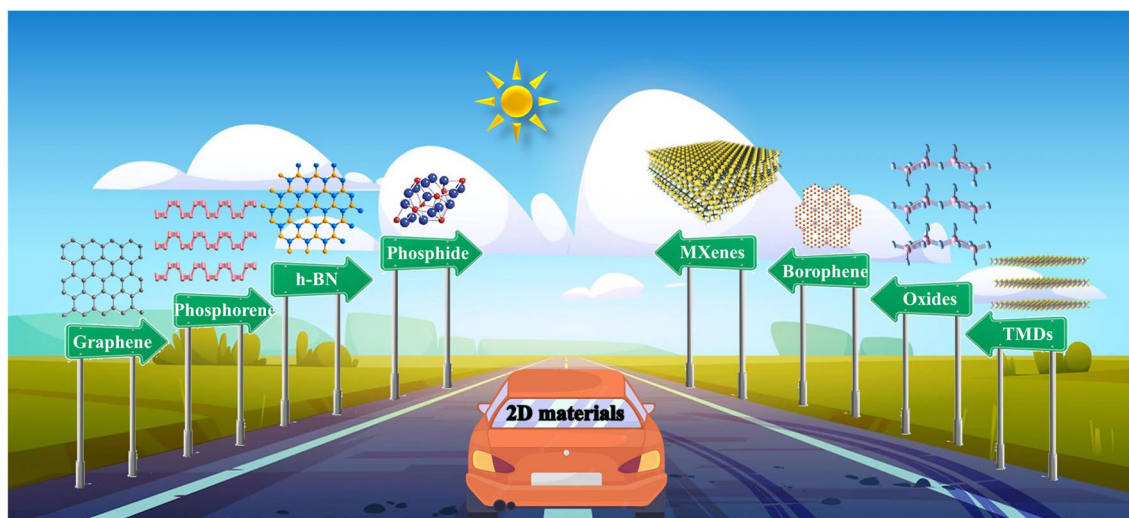


Fig. 1 The rapid development of two-dimensional materials. Reproduced with permission from Ref. [64–69]

Table 1 Classification of 2D materials

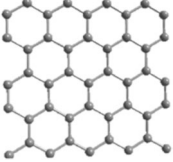
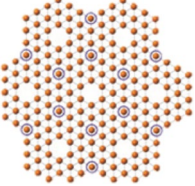
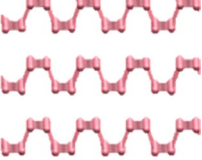
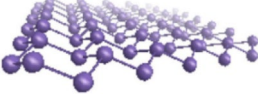
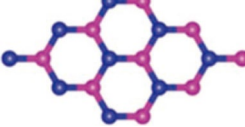
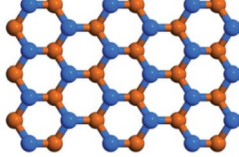
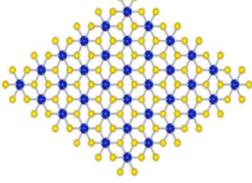
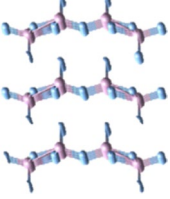
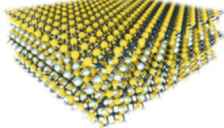
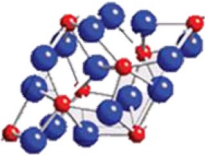
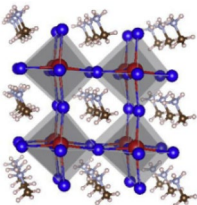
2D materials	Typical representative	Structure	Applications	Refs.
Xenes	Graphene		Lithium storage	[53]
	Borophene		HER	[54, 55]
	Phosphorene		Semiconductors	[16, 17]
	Silicene		Semiconductors	[14, 15]
	Germanene		Phototransistors	[56, 57]
	Stanene		Spintronics	[58]
TMDs	MoS ₂		Semiconductors	[59]
TM Oxides	V ₂ O ₅		Lithium storage	[60]
TM Nitrides	Ti ₃ C ₂		Supercapacitor	[41–45]

Table 1 (continued)

2D materials	Typical representative	Structure	Applications	Refs.
TM Phosphides	Ni ₂ P		HER	[61, 62]
Halides	CH ₃ NH ₃ PbX ₃		Semiconductors	[63]

carbides, nitrides and carbonitrides (MXenes) [31] were first reported as a member in rich family of 2D materials. In general, MXenes are obtained by selectively etching the A atomic layer in MAX phase with hydrofluoric acid, or an acidic solution of fluoride salts [31, 32]. MAX phases can be described with a $M_{n+1}AX_n$ formula, where $n = 1, 2, 3$, M stands for early transition metal, A is an element mostly from groups 13 or 14, X represents carbon and/or nitrogen [33–35]. MXenes have the advantages of large specific surface area, good hydrophilicity, good electrical conductivity and high mechanical strength, and play an important role in energy applications such as supercapacitors (SCs), LIBs and other catalytic processes [36–40]. For example, 2D $Ti_3C_2T_x$ (T_x stands for the surface terminations such as hydroxyl, oxygen, or fluorine) and other MXenes are promising electrode materials for SCs [41–45], LIBs [46, 47] and lithium–sulfur batteries (LSBs) [48, 49] and beyond LIBs [50–52].

With the growing interest in these emerging MXenes materials and the diversity of their parent MAX phase compositions, a variety of MXenes have been produced by different approaches. In addition, there are a series of layered orthogonal transition metal borides with the molecular formula $(MB)_2Al_y(MB_2)_x$ [70] (denoted as MAB phase, M can be Cr, Mo, W, Fe, Mn). Similar to MAX phases, the 2D transition metal borides are called MBenes when the “A” elements are wiped out in the MAB phases. The first article on MBenes dated back to 2015 by Ade and Hillebrecht [70], which identified them as derivatives of MXenes. Many researchers have since conducted theoretical studies

and experimental explorations on the synthesis and application of MBene (Fig. 2a–c, f–h). At the same time, alloying has been shown to be an achievable way to expand the chemical composition in materials with MAX phase. The recently discovered in-plane chemically ordered MAX phase alloy called i-MAX phase is an example [71–73]. A remarkable feature of i-MAX phase is that the two-dimensional MXene obtained by different etching methods can be chemically ordered in plane or vacancy ordered, which has great application prospects for catalysis and energy storage [74–81]. Encouraged by the i-MAX phase discovered earlier, Martin et al. [82] theoretically identified 15 novel MAB phases with in-plane chemical order, called i-MAB phases (Fig. 2d), which shows that alloying is an effective method to expand MAB phase. Zhou et al. [83] report $Mo_{4/3}B_{2-x}T_z$ MBene, produced by selective etching from 3D i-MAB phases in aqueous hydrofluoric (HF) acid (Fig. 2e). Wei et al. [84] studied the possibility of 2D hexagonal V_2B_2 MBene (Fig. 2i) as a promising anode material for sodium ion batteries. Very recently, Xiong and his group [85] prepared two-dimensional MoB with MoAlB as raw material by fluorine-free hydrothermal assisted alkane solution etching (Fig. 2j), and further evaluated the electrochemical performance as anode materials for LIBs.

2D MBenes, although relatively new and being explored, are a very promising family of nanomaterials. Parallel with MXenes, in accordance with calculations, MBenes are applied in energy storage and catalytic reactions. Nevertheless, there is no complete and systematic overview of MBenes’ papers on energy storage and conversion. Guo et al. [86]

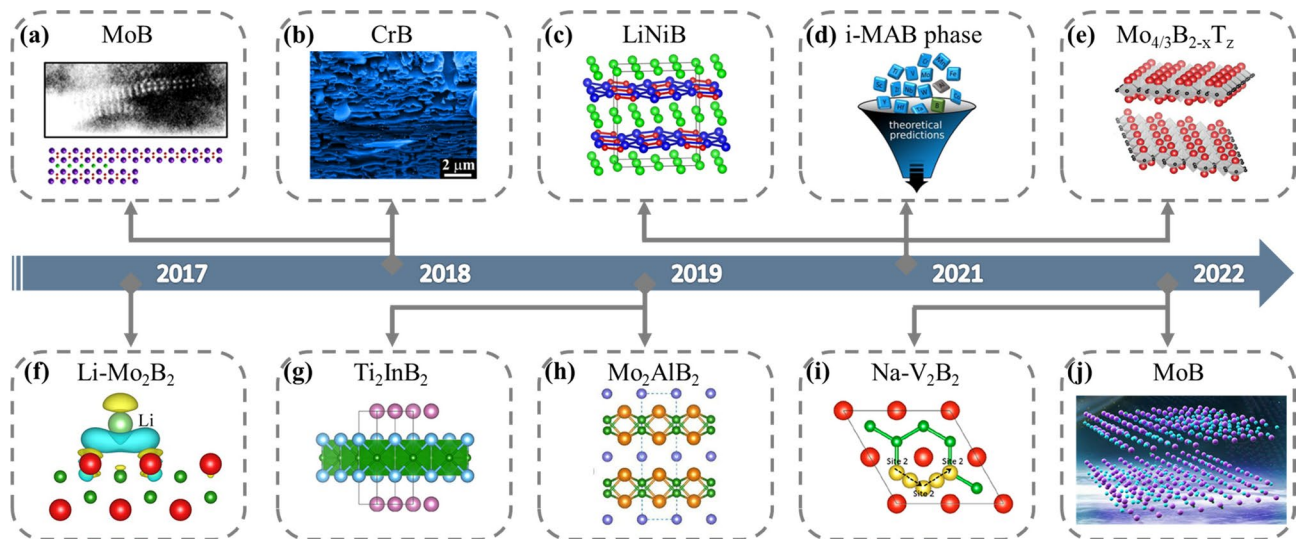


Fig. 2 The representative historical timeline of MBene. **a** Magnification image of the cavity containing the MoB sheets with idealized structure of the delaminated region of the MBene sheets. Reproduced with permission from Ref. [87]. **b** Microstructure of 2D CrB nanosheets prepared by etching for 8 h in dilute HCl solution. Reproduced with permission from Ref. [88]. **c** Crystal structure of *RT*-LiNiB. Reproduced with permission from Ref. [89]. **d** Chemical ordering upon metal alloying of M_2AlB_2 (M from groups 3 to 9) in orthorhombic and hexagonal symmetry with first principles study. Fifteen stable novel phases with in-plane chemical ordering are identified, coined i-MAB. Reproduced with permission from Ref. [82]. **e** The single-layer 2D molybdenum boride sheets with ordered metal vacancies, $Mo_{4/3}B_{2-x}T_z$ (where T_z is fluorine, oxygen, or hydroxide surface terminations). Reproduced with permission from Ref. [83]. **f** The first calculated charge density differences of Mo_2B_2 with one Li atom adsorbed. Reproduced with permission from Ref. [86]. **g** Crystal structure of stable boron-containing ternary phase Ti_2InB_2 . Reproduced with permission from Ref. [90]. **h** The synthesis of Mo_2AlB_2 from MAB phase $MoAlB$ by treatment with LiF/HCl. Reproduced with permission from Ref. [91]. **i** Top view of the Na diffusion path for V_2B_2 indicated by the black dotted arrows. Reproduced with permission from Ref. [84]. **j** 2D MoB MBene from the reaction between $MoAlB$ and NaOH with a fluorine-free hydrothermal-assisted alkane solution etching method. Reproduced with permission from Ref. [85]

firstly studied new MBenes for LIBs via theoretical calculations, such as Fe_2B_2 and Mo_2B_2 . Since then MBenes have also attracted great attention. Therefore, it is now urgent to understand the current progress of MBenes for energy storage and conversion, as well as the further prospects.

In the following, we will present the latest developments in various MBenes materials for applications. The synthesis strategies of MBenes are briefly summarized. In addition, the catalytic properties of MBenes are also mentioned. Then the focus is placed on the applications of 2D MBenes for diverse energy storage devices including lithium-ion batteries (LIBs), sodium-ion batteries (SIBs), potassium-ion batteries (PIBs), magnesium-ion batteries (MIBs) and lithium-sulfur batteries (LSBs) (Fig. 3). Finally, a conclusion

and perspectives on MBenes are provided, and this review is expected to provide some guidance for the design and other related applications of MBenes.

2 Synthesis of MBenes

MBenes seem to be very comparable to MXenes, except that the carbon and/or nitrogen positions have been replaced with boron. However, the MAB-MBenes cannot be directly linked to the corresponding MAX-MXenes combination alone due to the differences in the resulting stoichiometry, the pattern of 2D layer intercalation and structural transitions [96]. Layered MBenes can be obtained from their parental MAB phases using a chemical etching. The MAB phase has

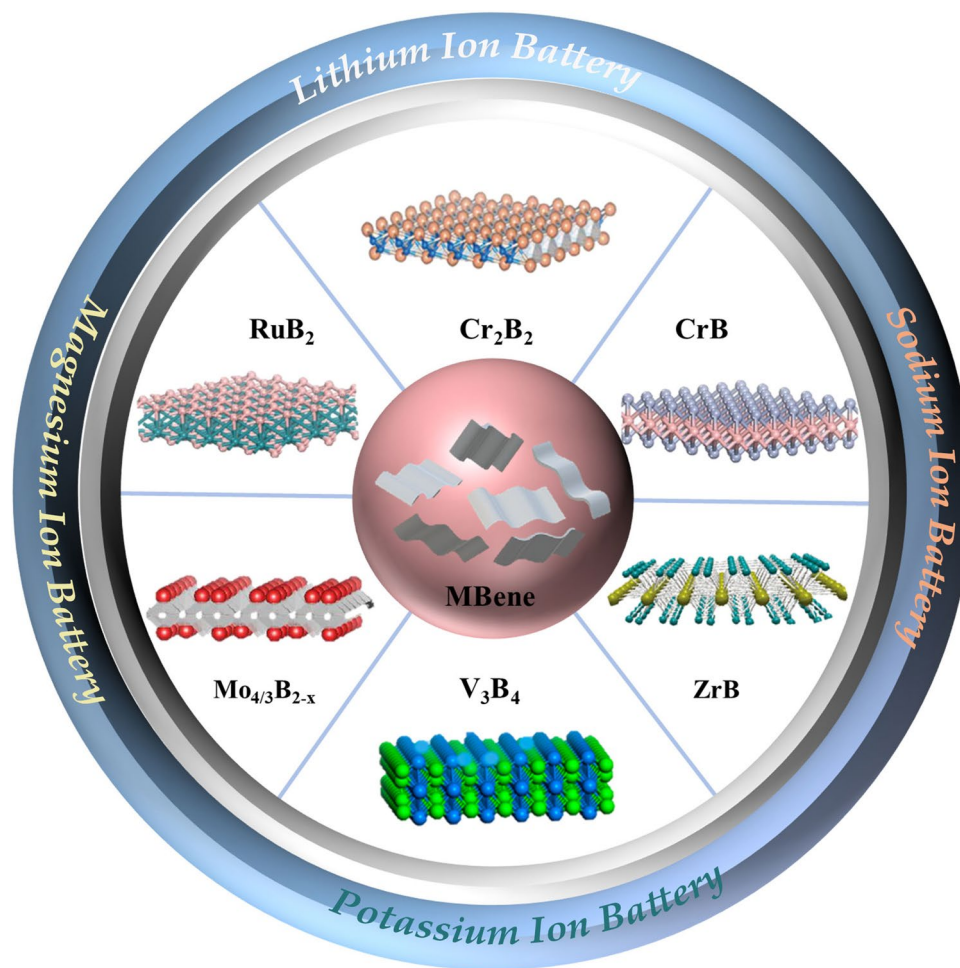


Fig. 3 Schematic diagram illustrating the structure of MBene along with energy storage applications. Reproduced with permission from Refs. [83, 91–95]

different chemical formulas with the related compositions MAB, M_2AB_2 , M_3AB_4 and M_4AB_6 [70]. The M-A bond is metallic, while the M-B bond has mixed covalent/metal/ionic properties and is very similar to M-X in the MAX phase [97]. Thus, by exploiting the difference in bond strength between M-A and M-B bonds, the MAB phase can be exfoliated into 2D MBenes by selective chemical etching of the Al layer, as in the case of isolated MXenes. Based on the above analysis, a possible etching process from the MAB phase to MBene was constructed by Guo et al. [86] (Fig. 4a). It was also shown in terms of lattice dynamics and thermodynamics that the separation of MBene is largely due to the etching of the Al layer.

In etching with fluoride salts with HCl, MXenes are generally synthesized using concentrated HF or their in situ generation. While M-X bonds are covalent-metal-ionic in nature

and have relatively high binding strengths, metallic M-A bonds are relatively weak [32]. In order to find a milder and more durable method for MXenes etching, a more practical method using LiF and HCl solutions was finally proposed [98]. The recent researches on 2D MBenes follow an outstanding exploration to obtain layered, atomically thin 2D MBene flakes. Two different methods for the preparation of 2D MBenes. The first approach used the MAB phase as the starting material, which was treated with acid or basic treatment. The second approach involved the use of bulk powders and their solvothermal fragmentation into specific nanostructures.

In the first approach, the use of MoAIB and Cr_2AlB_2 led to partial and complete etching, resulting in 2D MoB [87, 99] and CrB [88, 100], respectively. In case of MoAIB, the

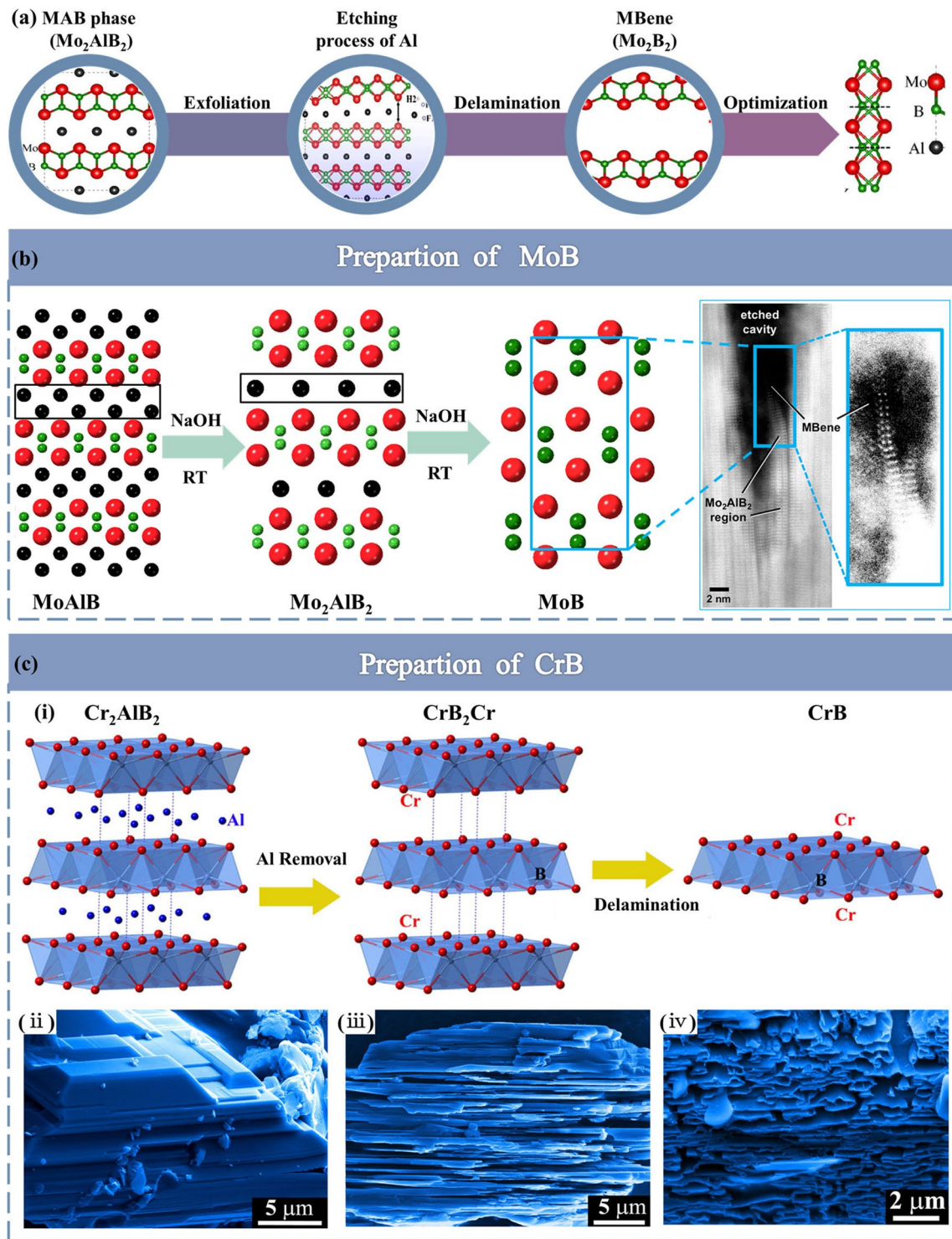


Fig. 4 a Schematic describing the synthesis, delamination and dispersion of Mo_2B_2 based on theory. Reproduced with permission from Ref. [86]. b Synthesis routes for the preparation of MoB. ADF-STEM image of two isolated, delaminated MoB (MBene) sheets inside an etched cavity MoAlB at various stages of etching with 10% NaOH at room temperature. Reproduced with permission from Ref. [87]. c Synthesis routes for the preparation of CrB. (i) A simple 2D model of CrB_2Cr built by removing the Al sheets from Cr_2AlB_2 and separating the adjacent CrB_2Cr units from a vacuum region of about 10 Å. Microstructure of Cr_2AlB_2 powders before (ii) and after (iii) treatment in diluted HCl solution. (iv) 2D CrB nanosheets prepared by etching for 8 h in dilute HCl (1.25 mol L^{-1}) solution. Reproduced with permission from Ref. [88]

Al layer in the MoAlB single crystal was partially etched with NaOH to obtain separated nanothick MoAlB flakes, and these flakes were released to isolate the separate MoAlB sheets (Fig. 4b). However, no typical MoB peaks were found in X-ray diffraction patterns, which indicated that the macroscopic preparation of 2D MoB MBene was a failure. In their study, Lucas et al. [87] investigated a microscopic study of the surface chemical etching of Al from MoAlB single crystals after treatment with NaOH solutions. They found that the exfoliation of Al from MoAlB is accompanied by the formation of high-density (0k0) layer dislocations, which points to alternative ways to prepare MBenes. They observed the appearance of the sub-stable phase Mo_2AlB_2 [86] (space group Cmmm) during the stripping of Al from MoAlB, and Mo_2AlB_2 may be a starting material for the synthesis of 2D MBenes. It was shown that STEM image of two isolated, delaminated MoB (MBene) sheets were accessible. The two MoB monolayers split apart as the stacking faults holding them together were etched, which was feasible to form a stable 2D MoB using this experiment.

While for Cr_2AlB_2 , 2D CrB nanosheets were successfully synthesized by chemical etching of the Al layer in dilute HCl solution at room temperature [88]. Compared to the MAX phase, etching the MAB phase completely into MBenes is not an easy task. Al layer is completely removed after 24 h treatment in MAX phase, and MXene multilayers are formed directly [31]. Zhang et al. [88] reported the synthesis of 2D CrB nanosheets by selective etching Al with Cr_2AlB_2 in hydrochloric acid at room temperature (Fig. 4c-i). In Fig. 4c-ii, the layered structure characteristics of Cr_2AlB_2 microcrystals can be seen, and obvious peeling can be seen after etching in diluted HCl solution for 6 h (Fig. 4c-iii). The researchers also found that when the soaking time was extended to 8 h, most Cr_2AlB_2 particles could be transformed into 2D CrB, and the thickness of the flake became thinner and had a curly shape (Fig. 4c-iv).

Based on recent studies, it is shown that a large number of stable or sub-stable 2D structures can be formed using Ti and B [101–104]. Different from MAB structures with orthorhombic symmetry, Ti_2InB_2 displays hexagonal $\overline{\text{P6m2}}$ symmetry. Wang et al. [90] successfully synthesized Ti_2InB_2 by solid-phase reaction based on the theoretical prediction, and then the layered TiB compound was obtained by high-temperature de-alloying and de-indium. In general, the synthesis process consists of placing the Ti_2InB_2 sample into a quartz tube under dynamic vacuum. The optimized condition

for the dealloying reaction was determined to be 1050 °C for 6 days, which is too complicated and time consuming. In this process, diluted HCl (2 mol L⁻¹) was applied for 10 h to remove any impurities (e.g., Ti_3In , Ti_3In_4 , $\text{Ti}_{2.2}\text{In}_{1.8}$). According to the XRD diagram of the product, the hexagonal TiB phase ($\overline{\text{P6m2}}$) could not be obtained due to the harsh reaction conditions. On the contrary, another stable layered TiB phase (CMCM) with orthogonal groups was formed. At the same time, a tiny TiB phase containing another orthogonal group (Pnma) was formed (Fig. 5a). The SEM image on the left side of Fig. 5b showed the prepared Ti_2InB_2 , and the layered structure can be clearly seen. The middle picture showed that the main removal product is TiB compound (CMCM) with orthogonal structure, which acted as impurity phase together with TiB_2 in the prepared Ti_2InB_2 . The SEM image on the right shows that TiB has smaller particle size than parent phase, but still has layered structure, which indicates that the original layered structure has changed during high temperature dealloying.

Recently, a new group of MAX phases was discovered with ordered quaternary [105–111], which expands MAX phases and opens a new window for tuning the nature of MAX phases and developing new MXenes. For example, Caspi et al. [106] showed by high-resolution neutron diffraction analysis that the $(\text{Cr}_{0.5}\text{V}_{0.5})_{n+1}\text{AlC}_n$ system showed a strong tendency for V and Cr atoms to be ordered, with V occupying only the intermediate layer. So far, only eight stable MAB phases have been synthesized experimentally: $(\text{CrB}_2)_n\text{CrAl}$ ($n = 1, 2, 3$) [70], Cr_4AlB_4 [112], Fe_2AlB_2 , Mn_2AlB_2 [113–116], MoAlB, and WAlB [112, 116–118]. In consideration of the above, Dai et al. [119] chose Cr_4AlB_4 to study possible ordered quaternary phases and predicted nine new stable ordered quaternary MAB phases ($\text{M}_2\text{M}'\text{AlB}_4$ phases, $\text{M} = \text{Mn, Fe, Co}$ and $\text{M}' = \text{Cr, Mo, W}$). Based on the prediction of the stability of the ordered $\text{M}_2\text{M}'\text{AlB}_4$ phase, researchers hope to synthesize new ordered quaternary MAB phases, which will greatly enrich the MAB phase family and expand its potential application prospects. Inspired by the finding of Ti_2InB_2 and the previous discovery of the i-MAX phase, Martin et al. [82] identified 15 new MAB phases with planar chemical ordering, called i-MAB phases, which is considered to be thermodynamically stable at a temperature of at least 2000 K. The researchers also synthesized $\text{Mo}_{4/3}\text{Y}_{2/3}\text{AlB}_2$ and $\text{Mo}_{4/3}\text{Sc}_{2/3}\text{AlB}_2$, confirming a structure displaying the characteristic in-plane chemical ordering of Mo and Y or Sc.

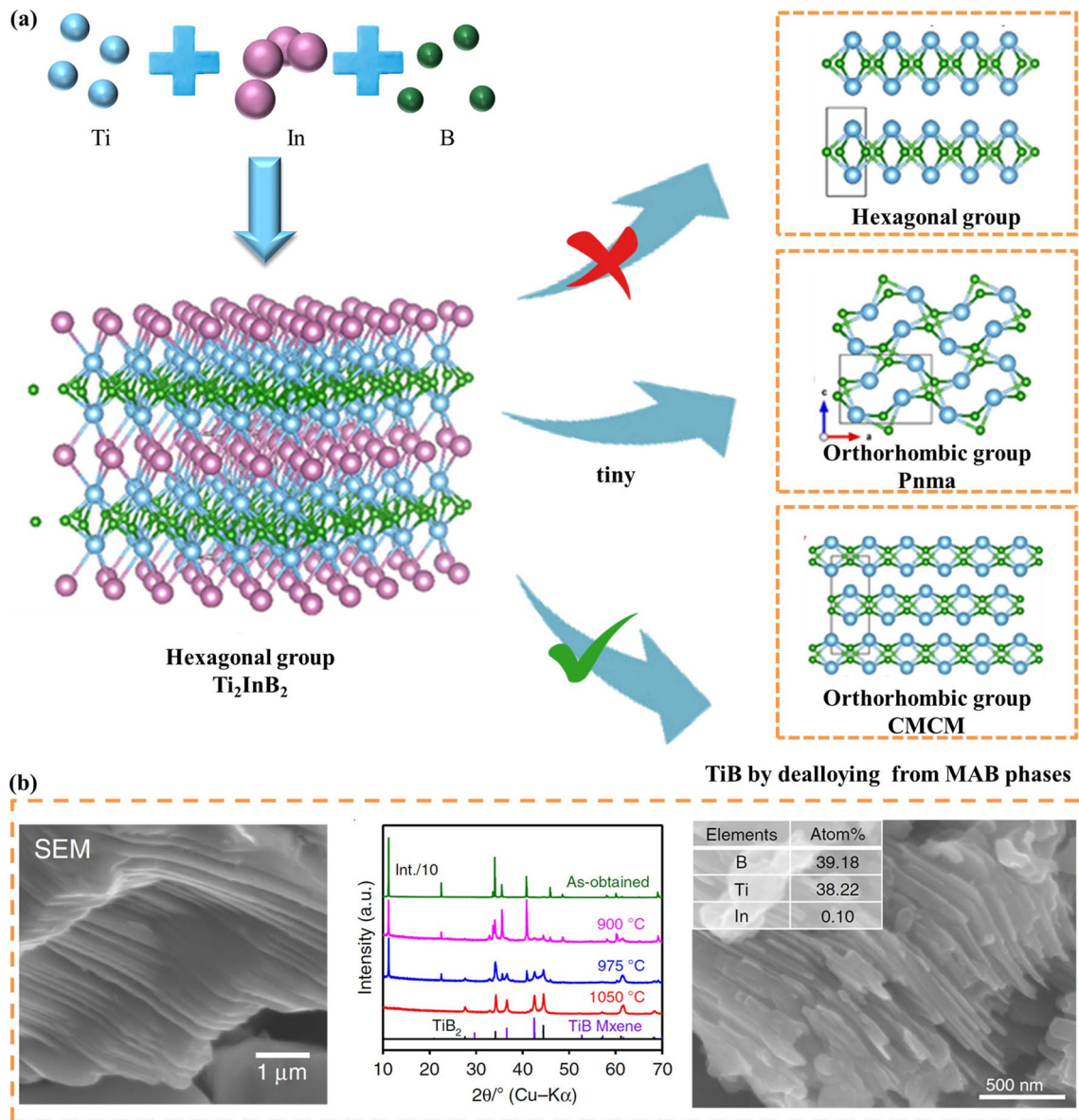


Fig. 5 **a** Proposed the generated crystal structures from the parent Ti_2InB_2 phase by dealloying. **b** Left: SEM image of a particle showing a laminated structure. Middle: XRD patterns for samples prepared by exposure of as-obtained Ti_2InB_2 powder to a vacuum (about 10^{-4} Pa) as a function of the temperature after 6 days. Right: Typical SEM image of the TiB phase; inset shows the atomic ratio for this sample. Reproduced with permission from Ref. [90]

Attempts to fabricate 2D MBenes have been challenging due to the reactivity of the boride phases and the tendency of the parent material to dissolve rather than selectively etch. A similar method was used by Zhou et al. to produce single-layer 2D MBenes with ordered metal vacancies, $Mo_{4/3}B_{2-x}T_z$ [83]. A $Mo_{4/3}B_{2-x}T_z$ film was obtained by HF etching of $(Mo_{2/3}Y_{1/3})_2AlB_2$ or $(Mo_{2/3}Sc_{1/3})_2AlB_2$, followed

by TBAOH intercalation and delamination (Fig. 6a). The precursors were prepared by solid-state reaction sintering of Mo/Y/Al/B powder mixtures in a tube furnace, showing rietveld refinement of the sample with composition of $(Mo_{2/3}Y_{1/3})_2AlB_2$ (Fig. 6b). The precursor phases are the in-plane ordered i-MAB structure. The XRD results of the powders before and after etching showed that the peak

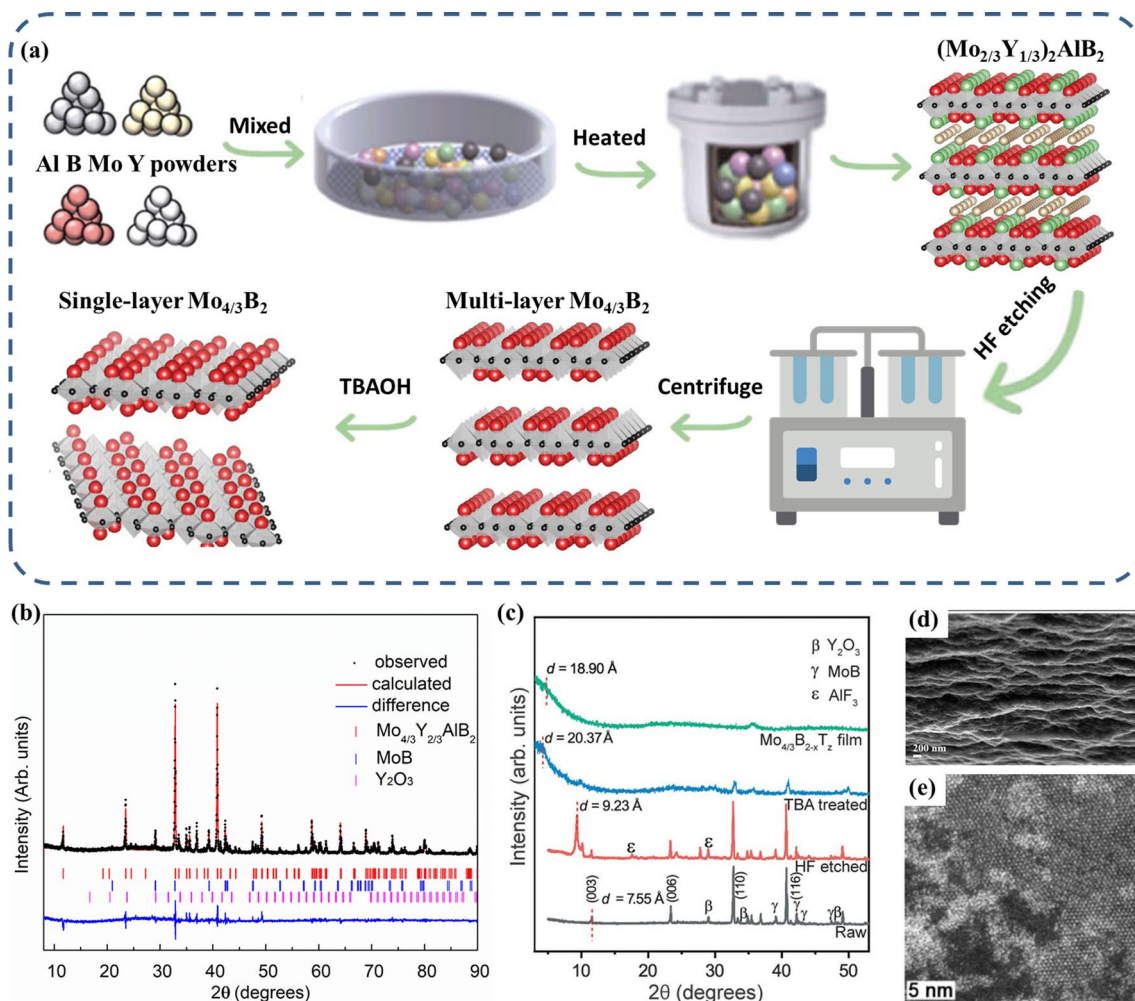


Fig. 6 **a** Schematic of the synthesis of 3D $(\text{Mo}_{2/3}\text{Y}_{1/3})_2\text{AlB}_2$ and transformation process from i-MAB to 2D boridene with the schematic atomic structure. **b** Rietveld refinement of the sample with nominal composition of $(\text{Mo}_{2/3}\text{Y}_{1/3})_2\text{AlB}_2$. **c** XRD pattern of $(\text{Mo}_{2/3}\text{Y}_{1/3})_2\text{AlB}_2$ before (black) and after (red) HF and after TBAOH intercalation (blue) and delamination (green). **d** SEM image showing the cross section of a $\text{Mo}_{4/3}\text{B}_{2-x}\text{T}_z$ film. **e** STEM image of single-layer $\text{Mo}_{4/3}\text{B}_{2-x}\text{T}_z$ sheet. Reproduced with permission from Ref. [83]. (Color figure online)

strength of $(\text{Mo}_{2/3}\text{Y}_{1/3})_2\text{AlB}_2$ decreased obviously after etching, and the strength of some impurities such as Y_2O_3 , Al_2O_3 and AlF_3 decreased obviously after TBAOH treatment (Fig. 6c). The average flake size of MBene was relatively small (50 nm), but the layered structure and stacked flake morphology can be observed from the SEM image of the cross section of the filter membrane (Fig. 6d, e). This MBene may be slightly deficient in B compared to the parent phase, and x can be as high as ~ 0.5 . The surface termination T_z was determined to be a mixture of O, OH, and F with z in the range of 2 to 3. 2D $\text{Mo}_{4/3}\text{B}_{2-x}\text{T}_z$ sheets can be prepared by a top-down approach and achieved in highly concentrated suspensions. Their results proved the feasibility of the top-down method of chemically peeling layered compounds and

provided a principle for the further preparation of abundant MBenes. A large number of 2D MBenes with similar structures are also expected to be prepared by this method.

The preparation methods of MBenes described above all have some disadvantages (such as complex preparation process and high pressure), and there is no practical application in these works. In addition, due to the serious corrosiveness and toxicity of hydrofluoric acid, it is not recommended to use the same hydrofluoric acid etching strategy typically commonly used to manufacture MXene, so the preparation by Zhou et al. [83] has not been applied to large-scale experiments. Xiong et al. [85] recently reported a green and safe method to fabricate MBene from precursor, so as to promote the application research of MAB. They used a

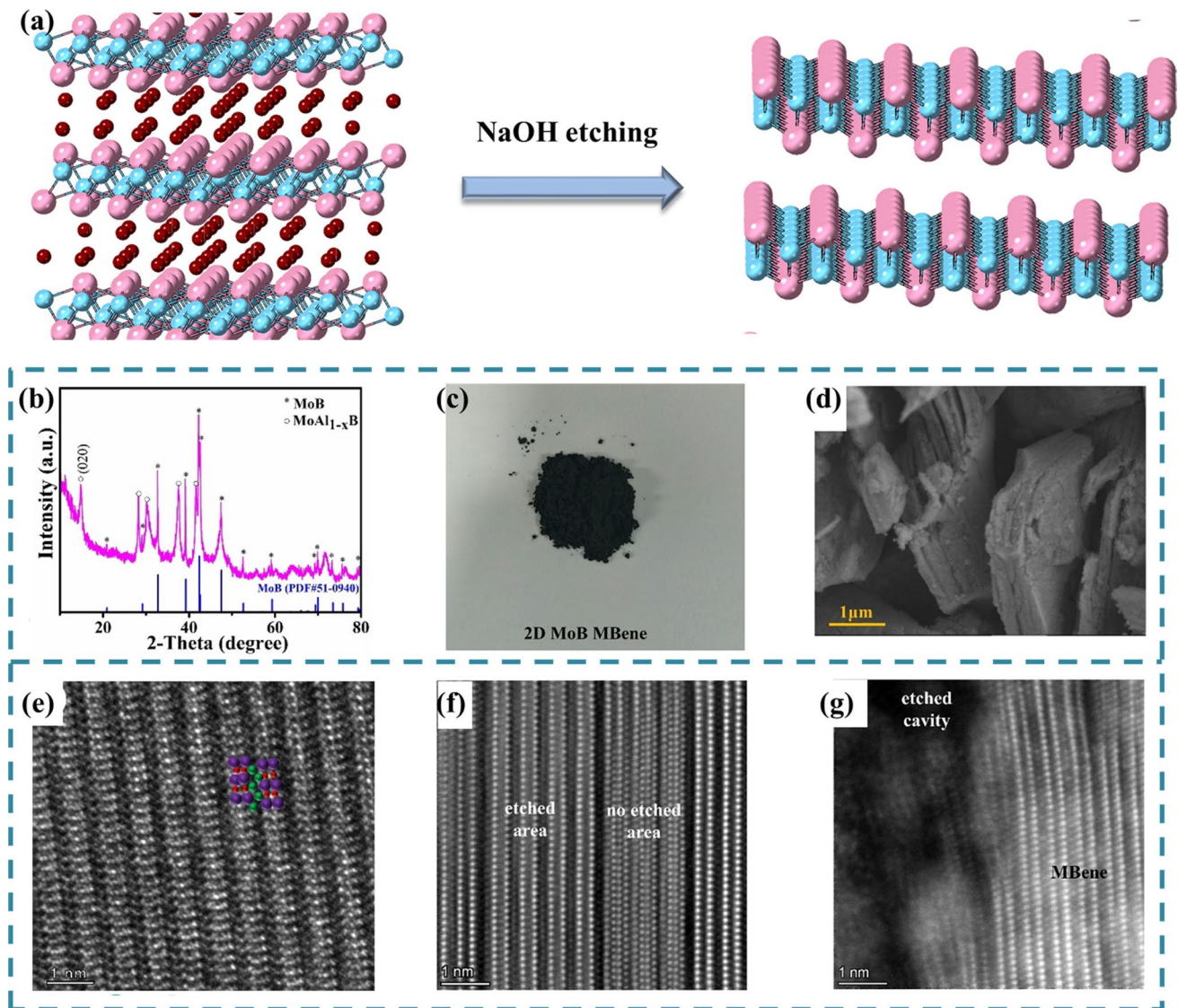


Fig. 7 **a** Schematic of the synthesis of 2D MoB MBene from MoAlB phases. **b** XRD patterns of 2D MoB MBene. **c** Optical images of 2D MoB MBene powders. **d** SEM images of 2D MoB MBene. Atomic scale resolution ADF-STEM image of **e** MoAlB, **f**, **g** 2D MoB MBene

hydrothermal-assisted alkane solution etching method to prepare MoB from MoAlB (Fig. 7a) and verified the excellent performance of MBenes as anode material for LIBs for the first time.

From X-ray diffraction peaks (Fig. 7b), we can also know that MoB has been successfully prepared, but some Al still exists. After characterization and analysis of the samples, the researchers found that the MoB particles were obtained after etching showed a clear accordion-like layered structure similar to MXene materials, as shown in Fig. 7c, d. In addition, the researchers found that when

the reaction temperature was raised to 160 °C, the product was particles instead of the previous layered structure, and only a small amount of MoAl_{1-x}B was observed, which indicated that a certain amount of Al atoms had a stable effect on maintaining the accordion-like layered structure. The microstructures of MoAlB and MBene were observed by annular dark field scanning electron microscope (Fig. 7e-g). When aluminum atoms are removed, 2D MoB can be observed from the etched region, but some regions are still not etched, and the end region of the wafer presents an etched style. Xiong et al. [85] successfully

prepared two-dimensional MoB wafers by hydrothermal assisted alkane solution etching, which opened the door for the future study of MBenes. Moreover, the samples obtained by using fluorine-free etchants have high safety, which is beneficial to the application in experiments. It is expected that more two-dimensional MBenes can be successfully prepared and put into experimental application by this method.

In the other case, researchers utilize bulk powders and their solvent thermal fragmentation into specific nanostructures, such as MgB₂ [120], MnB [121], ZrB₂ [93], and GdB₆ [122]. For example of MnB, Jin et al. [121] obtained MnB nanosheets (MBN) being a mixture of MnB₂ and MnB phases. This method was based on oxidative acidic etching of manganese boride under microwave assistance, improving previous MAB etching difficulties [31]. This process requires the use of two etching agents CH₃COOH and 30% H₂O₂. The mixture was heated to 160 °C for 2 h in a microwave reactor, washed, surface modified with hyaluronic acid (HA), and sonicated for 1 h. The addition of Bi³⁺ to the reaction system during etching is probably to result in the formation of bonds between boron and bismuth, forming double-anchored MnB₂/MnB nanosheets (MBBN).

Table 2 summarizes the recent findings regarding the experimental synthesis of 2D MBenes. MoB can be successfully prepared using a fluorine-free hydrothermal assisted alkane solution etching strategy, providing a green strategy for exploring a new family of MBene materials for different applications. However, compared to MXenes preparation methods, MBenes is only in its infancy and more preparation methods need to be investigated to obtain high quality 2D MBenes.

3 Unique Properties of MBenes

Boron shows great diversity in chemical properties. Boron atom is located in the left adjacent position of carbon atom, and has *sp*² orbital hybridization very similar to carbon element. Compared with carbon, boron lacks only one electron, which has attracted wide attention because of its lack of electrons. The complexity of boron stems from its electronic structure: boron has three valence electrons, which is easy to show the trend of building with other boron atoms, thus forming complex clusters and cage structures. Recently, by introducing B as X element, we are familiar with some ternary borides similar to MAX phase, called MAB phase. The MAB phase has various chemical formulas (i.e., MAIB, M₂AIB₂, M₃AIB₄ and M₄AIB₆) and various structures of atomic network structures with orthogonal crystals. In MAB phases MAIB, M₂AIB₂ and M₃AIB₄, boron atoms form one-dimensional isolated serrated chains perpendicular to A layer, while in M₃AIB₄ and M₄AIB₆, double and triple chains of boron atoms are connected together to form flat bands with hexagonal ring network.

Inspired by the significant success in energy storage and ion transport of MXenes etched from MAX phases, great efforts have been poured into the theoretical calculations of 2D MBenes within years. The MBenes studied by researchers now include orthorhombic system and hexagonal system. According to the calculation of total energy and fretting elasticity, the researchers predicted that MBenes with orthogonal group might transform into hexagonal structure after stripping. Generally speaking, the MBenes we study now can be divided into two types of chemical formulas. One is MB or M₂B₂ phase, and the other is M₂B phase. Usually, MB phase is studied more than M₂B phase. For a class of

Table 2 Summary of the most recent findings regarding the experimental synthesis of 2D boride phases

MBenes	Precursors	Etching methods	Etching conditions	Surface groups	Refs.
MoB	MoAlB	10% NaOH	RT, 24 h	–	[87]
CrB	Cr ₂ AlB ₂	1.25 M HCl	RT, 6 h	–OH	[100]
Mo _{4/3} B _{2-x}	(Mo _{2/3} Y _{1/3}) ₂ AlB ₂ or (Mo _{2/3} Sc _{1/3}) ₂ AlB ₂	40%wt HF	RT, 210 min	–O, –OH, –F	[83]
MoB	MoAlB	25% NaOH	150 °C, 24 h	–	[85]
TiB	Ti ₂ InB ₂	Dealloying	1050 °C, 6 d	–	[90]
ZrB	ZrB ₂	H ₂ O ₂ and acetic acid	–	–	[93]

MB MBenes, which are predicted by theory, they have good structural stability and excellent mechanical properties. In order to understand the mechanical properties of MBenes, the researchers calculated the elastic constants, Poisson's ratio, shear modulus of elasticity and Young's modulus of MBenes. MBenes have higher elastic modulus values than other 2D materials. And there are calculations that prove that the presence of surface end groups enhances the mechanical properties they produce. As with MBenes, surface termination is predicted to make MXenes mechanically stiffer than the associated pristine MXenes. The shear modulus value is the response of the material to shear stress, with larger (smaller) shear modulus values indicating the stiffness (softness) of the system to cutting [103]. Calculations of the shear modulus generally indicate that larger forces are required to deform in MBenes that are terminated by oxygen or fluorine, while the pristine MBenes will be deformed by smaller forces. In other terms, pristine MBenes are typically more ductile than functionalized MBenes. Therefore, like MXenes, it is predicted that surface terminations make MBenes stiffer.

Besides, phonon spectroscopy is widely used to verify the lattice dynamics stability of crystal structures. If no imaginary frequency is observed in the Brillouin zone, this indicates that 2D MBenes are dynamically stable. Jia et al.

[92] computed the vibrational spectra of 2D MBene structures based on density generalized theory to evaluate the thermodynamic stability of monolayers V_2B_2 , Cr_2B_2 and Mn_2B_2 . During the AIMD simulations, the free energy of the monolayer MBenes showed slight oscillations, confirming the thermodynamic stability at 350 K. The mechanical properties of MBenes monolayers were described by calculating Young's modulus and Poisson's ratio, and the results showed that 2D V_2B_2 , Cr_2B_2 and Mn_2B_2 have isotropic and ultra-high Young's modulus. Table 3 gives the stability of some MBenes. This result confirms that MBenes has good mechanical stability and processability. In summary, MBenes have great potential to exhibit beneficial mechanical properties that are comparable to or better than other 2D nanomaterials.

Khaledialidusti et al. [103] have systematically investigated the electronic structures of the hexagonal monolayer of pristine and functionalized MB MBenes ($M = Sc, Ti, Zr, Hf, V, Nb, Ta, Mo, \text{ and } W$) with F, O, or OH groups. The pristine 2D MB MBenes can be simply regarded as a 2D honeycomb boron layer doped with transition metals. In order to better understand the electronic structure of primitive and functionalized 2D MBenes, the researchers also considered their projected band structures. All the pristine MBenes are metallic, and the metal conductivity is determined by the

Table 3 Stabilities of MBenes

MBenes	Stabilities of MBenes					
	a (Å)	b (Å)	ΔE_{hull} (eV/atom)	E/atom (eV)	C_{2D} (N m ⁻¹)	h/l (10 ⁻⁴)
CrB	2.86952	2.93991	1.09	- 7.95679	251.23	1.24
MnB	2.86378	2.90075	0.87	- 7.79661	215.30	1.34
FeB	2.81997	2.78483	0.79	- 7.38663	198.60	1.41
ZrB	3.06595	3.25166	0.68	- 8.11756	191.26	1.52
MoB	3.02255	3.03284	1.18	- 8.66739	233.68	1.48
HfB	3.05277	3.20715	0.77	- 8.68925	237.84	1.74
WB	3.02418	3.02115	1.30	- 9.398	239.41	1.80
FeB ₂	3.14451	2.99459	0.83	- 6.99438	143.76	1.56
RuB ₂	3.46777	3.04861	0.76	- 7.43697	181.82	1.61
OsB ₂	3.50288	3.0146	0.80	- 7.9858	218.63	1.81
Mo ₂ B	2.84587	2.84587	1.29	- 9.15321	216.94	1.63
Au ₂ B	3.00307	2.99245	0.93	- 3.94874	85.52	2.70
Nb ₅ B ₂	5.91928	5.91926	0.88	- 9.25488	208.04	1.63
V ₃ B ₄	2.92227	2.99264	0.72	- 8.26231	395.05	1.23
Nb ₃ B ₄	3.03301	3.18588	0.70	- 8.80826	314.89	1.51
Ta ₃ B ₄	3.01463	3.18065	0.77	- 9.36285	341.17	1.80



delocalized metal d state. In addition, since the degree of hybridization between atomic orbitals in B-B bond is relatively greater than that in M-B bond, it can be expected that B-B bond is stronger than M-B bond. It can be seen from the projected band structure that there are few transitions in the metal band below Fermi level compared with the boron-related band. Therefore, in 2D MB MBenes, it is generally expected that the M-M bond will be weaker than the B-B bond and the M-B bond. By comparing the projected band structure of MBF, MBOH and MBO with the pristine MB, it can be recognized that F, OH or O have higher electronegativity than the transition metals studied, and these termination groups affect the electronic structure. Due to the saturation of F, one or two bands are effectively free near Fermi energy. Since both the F and OH chemical groups need an electron to completely fill their valence layers, the electronic structures of F and OH terminated MBenes are generally similar. In the case of O termination, the M d band becomes vacant, which also reduces metallicity.

The following content, we introduce the recent development of MBenes with attractive performance for catalyst and rechargeable batteries in this review.

4 Excellent Performance of MBenes in Energy Conversion

Energy conversion is one of the most vital issues related to the sustainable development of society. Therefore, one of the partial methods is to electrocatalyze a large number of substances to produce useful chemicals, such as electrocatalytic water splitting (to produce hydrogen) and nitrogen reduction (to produce ammonia) [123, 124]. The water splitting via the hydrogen evolution reaction (HER) in the presence of a catalyst is an effective and safe method for hydrogen production. Currently, Pt and Pt compounds are the most widely used catalysts, while the rarity and high cost of Pt limit their application in industrial scale [125–128]. Therefore, it is necessary to find non-precious and economical catalysts. In recent years, various 2D materials have been widely used in multiphase catalysis due to their large specific surface area and high stability, such as MoS₂ [129–131], MXenes [132–135] and heteroatom-doped graphene [136–139]. Researchers have also focused their attention on the properties of 2D MBenes derived from MAB phases. 2D MBenes have been explored as rising candidates in the

area of catalysis including HER, oxygen evolution reactions (OER), water splitting, and nitrogen evolution reactions, among many others (Fig. 8).

4.1 MBenes-based Electrocatalysts for HER

Guo's group [86] calculated the Gibbs free energy of Mo₂B₂ and Fe₂B₂, which indicates the potential HER catalytic activity of Fe₂B₂. The electrocatalytic HER activity of a class of 2D MBenes was investigated using the free energy of hydrogen adsorption by Liu et al. [144]. The calculated ΔG_{H}^* values for Fe₂B₂ monolayers under full H coverage are very close to the results reported by Guo et al. [86]. It is noteworthy that the Mn₂B₂ monolayer also exhibits excellent performance with a smaller $|\Delta G_{\text{H}}^*|$ value. The calculated results showed that the HER catalytic activity of Mn₂B₂ and Fe₂B₂ is comparable to that of Pt. Due to the high HER activity of Ti₃C₂O₂ and Nb₄C₃O₂ MXenes [145], Zhang et al. [146] investigated the importance of multilayer MBenes for electrocatalytic performance (Fig. 9a). They reported a new collection of MBenes: Cr_{n+1}B_{2n} (n = 1–3), with excellent structural stability, metal conductivity, high Young's modulus and catalytic activity. Considering the similarity between MAX phase and MAB phase, Cr-based Cr_{n+1}B_{2n} MBenes are expected to be etched from parent phase Cr_{n+1}AlB_{2n} (Fig. 9b). Based on the 2 × 2 supercell, the researchers calculated that at low H coverage (1/4 ML), Cr₂B₂, Cr₃B₄ and Cr₄B₆ showed their catalytic activities with ΔG_{H} of –0.198, –0.178, and –0.078 eV (catalytic activity is higher than Pt (0.09 eV) [147–151], respectively. When their HER catalytic activities at high H coverage (1/2 to 1 ML) were further investigated, Cr₂B₂ and Cr₃B₄ exhibited catalytic inertia. In contrast, for Cr₄B₆ exhibited near-zero $|\Delta G_{\text{H}}|$ at all considered H coverages, which is expected to be an excellent HER catalyst (Fig. 9d). Furthermore, Li et al. [152] investigated newly discovered TiB MBene towards its catalytic activity for HER. Notably, TiB sheets display a weak nucleus-free two-dimensional electron gas in free space (2DEG-FS), which can potentially be used for electronic devices with low barrier electron transport channels. They discovered oxygen-covered 2D TiB exhibited comparable catalytic performance on HER to the oxidized MXene [145, 147, 153]. The main process is shown in Fig. 9c. It was shown that bare TiB is not a suitable electrocatalyst for HER. However, this situation can be significantly improved by surface oxygen

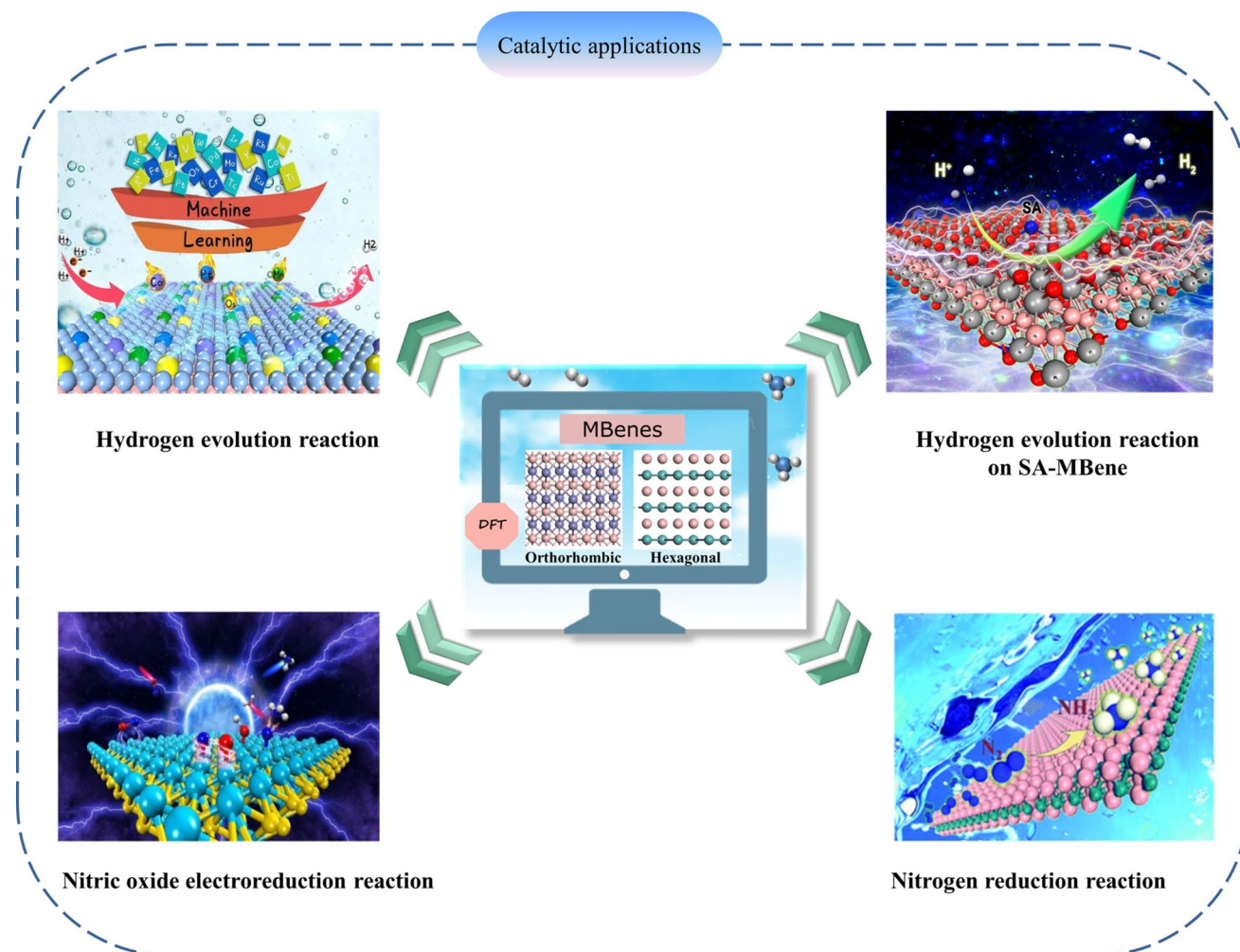


Fig. 8 Applications of MBene as catalyst. Reproduced with permission from Refs. [140–143]

termination (Fig. 9e). O surface is a favorable active center for H-binding, with near-zero H adsorption free energy.

It has been proved in theory that MBenes has excellent performance as HER catalyst, and the experimental study of MBenes further confirms the theory. Alameda et al. [99] studied the HER activity of MoAlB crystal before and after etching, and found that the overpotential of etched MoAlB single crystal was 301 mV at the current density of 10 mA cm^{-2} , which was significantly reduced by 99 mV compared with 400 mV of unetched crystal. The reason is that the etching of interlayer Al exposes the base surface and

all edges, which increases the surface area of the exposed catalytically active base surface, so the activity of HER is significantly improved. In addition, Helmer's team [154] studied the potential of $2\text{D Mo}_{4/3}\text{B}_{2-x}\text{T}_z$ as cathode catalyst material to produce electrochemical hydrogen through HER in acidic medium. After continuous cycling and 67 h constant current experiment, the activity of HER increased significantly at -10 mA cm^{-2} , and the initial voltage moved to -0.15 V relative to RHE. This is an impressive number for non-Pt materials. We also compare the catalytic activity of MBenes with that of typical MXenes in Table 4.

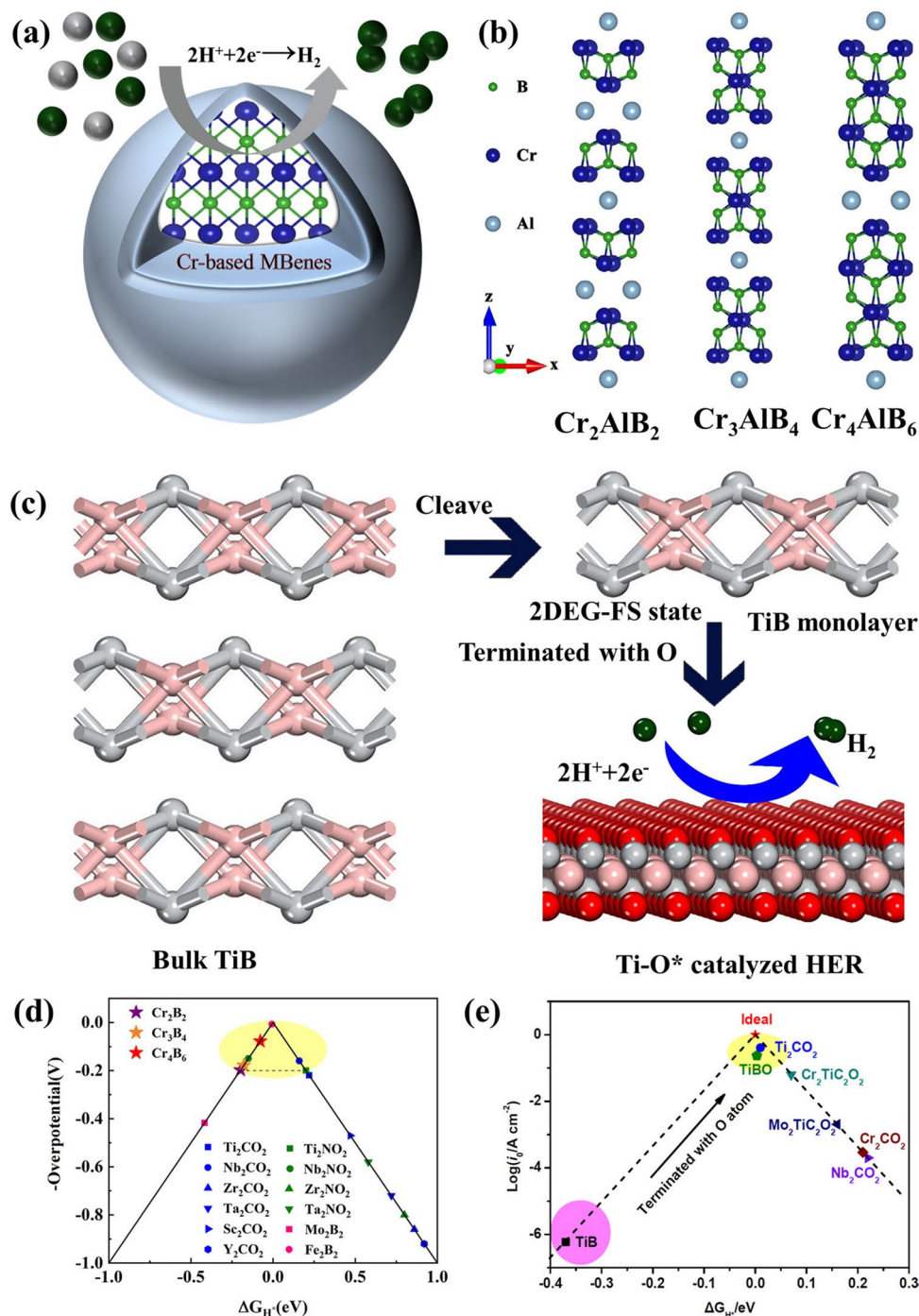


Fig. 9 **a** Schematic illustration of the reaction pathways of hydrogen evolution reaction on the $\text{Cr}_{n+1}\text{B}_{2n}$ catalyst surface. **b** Crystal structures of Cr_2AlB_2 , Cr_3AlB_4 and Cr_4AlB_6 . Reproduced with permission from Ref. [146]. **c** Sketch of the HER process catalyzed by TiB; The TiB monolayer cleaved from bulk TiB for the study of electronic properties and reactivity; The TiB layer with surface functionalization for HER. Reproduced with permission from Ref. [152]. **d** HER volcano curve of $\text{Cr}_{n+1}\text{B}_{2n}$ (stars) compared with some previously reported MXenes and MBenes at H coverage of 1/4 ML. Reproduced with permission from Ref. [146]. **e** The calculated exchange current ($\log i_0$) plotted as a function of H^* adsorption free energy on different MXenes/MBenes. Reproduced with permission from Ref. [152]

Table 4 Summary of MBenes and MXenes HER electrocatalysts from recent reports

Catalyst	Electrolyte	Overpotential at 10 mA cm ⁻² (mV)	Tafel slope (mV dec ⁻¹)	Refs.
MoAlB not etched	0.5 M H ₂ SO ₄	400	85	[99]
MoAlB etched	0.5 M H ₂ SO ₄	301	68	[99]
Mo _{4/3} B _{2-x} T _z	0.5 M H ₂ SO ₄	–	241	[154]
Ti ₃ C ₂ T _x flakes	0.5 M H ₂ SO ₄	385	188	[155]
Mo ₂ CTx	1 M H ₂ SO ₄	230	–	[156]

4.2 MBenes-based Electrocatalysts for NRR

Ammonia (NH₃) is one of the important raw materials for the synthesis of chemicals and fertilizers and plays a vital role in our life [157]. Metal catalysts (e.g., Fe and Ru) have

been widely used in industrial nitrogen reduction reactions (NRR), but their efficiency is severely limited by the highly competitive nature of the side reactions [158, 159]. Electrocatalytic nitrogen reduction reaction (eNRR) with simple and controllable operating conditions and low energy consumption is an ideal alternative to the Haber–Bosch process [160]. However, because of the slow activation of chemically inert N≡N triple bonds, this electrochemical process is currently limited by poor reaction kinetics and high overpotential [161–165]. It is well known that the HER process is a competitive process with NRR in electrocatalytic denitrification [166–168]. Therefore, it is crucial to inhibit the HER reaction on the catalyst surface when selecting a catalyst [169]. So far, the search for a desirable electrocatalytic eNRR process with high Faraday efficiency (FE) and low overpotential is still a challenging task [170].

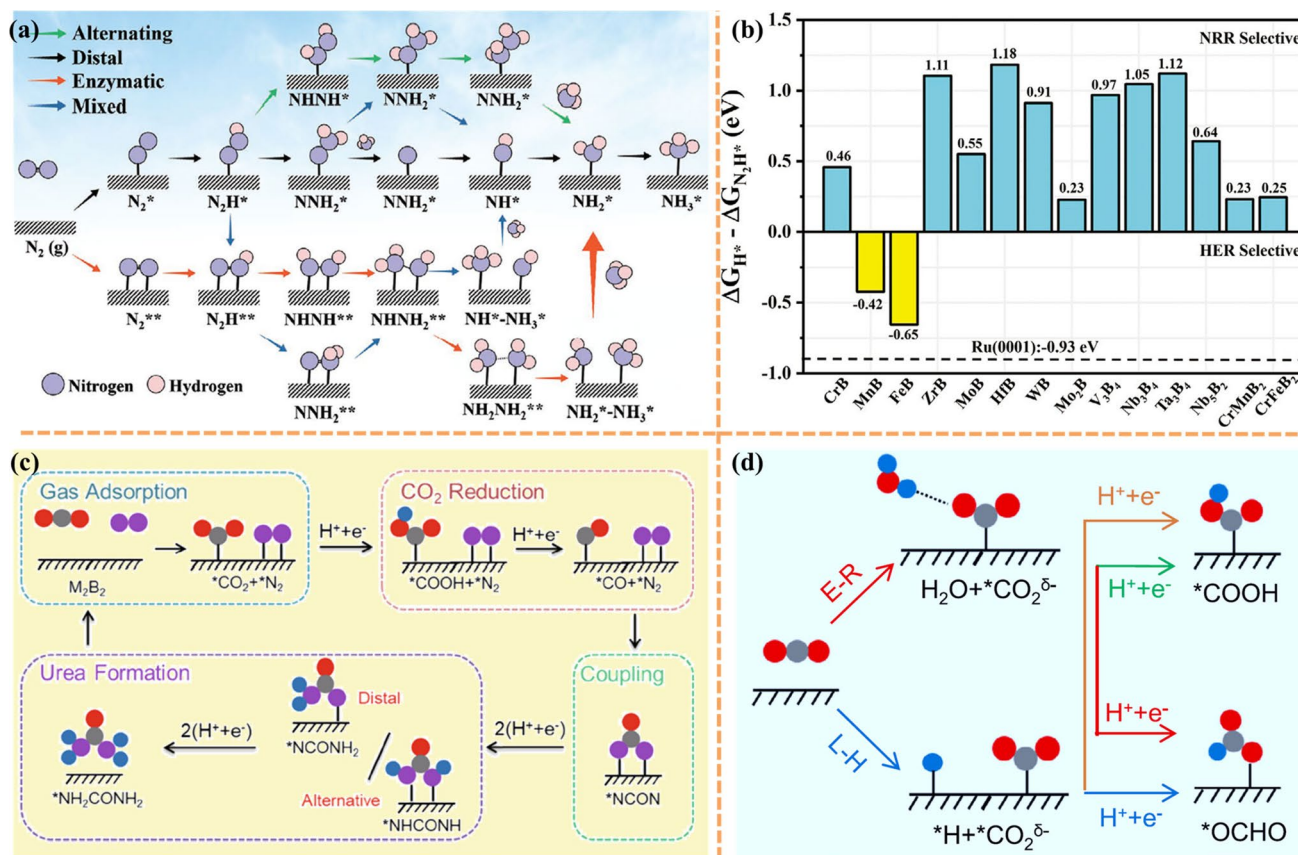


Fig. 10 **a** Schematic illustration of the reaction pathways of nitrogen reduction reaction on the catalyst surface. **b** The free energy differences of H⁺ and N₂H⁺ (ΔG_{H⁺} - ΔG_{N₂H⁺}) on the 14 MBenes. The corresponding value on Ru (0001) surface is given for comparison. Reproduced with permission from Ref. [171]. **c** Reaction mechanism. Schematic diagram of the mechanism of urea production through the electrochemical coupling of N₂ and CO₂. The gray, red, pink, and blue balls represent C, O, N, and H atoms, respectively. **d** Selectivity of CO₂ electroreduction. Schematic diagram of the ER and LH mechanisms of CO₂ electroreduction to *COOH or *OCHO. Reproduced with permission from Ref. [172]. (Color figure online)

In order to find qualified catalysts with both high specific activity and large active surface area, Guo et al. [171] predicted that a set of stable 2D MBenes can be considered as a defect-free, dopant-free nitrogen immobilized electrocatalyst by comprehensive density functional theory (DFT) calculations. Schematic diagram of the reaction pathway of NRR on the catalyst surface is shown in Fig. 10a. MBenes with their different chemical compositions and well-defined surface structures, both in exposed boron and exposed metal locations, are ideal models for studying this mechanism. Their study determined that seven MBenes (CrB, MoB, WB, Mo₂B, V₃B₄, CrMnB₂ and CrFeB₂) not only have intrinsic basal plane activity for NRR with limiting potentials between -0.22 and -0.82 V, but also have a strong ability to inhibit competitive HER. In addition, the researchers also used the free energy difference of H^{*} and N₂H^{*} to evaluate the catalytic selectivity of MBenes, and the changes of values on 14 MBenes were compared with those of Ru (Fig. 10b). Especially, unlike MXenes surface oxidation to close the active center [173–178], MBenes, once oxidized, can catalyze NRR through a self-activation process to reduce O^{*}/OH^{*} to H₂O^{*} under the reaction conditions, which facilitates the electroreduction of N₂. Particularly, CrMnB₂ reached a record level of theoretical activity with a limiting potential of -0.22 V. Qi et al. [179] demonstrated the feasibility of a class of MBenes as NRR electrocatalysts. All MBenes are metallic and exhibit electron-like features, which can facilitate the activation of N₂ gas. TiBene, YBene, ZrBene and WBene have low NRR overpotential (<0.7 V) and follow a direct dissociation mechanism. They also proposed that the MBenes work function can be used as a descriptor of NRR catalytic activity, providing a feasible strategy for the design of efficient NRR electrocatalysts. The catalytic performance of 2D MBenes (including FeB₂, RuB₂, OsB₂, V₃B₄, Nb₃B₄, Ta₃B₄, CrB, MnB, ZrB and HfB) for NRR was recently explored by ab initio calculations by Yang et al. [142]. Calculations showed that MBenes have high stability in aqueous environment and good selectivity for NRR without HER. Both surface boron atoms and metal atoms of MBenes can be used as active centers. Interestingly, MBenes with surface B atoms as active centers (FeB₂, RuB₂ and OsB₂) exhibit higher NRR reactivity than MBenes with metal active centers higher NRR reactivity. Li et al. [180] calculated the electrocatalytic activity of six MB (M = Sc, Ti, V, Cr, Mo and W) monolayers for NRR using the first principle calculation. Calculations showed

that N₂ molecules can be stably adsorbed on the surface of MB monolayers, except for VB monolayers in the end-face configuration, which can trigger the NRR process. The results showed that the monolayers of VB, CrB and MoB have good catalytic activity for NRR and are expected to be NRR electrocatalysts.

A similar method was taken by Wang et al. [181] to study Mo₂B₂ as a catalyst for the NRR reaction by DFT calculation. In their work, the possible active centers of nitrogen adsorption were explored in the constructed two-dimensional Mo₂B₂ model. For the adsorption of N₂ molecules on 2D Mo₂B₂ with three different stable structures (vertical, inclined, and horizontal adsorption), the electronic and bonding properties of these different structures were investigated to explore their catalytic activity and NRR pathways. Finally, HER on 2D Mo₂B₂ was investigated with a limiting potential of 0.57 V. This suggests that Mo₂B₂ can effectively promote the NRR reaction while inhibiting the HER reaction. Similarly, Lin and co-workers [182] searched the catalytic properties of Cr₂B₂ for NRR. In this work, four favorable structures were selected, including N₂ adsorbed on B-B bonds, Cr-B bonds, and the top site of B and Cr atoms. The results showed that N₂ adsorption on Cr-B bond with lateral structure has a maximum adsorption energy of -1.235 eV and good catalytic activity with a limiting potential of 0.29 V. Xiao et al. [183] performed a theoretical screening of the catalytic activity in the electrochemical NRR of MBenes using a density flooding theory approach. By considering stability, activity and selectivity, Ta₃B₄, Nb₃B₄, CrMnB₂, Mo₂B₂, Ti₂B₂ and W₂B₂ exhibit the lowest limiting potential and can activate N₂ molecular protonation, which suggests that these MBenes can be used as candidate catalysts for NRR. Excitingly, the coplanar oxidation, which has a great impact on the catalytic properties of NRR catalysts, can be solved by the potential difference between the redox potential (UR) and the limiting potential (UL) in this work. Among them, W₂B₂, Mo₂B₂ and Ta₃B₄ are promising negative resistance catalysts with the ultimate potentials of -0.24 , -0.43 , and -0.39 V, respectively.

Urea is the first organic compound to be produced from inorganic raw materials and is the most commonly used nitrogen fertilizer in the world [184, 185]. In addition, urea has important uses in everyday production, such as reducing the purity of NO_x in exhaust gases, and synthesizing barbiturates [186–189]. Currently, industrial urea production is mainly accomplished by reacting NH₃ and CO₂ at

high temperatures and pressures. However, this approach is not only relatively energy intensive, but also relies on some multi-cycle processes to improve the conversion efficiency [190]. While NH_3 mainly comes from the artificial nitrogen reduction reaction, we have also briefly described above the defects in NRR. Due to the adjustable lamellar structure and good electrical conductivity of MBenes, Zhu et al. [172] linked the possibility of direct coupling of N_2 and CO_2 for urea production on some specific MBenes. The electrochemical coupling of N_2 and CO_2 to urea can be classified as four stages: adsorption of N_2 and CO_2 , reduction of $^*\text{CO}_2$ to $^*\text{CO}$, coupling of $^*\text{N}_2$ and $^*\text{CO}$ to $^*\text{NCON}$, hydrogenation of $^*\text{NCON}$ to urea (Fig. 10c). They also systematically investigated the potential of three MBenes as electrocatalysts for urea synthesis, Mo_2B_2 , Ti_2B_2 and Cr_2B_2 . All three molecular sieves are able to adsorb N_2 and CO_2 on their substrates and the adsorbed CO_2 is readily reduced to $^*\text{CO}$. It is noted that compared with 2D Mo_2B_2 and Cr_2B_2 , Ti_2B_2 transforms to $\text{Ti}(\text{OH})_3$ in the high pH region when the applied potential is -0.65 V, indicating that Ti_2B_2 is susceptible to corrosion under the operating conditions of urea synthesis. Therefore, 2D Ti_2B_2 has low electrochemical stability and is not a satisfactory catalyst for the synthesis of urea. The selectivity

of CO_2 reduction is basically controlled by kinetics, and the formation of $^*\text{COOH}$ and $^*\text{OCHO}$ can be realized by accepting H atoms in water through Eley–Rideal (ER) mechanism or by accepting H atoms bound to the surface through the Langmuir–Hinshelwood (LH) mechanism (Fig. 10d). For this reason, the researchers also calculated that the formation of $^*\text{COOH}$ species requires a large energy barrier, so CO_2 will be mainly reduced to $^*\text{CO}$ instead of format. This article provides a bright pathway for the design of catalysts for the simultaneous immobilization of N_2 and CO_2 for urea synthesis, providing additional experimental and theoretical support for the development of 2D electrocatalysts for this challenging reaction.

Recently, machine learning (ML) combined with DFT calculations has become a powerful tool for the design and screening of novel catalysts [191–194] (Fig. 11). The development of ML has accelerated with the collection of massive datasets, making ML a popular tool for material discovery [195, 196]. The key issue in the accuracy of ML models is the way in which the input data is encoded. Therefore, the accurate representation (descriptor) of input data is very important in ML. A good descriptor usually includes a wide range of geometry, structure and chemical

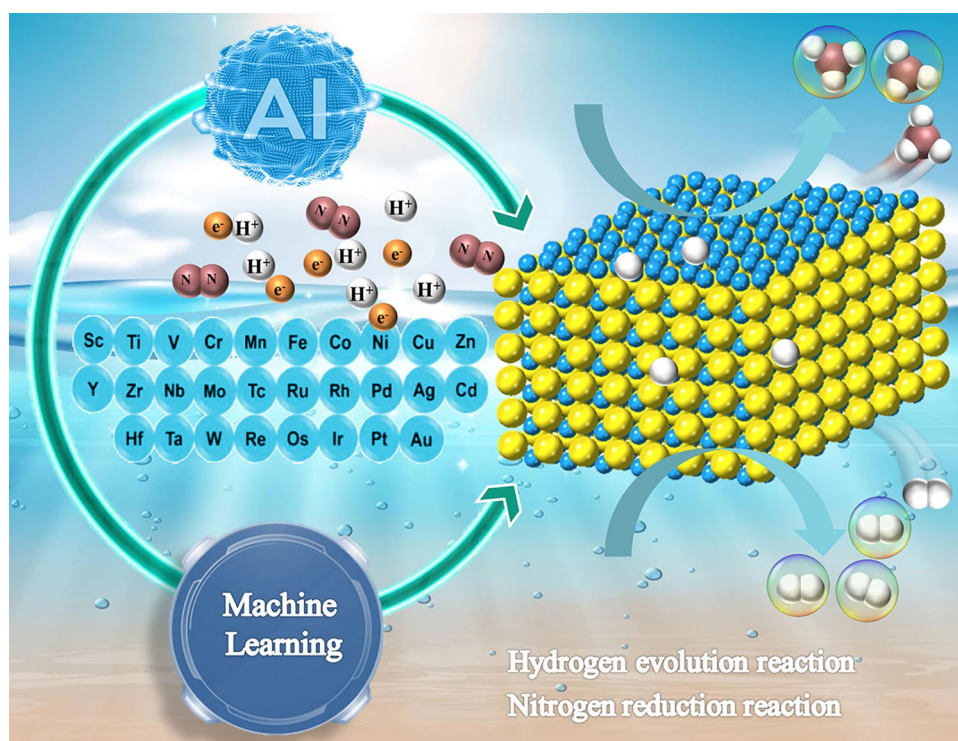


Fig. 11 Machine learning has become a powerful tool for the design and screening of novel catalysts for HER and NRR

composition, while maintaining the translation, rotation and arrangement symmetry of data sets. This method can accurately and rapidly predict the Gibbs free energy, the main indicator for characterizing catalyst activity. It can be well applied to various reactions, such as HER, CO₂ electroreduction, and oxygen evolution reactions (OER) [197–202]. Sun et al. [140] then used machine learning to screen efficient HER catalysts from MXenes and MBenes with or without single-atom doped. A database of 110 bare MBenes and 70 randomly selected single atom doped MBenes was first calculated by DFT calculations. They used four algorithms to predict ΔG_{H}^* , including the least absolute shrinkage and selection operator (LASSO), random forest (RFR), kernel ridge (KRR) and support vector (SVR) regression. Among them, SVR is the best model because it has efficient and stable prediction performance. Finally, by DFT calculations combined with the SVR model, the researchers found that the stable Co₂B₂ and Mn/Co₂B₂ are excellent HER catalysts due to $|\Delta G_{\text{H}}^*| < 0.15$ eV with a wide H coverage. Zafari et al. [203] also investigated MBenes, defect-engineered 2D materials and 2D π -conjugated polymer (2DCP)-supported single-atom catalysts to promote the reduction of N₂ to NH₃ while inhibiting the HER using a machine learning system. DFT calculations showed that N₂ molecules can be trapped on the vacancies of MBenes with a significant increase in adsorption strength and N≡N bond length. Among all

catalysts, MnB and MoB have the highest activity with a limiting potential of about 0.33 V, and TaB has the highest selectivity. In addition, the defective 2D materials formed by Te, Se and S vacancies expose the N₂ molecules to a specific environment adjacent to the three transition metals, significantly increasing the N≡N bond length (up to 1.38 Å) which greatly improves the catalytic activity and selectivity. With the assistance of ML, catalyst methods for screening HER and NRR show higher efficiency than traditional computational and experimental trial-and-error methods.

4.3 MBenes-based Electrocatalysts for Other Reactions

Although NRR has been widely concerned as a more economical and environmentally friendly method, there are still some problems in the process of electrocatalytic ammonia synthesis, such as low yield and poor catalytic selectivity, because the strongly inert nonpolar N–N bond is difficult to be destroyed at room temperature. NO is another nitrogen-containing gas molecule. It is a free radical and has an unpaired electron in the 2p* anti-bond orbital, so the N–O bond is easily activated [204]. Generally speaking, under the catalysis of NO, the process of ammonia synthesis follows two mechanisms, namely, association and dissociation. Recently, researchers have worked on the synthesis of ammonia by electrocatalytic nitrous oxide electroreduction

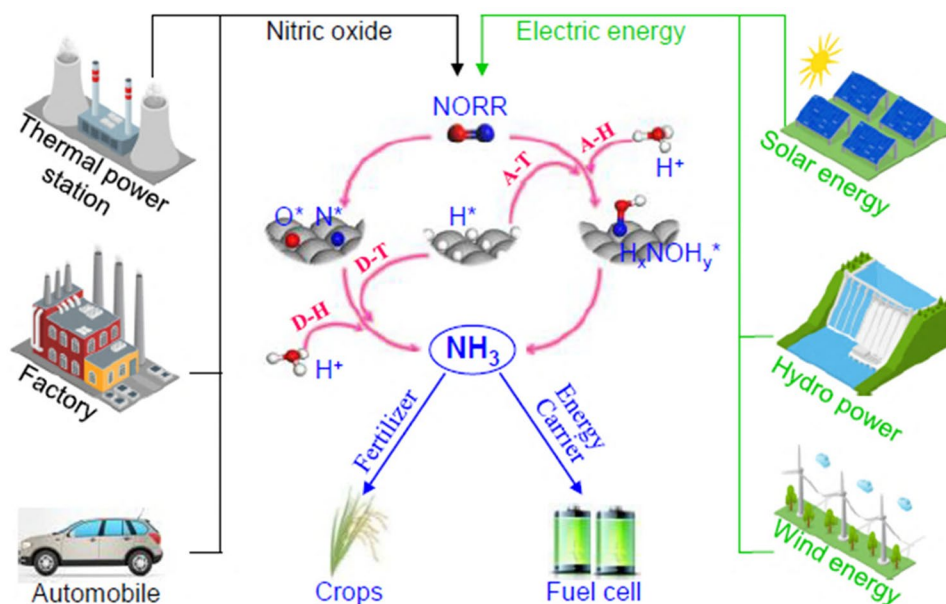


Fig. 12 Illustration of the proposed electrochemical ammonia synthesis route from NO from Ref. [205]

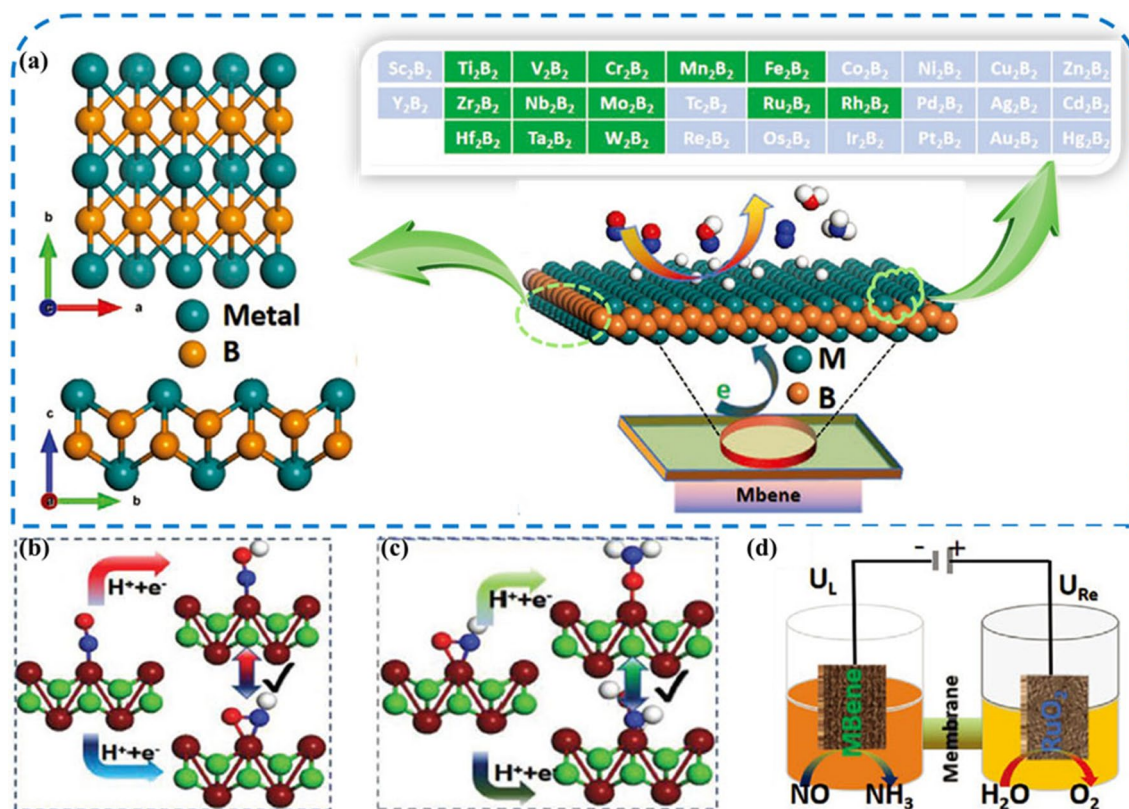


Fig. 13 **a** Top views of the M_2B_2 MBene monolayers. The metal and boron atoms are marked by cyan and orange spheres, respectively. Researchers screened M_2B_2 monolayers, including 3d, 4d, and 5d transition-metal boride compounds. Green and light blue represent stable and unstable M_2B_2 , respectively, which were verified from phonon spectrum calculations. **b**, **c** Schematic illustration of bifurcation reaction steps during the hydrogenation of NO to NH_3 on V_2B_2 MBenes. **d** A schematic diagram of the desired electrochemical cell for the NORR (cathode: MBene) and OER (anode: RuO_2 , for reference electrode). Reproduced with permission from Ref. [206]. (Color figure online)

reaction (NOER) using NO as a nitrogen source. For example, Long's team [205] proposed a new strategy to synthesize ammonia by electrocatalytic reduction of nitric oxide emitted from industrial waste gas and automobile exhaust, providing a new idea for denitrification and electrocatalytic synthesis of NH_3 (Fig. 12). Density functional theory calculations showed that electrochemical NOER is more active than N_2 reduction, and the most active copper (overpotential is 0.9 V vs. RHE) among the transition metal catalysts with moderate reactivity was screened. However, noble metals as a NOER catalyst have the disadvantages of high cost and low utilization rate, and there is a need to find a more efficient and practical catalyst.

Recently, Xiao et al. [206] investigated the catalytic performance of a series of MBenes (M_2B_2) for the NOER and found that Fe_2B_2 , Mn_2B_2 and Rh_2B_2 are highly active and selective, and are promising electrocatalysts for the conversion of NO to NH_3 (Fig. 13a). The investigators identified

the most favorable pathway and rate determining steps by assuming the route reaction network, taking into account the detailed binding properties of the intermediates and the limiting potentials of the corresponding reaction steps. Competing HER was also considered and compared on MBene catalysts, and most of these MBene candidates were found to be highly selective for NOER, with the exception of Ti_2B_2 , V_2B_2 , and Zr_2B_2 . In order to identify the most favorable NORR reaction pathway, the researchers determined the lowest Gibbs free energy diagram of NORR. The bifurcated reaction steps in the hydrogenation of NO to NH_3 in V_2B_2 MBenes are shown in Fig. 13b, c. The researchers also used Boltzmann distribution to calculate the selectivity of NORR. Depending on the Gibbs free energy difference between the two competing reaction steps, the potential difference between the redox potential (U_R) anode and the limiting potential (U_L) cathode can be used as a descriptor to estimate the oxidation trend on these 12 MBenes (Fig. 13d). The

larger the positive value of $U_R - U_L$, the stronger the ability to promote surface reduction. The calculated $U_R - U_L$ values are positive for all MBene monolayers, indicating that MBenes can inhibit surface oxidation. Volcano diagrams provide an efficient method for exploring promising candidate catalysts and reaction mechanisms. Calculations showed that Nb_2B_2 and Zr_2B_2 are located near the volcanic region and have intermediate binding energies of -3.20 and -4.31 eV, respectively. The limiting potentials for the formation of NH_3 , N_2 , and N_2O on Nb_2B_2 are 0.25 , 5.16 , and 2.53 V, respectively. He et al. [143] also studied the possibility of electrocatalytic NO synthesis of ammonia from 2D MBenes. They studied the orthorhombic group structure with CMCM (CrB, MnB, MoB, HfB and WB), which is composed of two layers of alternating transition metal atoms and boron atoms. The investigators calculated the overpotential for the electrocatalytic synthesis of ammonia from NO on the surfaces of five molecular sieves. The results showed that all MBenes catalysts except CrB (1.05 eV) require lower overpotential than copper in the NOER reaction, which implies that MBenes is a more suitable catalyst for the NOER. In the association pathway, NO can be completely spontaneously hydrogenated on the surface of MnB for ammonia synthesis. For the dissociation pathway, the overpotential on CrB, HfB and WB surfaces is less than 0.7 eV, which is viable in practical production. These findings provide new theoretical and experimental directions for the development of electrocatalytic ammonia synthesis.

Many transition metals have been applied for catalytic CO_2 reduction [208–212], for example, copper and copper-based alloys show high selectivity for the generation of hydrocarbons [213, 214]. However, the required overpotential is still too high for practical application. Considering that copper is already at the top of an active "volcano" in the reaction pathway with *CO and *CHO intermediates, catalysts with different reaction mechanisms should be used to reduce the overpotential required for the electroreduction of CO_2 to CH_4 [215, 216]. Based on this, Yuan et al. [217] screened 13 stable transition metal diboride (MB_2) monolayers, which all showed good selectivity for CH_4 production. Since the adsorption of *H is much weaker than that of *CO_2 , it well suppresses the HER reaction. Researchers found that OsB_2 is the most promising catalyst for the conversion of CO_2 to CH_4 , with a limiting potential of only -0.4 V. Liu et al. [207] computationally investigated 2D MBenes (Cr_2B_2 , Mn_2B_2 , Fe_2B_2 , Mo_2B_2) (Fig. 14a) as potential CO_2 reduction

reaction (CO_2RR) catalysts (Fig. 14b). Electrochemical reduction of CO_2 to produce other products (hydrocarbons and alcohols) is a promising strategy to mitigate the greenhouse effect and energy shortage. To achieve high CO_2RR efficiency, HER must be suppressed. The free energy of adsorbing H on Cu (111) surface is -0.15 eV, and the HER of Cr_2B_2 and Mo_2B_2 is relatively low with free energies of -0.34 and -0.76 eV. However, the free energy of Fe_2B_2 and Mn_2B_2 is close to zero, which leads to poor selectivity of CO_2RR (Fig. 14c). In their study, it was found that Mo_2B_2 not only achieves a balance between the limiting potential of CO_2RR and its performance, but also has a strong CO_2 capture capacity, making it an ideal CO_2RR catalyst. Xiao et al. [94] also investigated 11 new MBenes (Fig. 14d) as new high-efficiency catalysts for the CO_2RR within ab initio calculations. The researchers have fully considered the reaction mechanism and catalytic activity of CO_2RR on different types of MBene surfaces (Fig. 14e), as well as the selectivity related to the competitive reaction with HER. These novel 2D composites with large specific surface area and good electrical conductivity have unique electrocatalytic advantages. 2D Au_2B and V_3B_4 MBenes are more suitable as a platform for the electrocatalytic reduction of CO_2 to CH_4 . The evolution of the rate determination step is determined by ΔG_{*OH} . When ΔG_{*OH} reaches -3.47 eV, the rate determination step changes from $^*HCHO + H^+ + e^- \rightarrow ^*O + CH_4$ to $^*CH_3O + H^+ + e^- \rightarrow ^*O + CH_4$, and the catalytic activity for CO_2RR reaches the best (Fig. 14f). The limit potentials of Au_2B and Mo_2B are -0.11 and 0.60 eV, which is favorable for CO_2RR . Furthermore, Au_2B , Os_2B_4 and Ru_2B_4 are more suitable than other MBenes for the production of methanol with overpotentials of 0.31 , 0.48 , and 0.35 V. These findings provide theoretical guidance for the diffusion and application of 2D MBene systems in CO_2 electroreduction catalysts.

4.4 SAC-Type Doping of MBenes for HER/OER and NRR

Researchers have been working on the design of efficient two-dimensional catalysts for practical applications in production. Among various catalyst designs, single-atom catalysts have attracted much attention owing to their unique electronic structures. SACs fully expose and disperse the active center, which allows SACs to exhibit remarkable catalytic performance in various reactions. Recently, some

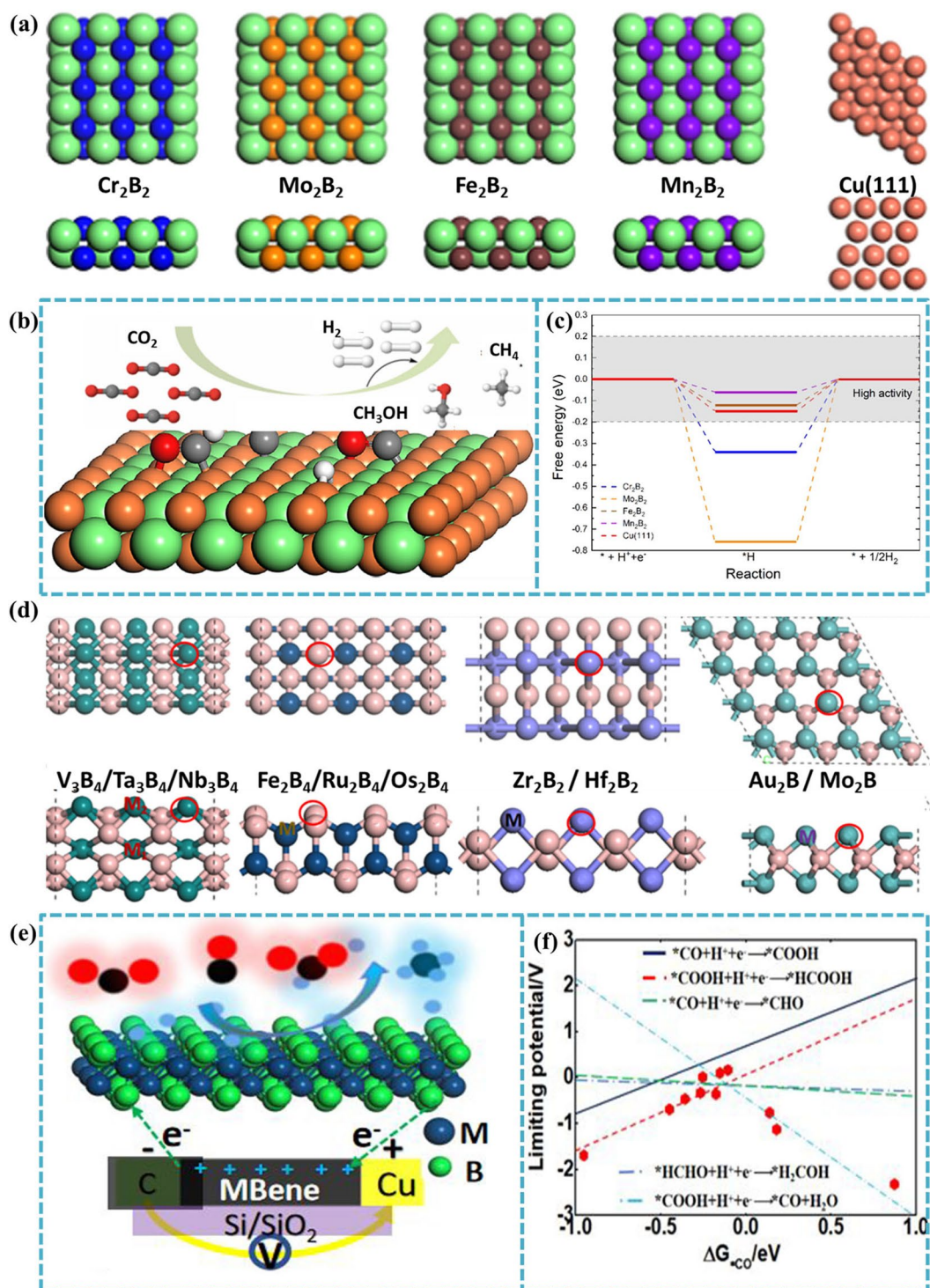


Fig. 14 **a** Optimized structures of Cr_2B_2 , Mo_2B_2 , Fe_2B_2 , Mn_2B_2 , and the $\text{Cu}(111)$ surface. **b** Schematic diagram of the reaction for the electroreduction of CO_2RR on 2D M_2B_2 MBenes. **c** Relative free energy diagrams of HER on MBenes and $\text{Cu}(111)$. Reproduced with permission from Ref. [207]. **d** Top views (upper) and side views (lower) of different types of MBene structures, the red circles represent the active sites for CO_2 adsorption and intermediate production. **e** Schematic diagram of the reaction for the electroreduction of CO_2RR on 2D MBenes. **f** Limiting potentials for each elementary reaction step as a function depending on the formation energy of ΔG_{CO} . Reproduced with permission from Ref. [94]

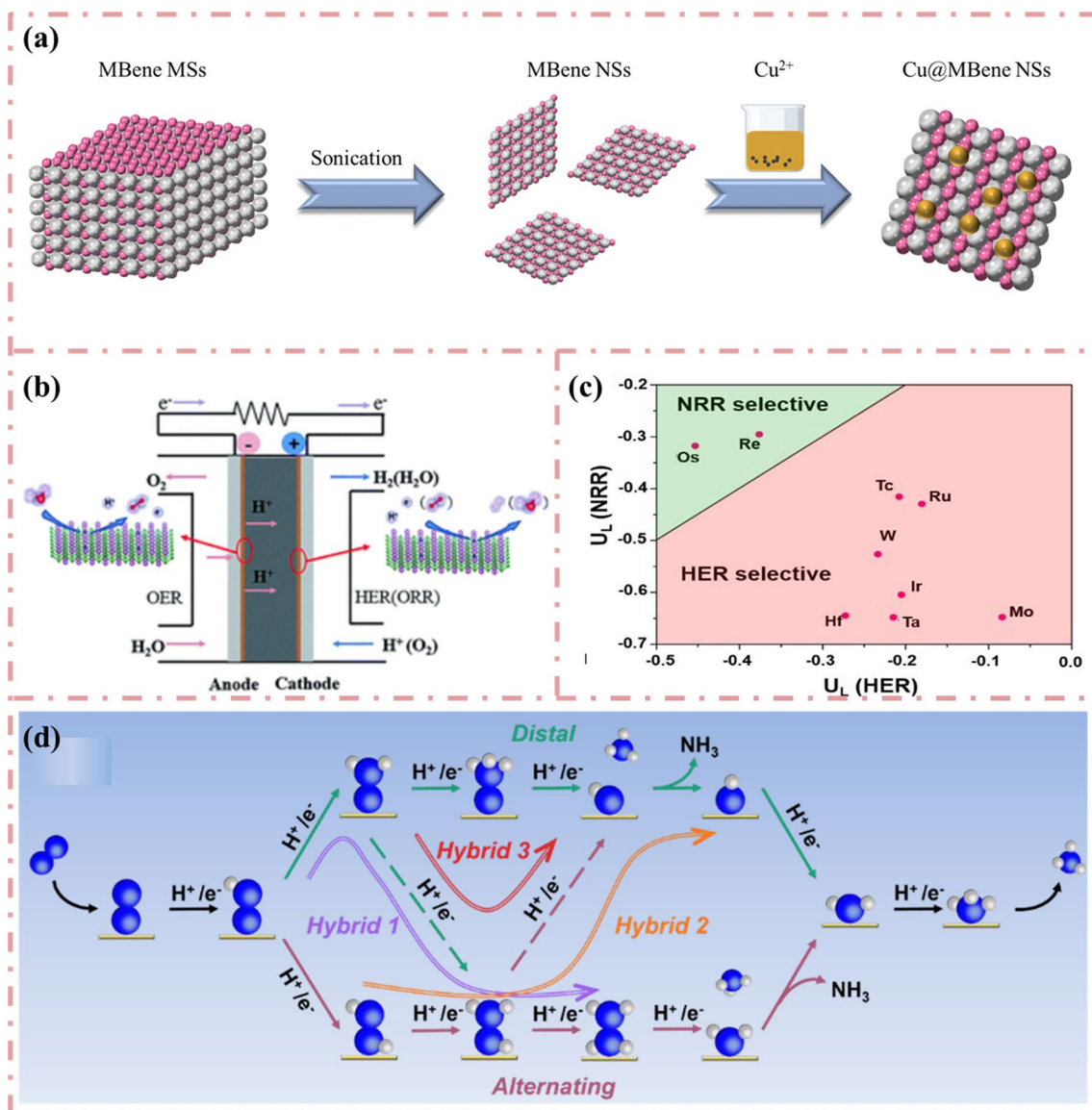


Fig. 15 **a** A schematic formation mechanism of the Cu@MBene NSs. **b** Schematic illustration of the process of water splitting. Reproduced with permission from Ref. [218]. **c** The calculated potential vs SHE for HER ($U_{\text{L}}(\text{HER})$) and NRR ($U_{\text{L}}(\text{NRR})$) for selectivity screening. **d** Schematic of the possible five routes (the distal, alternating, hybrid 1, hybrid 2 and hybrid 3) for eNRR over $\text{Mo}_2\text{B}_2\text{O}_2\text{-SA}$ systems. Reproduced with permission from Ref. [219]

researchers have focused on embedding transition metal atoms in MBenes to improve the catalytic performance. The schematic formation mechanism of the Cu@MBene NSs is shown in Fig. 15a. Zhang et al. [218] investigated catalytic activity of Mo_2B_2 MBene-supported SACs by embedding a series of transition metal atoms in Mo vacancy ($\text{TM@Mo}_2\text{B}_2$, $\text{TM}=\text{Ti, V, Cr, Mn, Fe, Co, Ni}$ and Cu) as bifunctional electrocatalysts for oxygen evolution reaction, oxygen reduction reaction and HER (Fig. 15b).

The structural stability was first investigated, and the calculations showed that the binding energies of $\text{TM@Mo}_2\text{B}_2$ were all negative and the studied materials all had good structural stability. Then the researchers found that $\text{Ni@Mo}_2\text{B}_2$ is a promising HER/OER bifunctional electrocatalyst with low $|\Delta G_{\text{H}}|$ (-0.09 eV) at $1/4\text{H}$ coverage and OER overpotential (0.52 V). In addition, $\text{Cu@Mo}_2\text{B}_2$ has the potential to be an OER/ORR bifunctional electrocatalyst with low OER (0.31 V) and ORR (0.34 V) overpotentials.

In addition to the applications in HER, there are also applications in NRR where transition metal atoms are embedded to improve the performance of MBenes catalysts. Yao et al. [219] investigated a series of transition metal atoms embedded in Mo vacancies from group IVB to VIII in $\text{Mo}_2\text{B}_2\text{O}_2$ for NRR and performed a systematic screening of their activities and selectivity in potential-determining steps (PDSs) and their competitive selectivity with HER. The introduction of SACs inhibited HER, which was manifested by the shortening of the distance from the dashed line. Among them, $\text{Mo}_2\text{B}_2\text{O}_2$ with embedded Re and Os has the best suppression effect on HER, breaking the boundary between HER and NRR equilibrium and making the NRR process more favorable (Fig. 15c). The results showed that Re and Os- $\text{Mo}_2\text{B}_2\text{O}_2$ have significant catalytic activity with low determining PDS of 0.29 and 0.32 eV, respectively. Considering the end-on adsorption mode of N_2 in the $\text{Mo}_2\text{B}_2\text{O}_2$ -SA system, the electrocatalytic NRR process is based on two basic mechanisms involving different intermediates (Fig. 15d). In order to predict the optimal eNRR

performance, they also studied all the intermediate steps related to remote and alternate paths for selected Re and Os systems. Therefore, better catalytic performance of eNRR can be predicted, giving directions for future experimental directions of eNRR.

Currently, there is a paucity of studies on the application of h-MBenes (MBenes are derived from the precursor hexagonal MAB phase), which provides a wide scope for exploration. Li et al. [141] systematically explored SA- $\text{Mo}_2\text{B}_2\text{O}_2$ and SA- $\text{W}_2\text{B}_2\text{O}_2$ as efficient catalysts for HER through first principles calculations. Since the F-functional group is converted to O-functional group on the surface of MBene under certain conditions during the actual preparation process. Therefore, they constructed a specific adsorption geometry configuration of MBene structure with O atom as the outermost surface functional group. After the introduction of the single atom, the researchers' calculations showed that SA- $\text{Mo}_2\text{B}_2\text{O}_2$ and SA- $\text{W}_2\text{B}_2\text{O}_2$ (SA = Ti, V and Zn) exhibit better stability properties based on negative binding energies. The investigators found that embedding a single transition

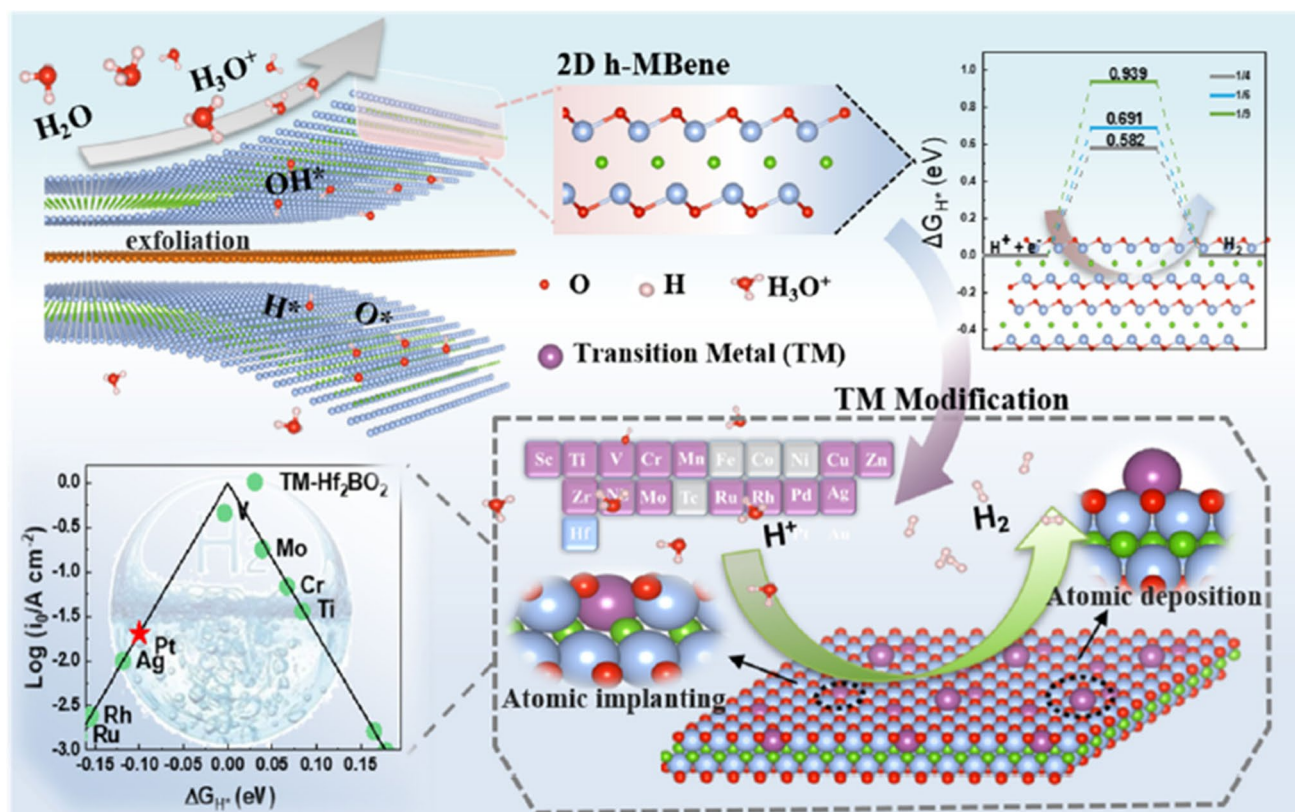


Fig. 16 Schematic illustration of the process of preparing h-MBenes by exfoliating A layer and transition metal (TM) modification approaches by atomic deposition and atomic implanting. Reproduced with permission from Ref. [220]

metal atom on MBenes, the H–O bond distance increases, indicating that the H–O bond is weakened by the embedded atom. This is more favorable for the H₂ adsorption and desorption processes, which significantly accelerates the HER process. Recently, Feng et al. [220] chose 2D Hf₂B as the object of study for its application in electrocatalytic HER. In this study, two TM modifications were proposed to significantly improve the catalytic activity of Hf₂BO₂: atom deposition of TM@Hf₂BO₂ and atom implanting of TM-Hf₂BO₂. The results of ΔG_{H^*} showed that the system can hardly satisfy both stability and catalytic activity after deposition of TM atoms (Fig. 16). Notably, only atomic implanting can significantly activate the TM-Hf₂BO₂ surface. They also investigated the factors affecting the catalytic activity and performed detailed electronic structure calculations for TM-doped Hf₂BO₂. Since the antibonding position of H–O rises slightly after Mo atom doping, the increase in the bonding energy of H–O leads to a decrease of ΔG_{H^*} from 0.9 to 0.04 eV. The above work shows that h-MBenes can open a new field for 2D materials due to their good electrocatalytic properties and will stimulate researchers to explore the synthesis of h-MAB phase and the exfoliation of h-MBenes.

5 Potential Impact of MBenes in Energy Storage

2D materials are anode materials for rechargeable batteries due to their high specific surface area, excellent electron mobility and superior mechanical properties. In recent years, numerous 2D materials have been investigated as anode materials with great success, such as graphene [221], MoS₂ [222], Mo₂C [223], Ti₃C₂ [224]. Likewise, MBene has great potential as a 2D layered material for energy storage. Theoretical calculations are playing an increasingly critical function in revealing the mechanism of action of MBene in the battery.

In the last three years, a large number of MBenes as anode materials for rechargeable battery have been predicted by theoretical work. Researchers usually evaluate the performance of MBene as a metal ion battery electrode material by calculating the structure, electronic properties, adsorption and diffusion properties of metal atoms on the MBene surface, open circuit voltage and specific capacity (Fig. 17).

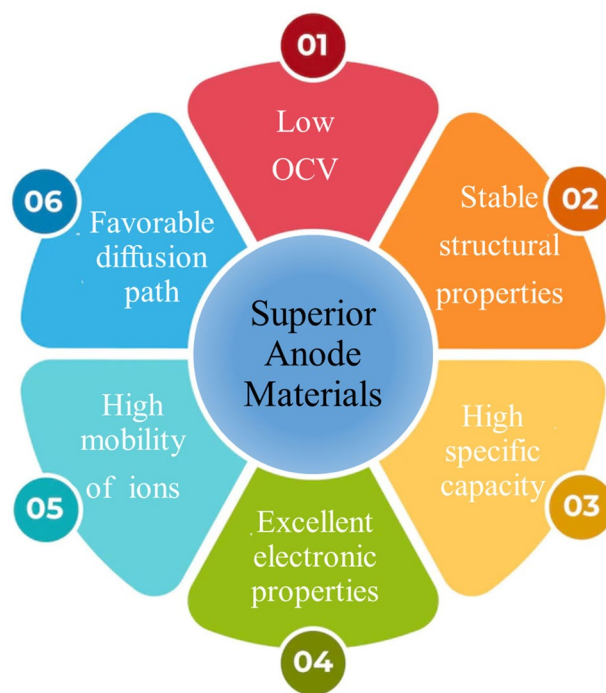


Fig. 17 Properties of a high-performing battery anode materials

5.1 Problems Solved in Metal-Ion Batteries

The reversible energy storage of rechargeable batteries depends mainly on the insertion/extraction of metal ions (Li⁺, Na⁺, K⁺, Mg²⁺). MBenes have a layered structure, high specific surface area and abundant active centers, which facilitates the insertion and storage of metal ions. Although MBene as an electrode material has a similar working mechanism for different metal ions, the battery performance varies greatly due to the inherent properties of the metal ions (e.g., ionic radius and valence electrons). More specifically, the ionic radius and valence electrons of metal ions affect the interaction between metal ions and MBene, thus affecting its adsorption, storage and diffusion properties. The great success of MBenes as anode materials for LIBs and SIBs has been proved theoretically. As a negative electrode, MBenes have greater application potential, for example, the most remarkable theoretical capacity is higher than other 2D materials. In addition, the negative adsorption energy of lithium–sodium atoms on the surface of various MBenes is large, which indicates that the interaction between MBenes and lithium–sodium atoms is strong. The diffusion barrier of

Table 5 Summary of main performances of MBenes as anode materials for rechargeable batteries

Materials	Type	Specific capacity (mAh g ⁻¹)	Diffusion energy (meV)	OCV (V)	Refs.
Graphite	LIBs	372	400	–	[225]
Ti ₃ C ₂	LIBs	320	280	0.62	[226]
Mo ₂ B ₂	LIBs	444	270	0.41	[86]
	MIBs	502.1	840	0.84	[227]
Tetr- Mo ₂ B ₂	LIBs	251	29	0.835	[228]
	SIBs	251	10	0.515	[228]
Tri- Mo ₂ B ₂	LIBs	251	23	0.407	[228]
	SIBs	188	13	0.383	[228]
Fe ₂ B ₂	LIBs	665	240	0.33	[86]
T-Mo ₂ B	LIBs	264	37	0.628	[229]
H-Mo ₂ B	LIBs	74.18	50	0.386	[229]
Zr ₂ B ₂	LIBs	526	17	0.236	[230]
TiB	LIBs	480	20	0.33	[90]
	SIBs	480	20	0.17	[90]
TiB ₃	LIBs	1335.04	38	0.156	[231]
	SIBs	667.52	157	0.195	[231]
Ti ₂ B ₂	LIBs	456	17	0.526	[232]
	SIBs	342	8	0.502	[232]
V ₂ B ₂	LIBs	969	220	–	[92]
	SIBs	614	130	–	[92]
V ₂ B ₂ O ₂	LIBs	812	390	0.57	[92]
	SIBs	547	420	0.41	[92]
Cr ₂ B ₂	LIBs	696	280	–	[92]
	SIBs	492	170	–	[92]
	MIBs	853.4	380	0.53	[227]
Mn ₂ B ₂	LIBs	679	290	–	[92]
	SIBs	483	170	–	[92]
Sc ₂ B	MIBs	3192.81	40	0.023	[233]
	LIBs	532.14	60	0.182	[233]
	SIBs	532.14	20	0.327	[233]
Ti ₂ B	MIBs	3018.41	80	0.101	[233]
	LIBs	503.07	90	0.532	[233]
	SIBs	503.07	110	0.432	[233]
V ₂ B	MIBs	2853.95	40	0.142	[233]
	LIBs	475.66	150	0.748	[233]
	SIBs	503.07	10	0.558	[233]
Y ₂ B ₂	LIBs	806.31	13	0.33	[234]
	SIBs	403.16	8	0.30	[234]
ScB	LIBs	427.373	108	0.409	[235]
	SIBs	340.287	72	0.446	[235]
TiB	LIBs	408.421	105	0.683	[235]
	SIBs	328.162	63	0.528	[235]
VB	LIBs	390.168	264	0.797	[235]
	SIBs	316.273	85	0.553	[235]
V ₂ B ₂	SIBs	814	11	0.65	[84]

lithium sodium atom is also lower than that of other materials, which can greatly improve the charge and discharge rate. At the same time, the open circuit voltage of Li/Na ions on the monolayer is in the range of 0–1 V, which may effectively inhibit the formation of Li/Na dendrites on the anode during charge and discharge. Based on MBenes as the negative electrode of ion battery, the performance of ion battery is greatly improved.

In this section, we summarize the main contributions of MBenes as anode materials for ion batteries. Table 5 summarizes the performance of MBenes in rechargeable batteries. It can be clearly seen the theoretical specific capacity is superior to that of some other 2D materials such as graphite and Ti₃C₂. Due to the structural difference between MBenes and MXenes, MBenes exhibit more excellent potential in LIBs, SIBs and MIBs.

Since the commercialization of rechargeable lithium-ion batteries, they have been favored by researchers because of their advantages of large capacity, high power density, long cycle life and high energy efficiency. The performance of lithium-ion battery depends on the performance of electrode materials to a great extent. The structure and working mechanisms for LIBs have been demonstrated in Fig. 18a and b. At present, graphite has been commercially used as anode material for lithium-ion batteries because of its high coulomb efficiency, relatively good cycle stability and low cost. However, its relatively low theoretical specific capacity (372 mAh g⁻¹) and poor rate capability are still far from the demand of modern electronic market. Therefore, it is urgent to find new anode materials to further improve the performance of LIBs.

2D MBenes have similar structure to MXenes, and many studies have proved that MBenes plays a great role in improving the performance of ion batteries. Considering that the molar mass of boron is less than that of carbon and nitrogen, it is possible to achieve higher theoretical specific capacity by using MBenes as electrode material. For example, Guo et al. [86] reported for the first time the performance of two-dimensional Mo₂B₂ and Fe₂B₂ as anode materials for lithium ion batteries. They calculated the adsorption energy of isolated lithium atoms, and the negative value of adsorption energy of lithium atoms is relatively large, which indicates that there is a strong interaction between Li atoms and MBene, which is beneficial to prevent the formation of metal Li and improve the safety and reversibility of LIBs. The theoretical specific

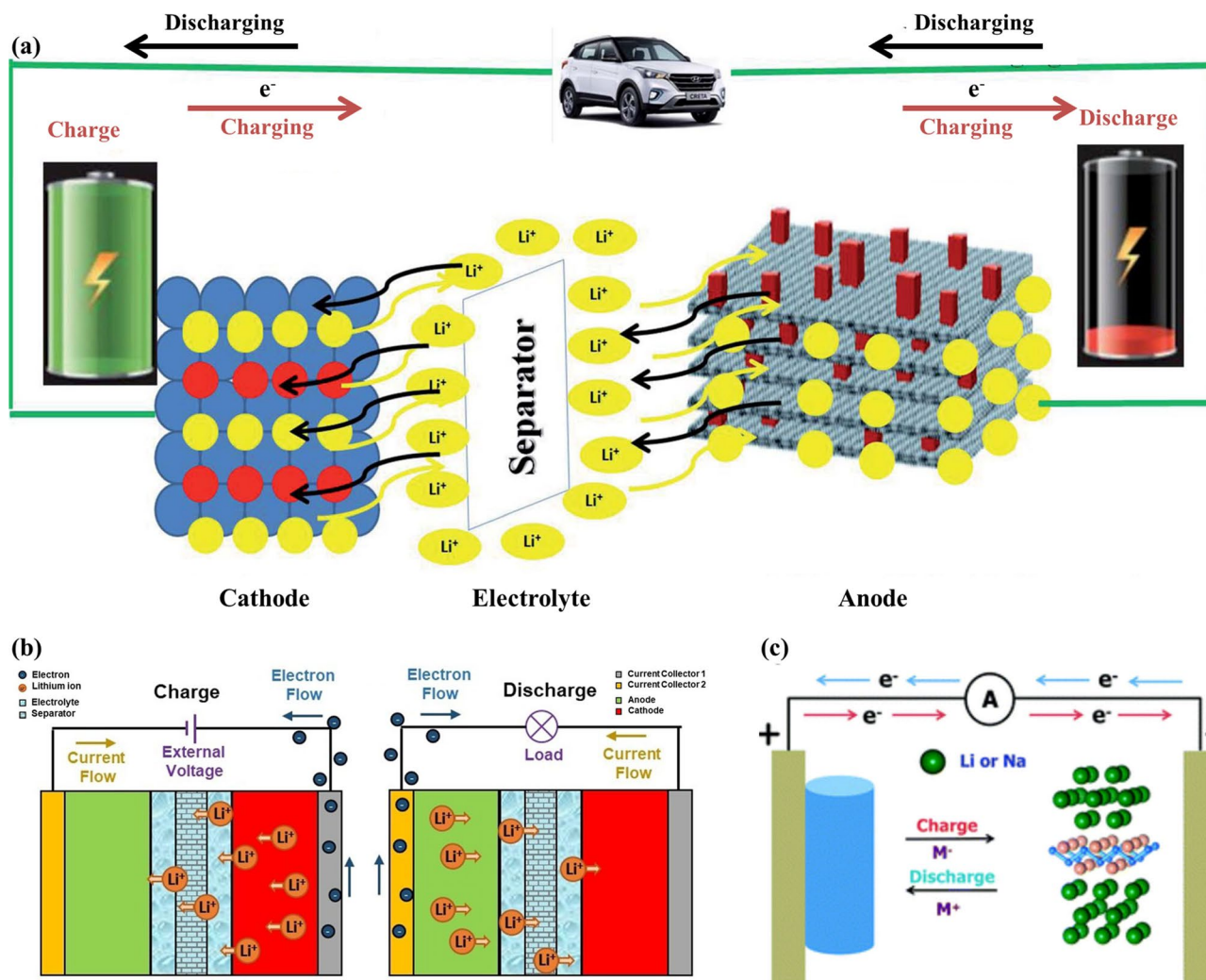


Fig. 18 **a** Schematic illustration of MXene-based anode batteries. Reproduced with permission from Ref. [47]. **b** Schematic structure of the metal-ion batteries showing the working mechanisms of the charge and discharge process. Reproduced with permission from Ref. [236]. **c** Schematic illustration of MBene-based anode batteries. Reproduced with permission from Ref. [92]

capacities of 2D Mo_2B_2 and Fe_2B_2 as LIB electrodes are ~ 444 and 665 mAh g^{-1} , respectively, which are better than some other 2D materials. In addition, the energy barriers of the two diffusion paths are similar, which will increase the charge and discharge rate of LIBs. Generally speaking, MBenes should be a good candidate anode material in LIBs due to the small diffusion energy barrier of Mo_2B_2 and Fe_2B_2 MBenes, high storage capacity for Li atoms and strong applicability.

In addition, Bo and co-workers [232] firstly investigated a set of hexagonal MBenes including Sc_2B_2 , Ti_2B_2 , V_2B_2 , Cr_2B_2 , Y_2B_2 , Zr_2B_2 , and Mo_2B_2 . They chose Ti_2B_2 monolayer as anode material for LIBs and SIBs based on DFT

calculations. Similarly, the working mechanisms of MBene for LIBs and SIBs have been demonstrated in Fig. 18c. Through electronic structure calculation, researchers found that the whole lithium ionization process has good electronic conductivity. The volume change of Ti_2B_2 monolayer is very small after adsorbing the first, second and third layers of Li and Na ions, which indicates that Ti_2B_2 monolayer is robust. Moreover, Ti_2B_2 possessed high theoretical specific capacities of 456 and 342 mAh g^{-1} and ultralow energy barrier of $0.017/0.008 \text{ eV}$ for Li and Na, respectively. The results show that Ti_2B_2 monolayer and other hexagonal 2D MBenes with high specific capacity and rapid diffusion are expected to be used as anode materials for LIBs and SIBs.

However, the Li diffusion barrier of Mo_2B_2 is very high, while the theoretical specific capacity of Ti_2B_2 relative to Li ion is insufficient. Therefore, it is necessary to find an anode material with ultra-low diffusion barrier and large theoretical specific capacity. Zha et al. [229] predicted H- and T-type Mo_2B as anode materials for LIB based on first-principles calculations. Compared with Mo_2C [237], the electrical conductivity of both H- and T-type Mo_2B is comparable, while the thermal conductivity is much higher. T-type Mo_2B exhibits good performance in LIBs. The theoretical volume capacity is up to 2424 mAh cm^{-3} and the migration barrier is as low as 0.0372 eV . H-type Mo_2B is a stable structure that can be transformed into a T-type by applying strains.

With the ubiquitous use of lithium-ion batteries and the continuous depletion of lithium resources, there is an urgent need to develop some new resource-rich batteries. Researchers have systematically investigated the intercalation behavior of sodium, potassium, and magnesium ions using a first-principles simulation approach to provide insight into the storage mechanism of metal ions on MBenes. Due to the abundant resources and environmentally friendly nature of non-lithium alkali metals, rechargeable sodium, potassium, and magnesium ion batteries have received significant attention as emerging technologies for low-cost renewable energy storage.

Na and K ion batteries are of interest because of their abundant natural reserves and low cost [238, 239]. In addition, the operating mechanism of Na and K ion batteries is similar to that of LIBs, with metal ions shuttling back and forth between the cathode and anode during the discharge and charging cycles. In addition, most 2D materials have low affinity for Na and K ions and their adsorption energies are usually less than 1.5 eV , which leads to lower open-circuit voltages [240]. Therefore, the development of an effective method to modulate the affinity of 2D electrodes for Na and K ions to increase the open-circuit voltage when used as a cathode and decrease the open-circuit voltage when used as an anode is an urgent need to increase the energy density. Liu et al. [241] investigated the effects of surface modification of oxygen group elements on the structure, stability and electrochemical properties of MoBX ($X = \text{O}, \text{S}, \text{Se}, \text{Te}$) as an anode material for SIBs and PIBs (Fig. 19a). The four feasible configurations for MoBX are shown in Fig. 19b. The MoB electrodes showed extremely high affinity for X atoms, and the calculated binding energy between X atoms decreases

in the order of $\text{MoBO} > \text{MoBS} > \text{MoBSe} > \text{MoBTe}$. MoBO is suitable for use as 2D cathode material with high OCVs of $3.2 \sim 2.2 \text{ V}$ for Na ions (K ions from 3.47 to 1.85 V). As a cathode material, the capacities in $\text{Na}_{0.5}\text{MoBO}$ and $\text{K}_{0.5}\text{MoBO}$ are ~ 110 and 110 mAh g^{-1} , respectively. Metal ions show good mobility on MoBX with an electronic potential barrier of $0.38\text{--}0.59 \text{ eV}$.

Wang et al. [90] investigated the adsorption of Li and Na atoms on the surface of TiB monolayers by DFT calculations and confirmed the potential of layered TiB as anode materials for LIBs and SIBs. Calculations showed that the theoretical specific capacity of TiB for Li or Na ions is 480 mAh g^{-1} , which is significantly higher than that of Ti_3C_2 [226]. The researchers also calculated the diffusion energy barriers of Li and Na between the most stable nearest-neighbor adsorption sites on the 3×3 TiB supercell along three different paths (Fig. 19c), showing that Li ions/sodium ions moving along paths 1 and 2 have lower energy barriers of $0.11/0.08$ and $0.16/0.11 \text{ eV}$, respectively (Fig. 19d). However, path 3 has the highest energy barrier of $0.22/0.17 \text{ eV}$. Due to its high specific capacity, low OCV and energy barrier for Li^+ and Na^+ ions, 2D TiB is expected to be an alternative material to commercial graphite anode for LIBs and SIBs.

Gao and his group [92] reported six new M_2B_2 MBenes ($M = \text{Ti}, \text{V}, \text{Cr}, \text{Mn}, \text{Zr}, \text{Nb}$) and predicted to obtain by exfoliation of layered MAB phases (Fig. 20a). The adsorption energy of Na is much smaller than that of Li for the same adsorption positions, indicating that the adsorption of Na on MBene monolayer is more stable than that of Li on MBene. There are three possible diffusion paths between the stable adsorption sites of Li/Na ions adjacent to monolayer MBenes (Fig. 20b). MBenes have low diffusion energy barriers ($0.22/0.13$, $0.28/0.17$, and $0.29/0.17 \text{ eV}$ for V_2B_2 (Fig. 20c, d), Cr_2B_2 and Mn_2B_2 , respectively) and high Li/Na atomic storage capacities ($969/614$, $696/492$, and $679/483 \text{ mAh g}^{-1}$). In addition, the Li/Na adsorption properties of the functionalized $\text{V}_2\text{B}_2\text{O}_2$ were also investigated by the researchers (Fig. 20e). Compared with V_2B_2 , the specific capacities (812.2 and 547 mAh g^{-1}) and OCVs (0.57 and 0.41 eV) of $\text{V}_2\text{B}_2\text{O}_2$ increased and decreased, respectively, which is not favorable for the application of functionalized V_2B_2 as LIB/SIB anode material. Bo et al. [228] predicted two new 2D tetragonal and triangular Mo_2B_2 structures (tetra- and tri- Mo_2B_2), both of which are lower in energy than the



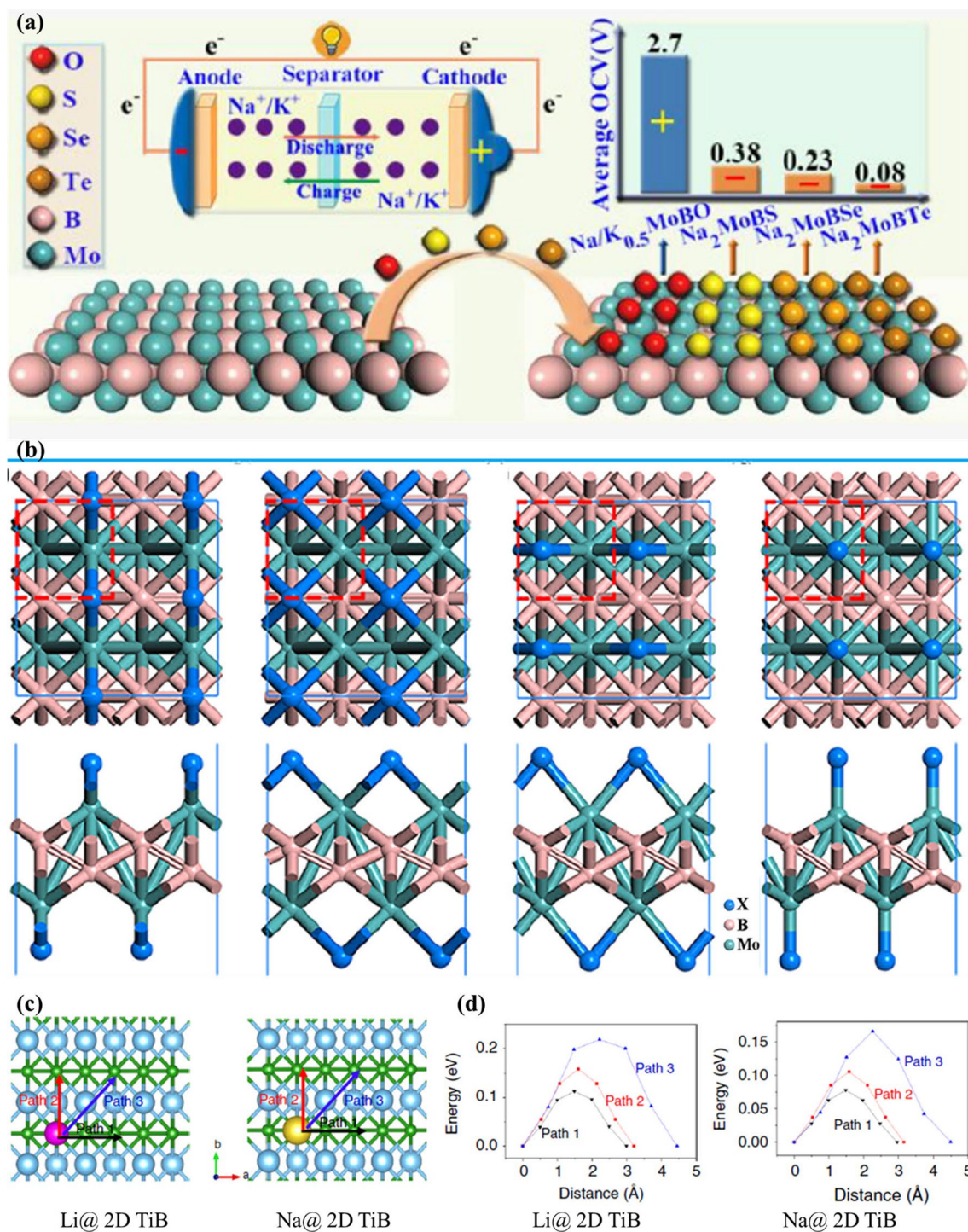


Fig. 19 **a** Schematic of a hybrid Na^+/K^+ battery using MoBX ($X = \text{O}, \text{S}, \text{Se}$ and Te) compounds as the electrode materials. Left: Average OCVs of $\text{Na}_{0.5}\text{MoBO}$ and $\text{K}_{0.5}\text{MoBO}$ for cathode application and of Na_2MoBS , Na_2MoBSe , and Na_2MoBTe for anode application. Calculated evolution of OCV values with different metal ion concentrations in Na_xMoBO (middle) and K_xMoBO (right). **b** Top and side views of adsorption sites for MoBX ($X = \text{O}, \text{S}, \text{Se}$, and Te). The unit cell is emphasized by a red dashed rectangle. The blue, pink, and ocean-blue balls represent X, B, and Mo atoms, respectively. Reproduced with permission from Ref. [241]. **c** Considered diffusion paths for Li and Na on the TiB monolayer. **d** Calculated diffusion energy barriers along the paths in c. The purple and yellow spheres represent Li and Na atoms, respectively. Reproduced with permission from Ref. [90]. (Color figure online)

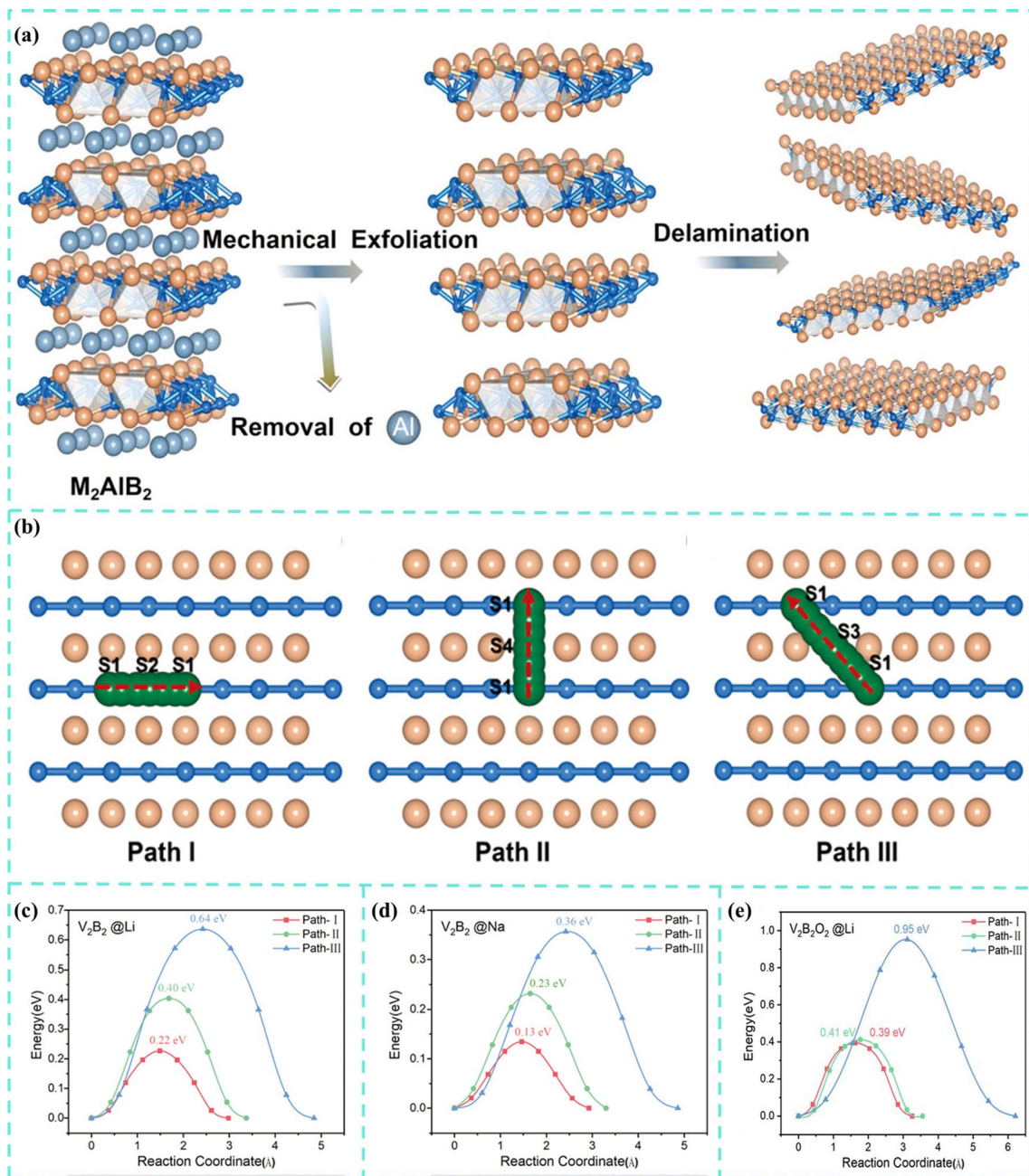


Fig. 20 **a** Schematic diagram of removing Al to form MBenes by mechanical exfoliation in the MAB phase. **b** Schematic diagram of the metal cation diffusion migration paths considered on monolayer MBenes: left: S1 → S2 → S1, middle: S1 → S4 → S1 and right: S1 → S3 → S1. **c** Diffusion energy curves of Li ions on V_2B_2 . **d** Diffusion energy curves of Na atoms on V_2B_2 . **e** Diffusion energy curves of Li ions on $V_2B_2O_2$. Reproduced with permission from Ref. [92]

orthorhombic and hexagonal structures. Interestingly, both tetra- and tri- Mo_2B_2 exhibit high Li/Na diffusion rates. The diffusion energy barriers of Li/Na on tetra- (0.029/0.010 eV) and tri- Mo_2B_2 (0.023/0.013 eV) are small, indicating that both monolayers have good charge/discharge performance for Li/Na.

Through DFT and ab initio molecular dynamics (AIMD) calculations, Yuan et al. [230] explored the potential of Zr_2B_2 MBene as anode materials for LIBs (Fig. 21a). The researchers calculated the diffusion barrier of Li ions on single layer Zr_2B_2 (Fig. 21b). According to its electronic structure, it was found that it contains metals during the whole

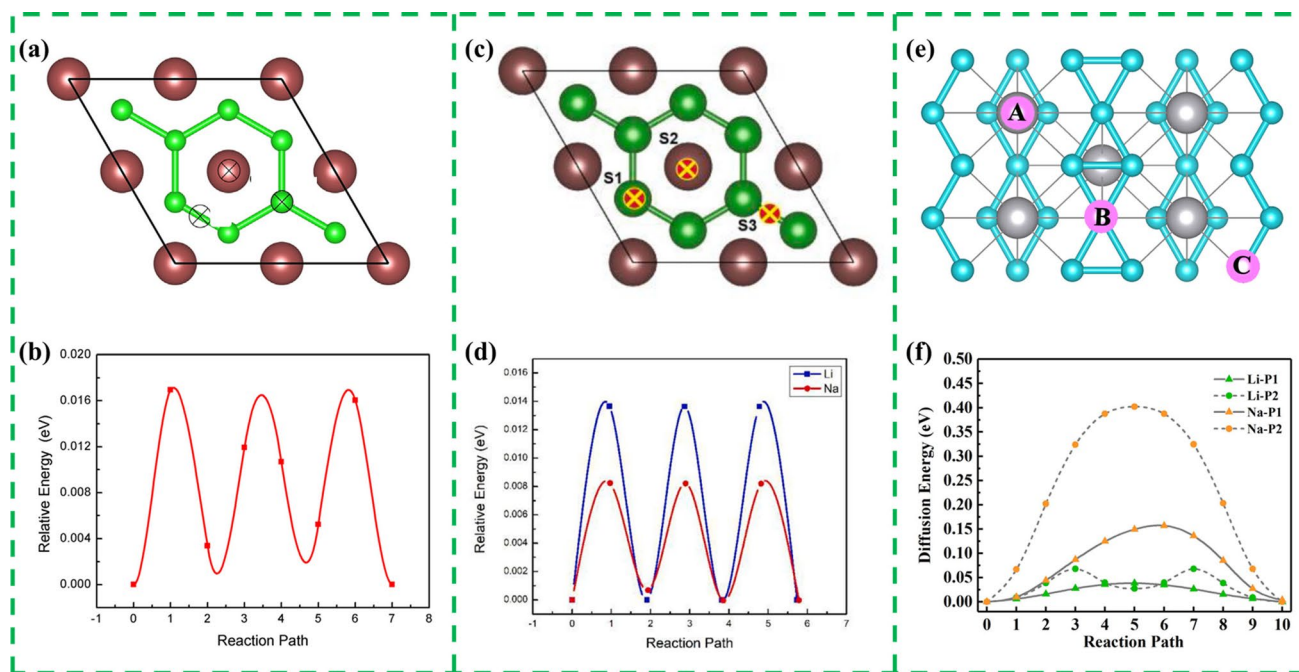


Fig. 21 **a** Top view of the stable structure of the monolayer Zr_2B_2 . The brown and green balls represent the Zr and B atoms, respectively. **b** The energy during the diffusion process on the monolayer Zr_2B_2 . Reproduced with permission from Ref. [230]. **c** Top view of 2D Y_2B_2 crystal structures. The Y and B atoms are denoted by brown and green spheres. **d** The diffusion energy barrier curves of M on Y_2B_2 . Reproduced with permission from Ref. [234]. **e** The adsorption site of Li/Na on TiB_3 monolayer. **f** Diffusion barrier of Li and Na on TiB_3 monolayer along P1 and P2, respectively. Reproduced with permission from Ref. [231]

lithium process, which demonstrated Zr_2B_2 is a promising anode material for LIBs. Gao and co-workers [234] demonstrated that 2D Y_2B_2 is kinetically and thermally stable and that electrons conduct well during charging, calculating the potential application of 2D Y_2B_2 in rechargeable LIBs and SIBs (Fig. 21c). Calculations showed that the low diffusion energy barriers of Li and Na on Y_2B_2 are 0.013 and 0.008 eV, respectively (Fig. 21d). The theoretical specific capacitance of Li/Na on Y_2B_2 is 806.31 and 403.16 mAh g^{-1} , and the OCV of Li/Na varies from 0.43 to 0.24/0.45 to 0.15 V at different Li/Na concentrations. These excellent physical properties indicated that 2D Y_2B_2 has good application prospects in battery. Li et al. [231] identified a novel TiB_3 MBene with unique boron chains on the surface by crystal structure prediction by changing the wrapping ratio of the nonmetallic element boron to metal atoms to weaken the near-neighbor electrostatic repulsion (Fig. 21e). They used a simple analysis based on electrostatic potential to quickly screen the adsorption sites of Li/Na atoms. Similarly, the diffusion energy barrier between the two most favorable adsorption centers on TiB_3 monolayer was calculated.

For P1 (A \rightarrow A), Li/Na ions move directly from A site to another nearest A site, and the energy barrier is small (Li ion is 0.038 eV, Na ion is 0.157 eV). The diffusion along P2 (A \rightarrow B \rightarrow A) has a large potential barrier (0.068 eV for Li ion and 0.402 eV for Na ion), and the constructed A \rightarrow C \rightarrow A path will automatically change into A \rightarrow B \rightarrow A after optimization (Fig. 21f). It is worth pointing out that TiB_3 has a high capacity of 1335.04 and 667.52 mAh g^{-1} in LIBs/SIBs, respectively, which is the highest record for other MBene and many MXene.

Li et al. [235] calculated the performance of ScB, TiB, and ScB as LIBs and SIBs anodes by first principles. The two monolayers are thermodynamically stable at room temperature and show obvious metal characteristics, which provides unique advantages for monolayers as anode materials. They studied the diffusion kinetics of Li/Na atoms at the most favorable adsorption sites, and found that the adsorption strength of Na ions (-0.442 , -0.686 , and -0.510 eV) on each monolayer was much stronger than that of Li ions (-0.062 , -0.361 , and -0.352 eV). However, the adsorption energy of Li/Na is obviously weaker

than that of MXenes with similar Sc_2C ($-0.31/-0.61$ eV), Ti_2C ($-0.721/-0.79$ eV), and V_2C ($-0.96/-1.16$ eV). With the increase of the concentration of Li/Na ions on the three monolayers, all OCVs fall in the range of 0–1 V, which can effectively inhibit the dendrite formation of Li/Na metal. In addition, the average adsorption energies of several Li/Na ions on ScB, TiB, and VB monolayers were calculated. It can be seen that the adsorption strength of Li ions on TiB and VB monolayers is much stronger than that of Na ions. Researchers have shown that ScB and TiB monolayers, as anode materials of LIBs and SIBs, have better electrochemical performance than other MBenes. Wei et al. [84] recently calculated the possibility of V_2B_2 as anode material for sodium ion battery separately. V_2B_2 has excellent Na^+ adsorption characteristics, and can absorb three layers of Na^+ nearby, with a maximum capacity of 814 mAh g^{-1} . It is found that V_2B_2 has an ultra-low diffusion barrier (0.011 eV), which represents the ultra-high ion diffusion rate of Na ions on V_2B_2 surface. The average OCV is 0.65 V, and the good metallicity is maintained during the whole adsorption process of sodium ions. These performances are superior to some MBenes that have been studied.

The above is just a theoretical calculation to predict the excellent performance of different MBenes in the field of ion batteries. More recently, Xiong's team [85] prepare MoB by fluorine-free hydrothermal method, and test the electrochemical performance of MoB as a lithium ion battery in CR-2032 coin half battery. Figure 22a shows the cyclic voltammetry (CV) curve of MoB in the voltage window of $0.01-3$ V and Li/Li^+ . The redox peak at $1.20/1.49$ V still appears during the second and third cycles, which is attributed to the intercalation/deintercalation of lithium ions, indicating that this is a reversible process. Figure 22b shows the cycle stability and coulomb efficiency of MoAIB and MBene. At the current density of 50 mAh g^{-1} , the original MoAIB has almost no capacity, but the specific capacity of the negative electrode of MBene reaches 671.6 mAh g^{-1} after 50 cycles, which indicates that the removal of aluminum atoms from MAB phase is beneficial to improve the electrochemical performance. Figure 22c shows the charge–discharge curve of MBene with current density of 50 mAh g^{-1} in the voltage range of $0.01-3$ V. The initial charge–discharge specific capacities are 659.3 and 701.7 mAh g^{-1} , respectively. The corresponding small irreversible capacity in the first cycle is attributed to the formation of SEI layer, which is consistent

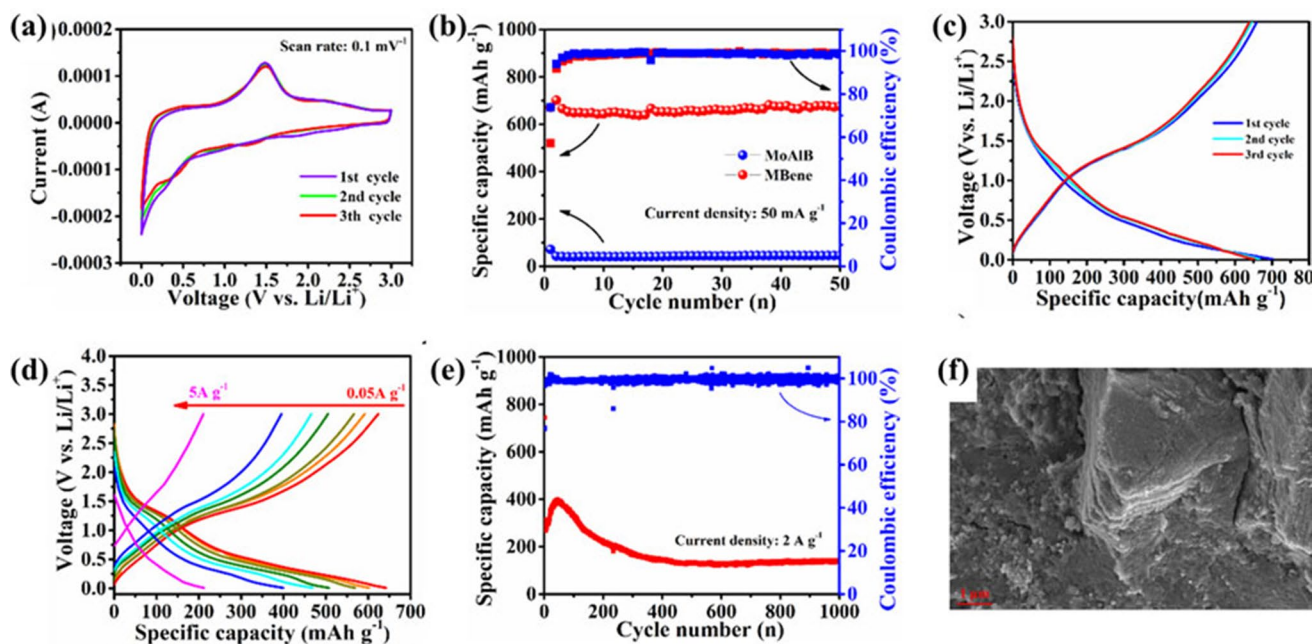


Fig. 22 Electrochemical performance of the 2D MoB MBene anodes in LIBs. **a** CV curves at a scan rate of 0.1 mVs^{-1} . **b** The cycle performance of MoAIB and 2D MoB MBene at 50 mA g^{-1} . **c** Charge–discharge curves at 50 mA g^{-1} . **d** The corresponding voltage curves of 2D MoB MBene and **e** long cycle performance at 2 mA g^{-1} . **f** SEM images of the surface morphology of 2D MoB MBene anode after electrochemical cycle. Reproduced with permission from Ref. [85]

with the results of cyclic voltammetry. With a capacity of 0.05 A g^{-1} as a reference, the capacity retention rates are 93.8%, 88.6%, 79.1%, 73.1%, 62.1%, and 33.1% at a current density of 0.1 A g^{-1} (Fig. 22d), respectively. At the current density of 2 A g^{-1} , the reversible specific capacity after 1000 cycles is 144.2 mAh g^{-1} (Fig. 22e), which is higher than that of many reported MXenes anodes [242–244]. The surface morphology of two-dimensional MoB MBene electrode after electrochemical cycle is shown in Fig. 22f. After long-term

electrochemical cycle, the morphology of 2D MoB remains unchanged, indicating that the structure of 2D MoB is stable during charge and discharge. The above results show that MoB has excellent performance as anode material of LIBs, and MBene material will attract great research attention and become the next generation star material.

Rechargeable magnesium battery is becoming one of the most promising alternatives because of their mild nature, high natural abundance, good atmospheric stability, low

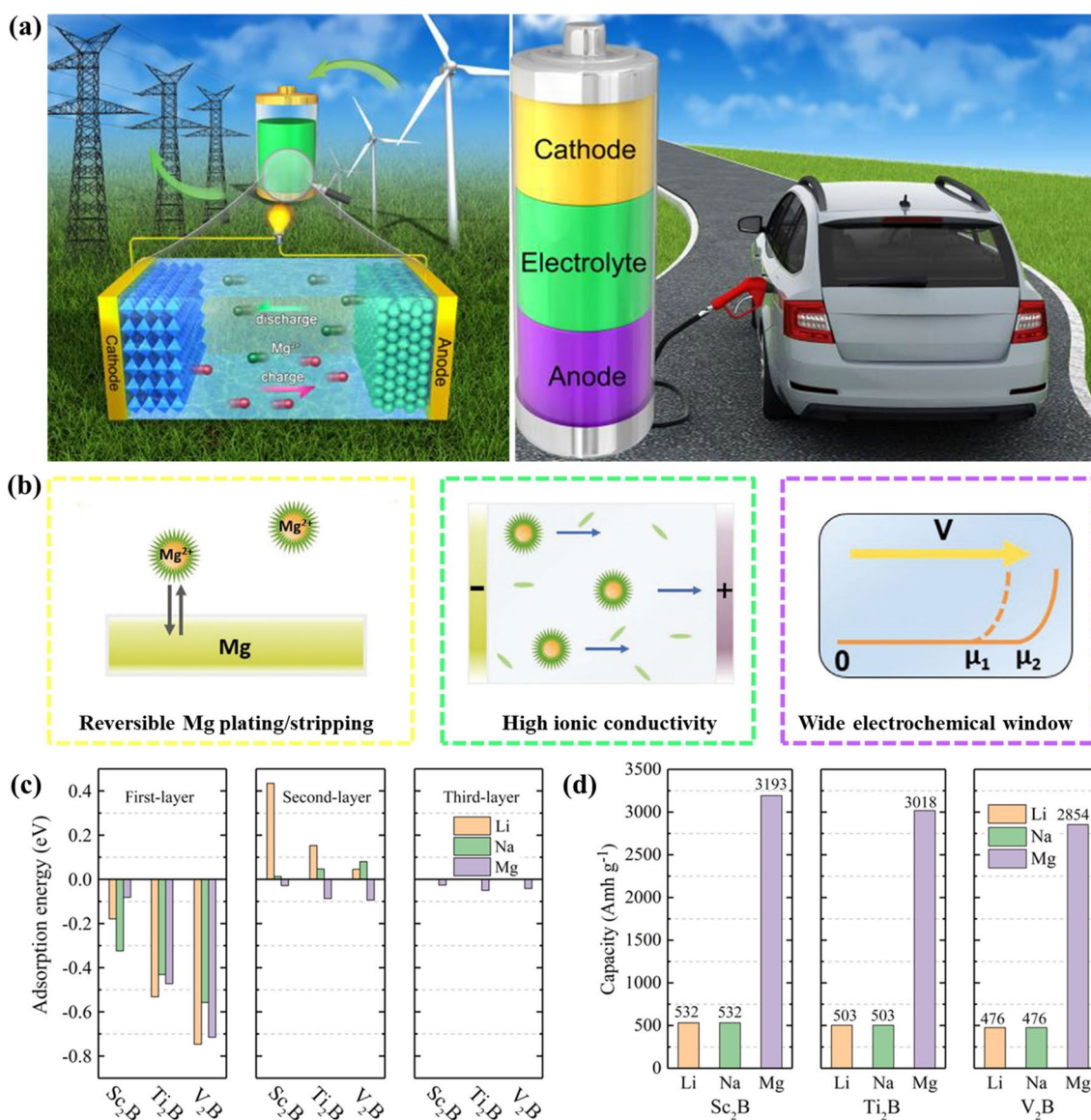


Fig. 23 **a** Schematic illustration of rechargeable magnesium battery. Reproduced with permission from Ref. [245]. **b** Schematic illustration of main prerequisites for MIBs electrolytes. Reproduced with permission from Ref. [246]. **c** The average adsorption energies for cations (cation = Li, Na and Mg) on M_2B at first layer, second layer and third layer. **d** Theoretical specific capacity of cations (cation = Li, Na and Mg) in M_2B (M = Sc, Ti and V) monolayer. Reproduced with permission from Ref. [233]

cost, and environmental friendliness. Magnesium ion battery basically consists of four parts: positive electrode, negative electrode, electrolyte and separator. Energy storage in MIBs is achieved through electrochemical reactions associated with electron and ion transport (Fig. 23a). During the discharge process, electrons generated by redox reaction drive the external load. On the contrary, during charging, electrons are stored in the electrode through reversible electrochemical reaction. Therefore, the reversible capacity provided by magnesium ion batteries is mainly limited to the exchanged electrons, the structural stability of materials during intercalation/delamination, and the diffusion rate controlled by electrolyte. At this point, the performance of electrode materials and electrolyte determines the performance of the battery, which is the key factor of high performance. The electrolyte should have the following characteristics: (1) reversible deposition and dissolution of Mg; (2) high ionic conductivity; (3) wide electrochemical window (Fig. 23b). In recent years, the exploration of suitable two-dimensional electrode materials has aroused researchers' interest.

Li et al. [227] firstly evaluated MBenes as potential anode materials for MIBs based on DFT calculations. The simulation results showed that Cr_2B_2 is a competitive anode material with a maximum theoretical capacity of 853.4 mAh g^{-1} and an average open-circuit potential of 0.53 eV . Compared with Cr_2B_2 , Mo_2B_2 has a weaker Mg storage capacity with maximum storage capacity of 502.1 mAh g^{-1} . The energy barriers of magnesium in Cr_2B_2 and Mo_2B_2 are 0.38 and 0.84 eV , respectively. These excellent physical properties mean that 2D MBenes have good prospects for application in MIBs as anode materials. Recently, Ma et al. [233] explored three new 2D MBenes phases, Sc_2B , Ti_2B , and V_2B , as electrode for MIBs. The adsorption energy of Li, Na and Mg on the M_2B are appeared in Fig. 23c. When the third layer of Mg ions is adsorbed on the surface of M_2B , the adsorption energies are -0.026 , -0.049 , and -0.041 eV for Sc_2B , Ti_2B , and V_2B , respectively, which indicates that the interaction between adsorbed atoms and the substrate is weak. However, the adsorption energies of Li and Na atoms in the second layer are positive, not to mention the third layer. The theoretical capacities of Sc_2B , Ti_2B , and V_2B as electrodes of MIBs are 3192.813 , 3018.414 , and $2853.953 \text{ mAh g}^{-1}$, respectively (Fig. 23d). In addition, the open circuit voltage of M_2B is in the range of 0.023 – 0.748 V , which improves the safety performance of the battery. As an anode material for MIBs, M_2B ($M = \text{Sc}, \text{Ti}, \text{V}$) have high theoretical

specific capacity, low open-circuit voltage and diffusion energy barrier.

5.2 Problems Solved in Lithium–Sulfur Batteries

Lithium-sulfur battery is considered as one of the next generation high energy density energy storage devices with the greatest development potential. Compared with traditional lithium-ion batteries, lithium-sulfur batteries (LSBs) have important advantages: lower material price and lighter weight. Increasing energy density is very important in transportation and energy manufacturing to reduce energy storage costs and greenhouse gas emissions. However, there are several challenges that hinders the development of LSBs, such as the poor conductivity of sulfur cathodes, the shuttling effect and the sluggish decomposition of Li_2S clusters [247, 248]. The shuttle effect of soluble lithium polysulfide (LiPS) will cause some negative effects on the corresponding components in the path (Fig. 24a). When searching for suitable electrode materials for metal ion batteries, the structural stability, electronic conductivity, adsorption and storage properties, ion transport, open circuit voltage and capacity of the battery are usually considered. In addition, the anchoring effect of the material may need to be considered when selecting a suitable material for LSBs. Xiao et al. [249] believed that Mo_2B_2 surface functionalization can obtain appropriate anchoring energy to inhibit the shuttle effect in LSBs, and can be further modified by adjusting surface groups. At the same time, further electronic structure results showed that the functionalized MBenes still show good electronic conductivity after LiPSs adsorption, which provides an electronic pathway to stimulate the redox electrochemistry of LiPSs. The specific analysis process is as follows.

To investigate the anchoring behavior, the structure of bare Mo_2B_2 MBenes was first optimized and found to be composed of Mo-B-B-Mo atoms stacked. The anchoring material needs to have excellent anchoring properties for LiPS in order to suppress the shuttle effect. Therefore, a preliminary simulation of the adsorption behavior of LiPS on bare Mo_2B_2 MBenes was performed, and it was found that most of the sulfur atoms were unloaded on the surface of Mo_2B_2 MBenes, leading to the structural collapse of LiPSs. This meant that the direct use of bare Mo_2B_2 MBenes as the anchoring material for LiPSs will seriously hinder the charge/discharge cycle performance of the battery. In order to obtain reversible charge/discharge



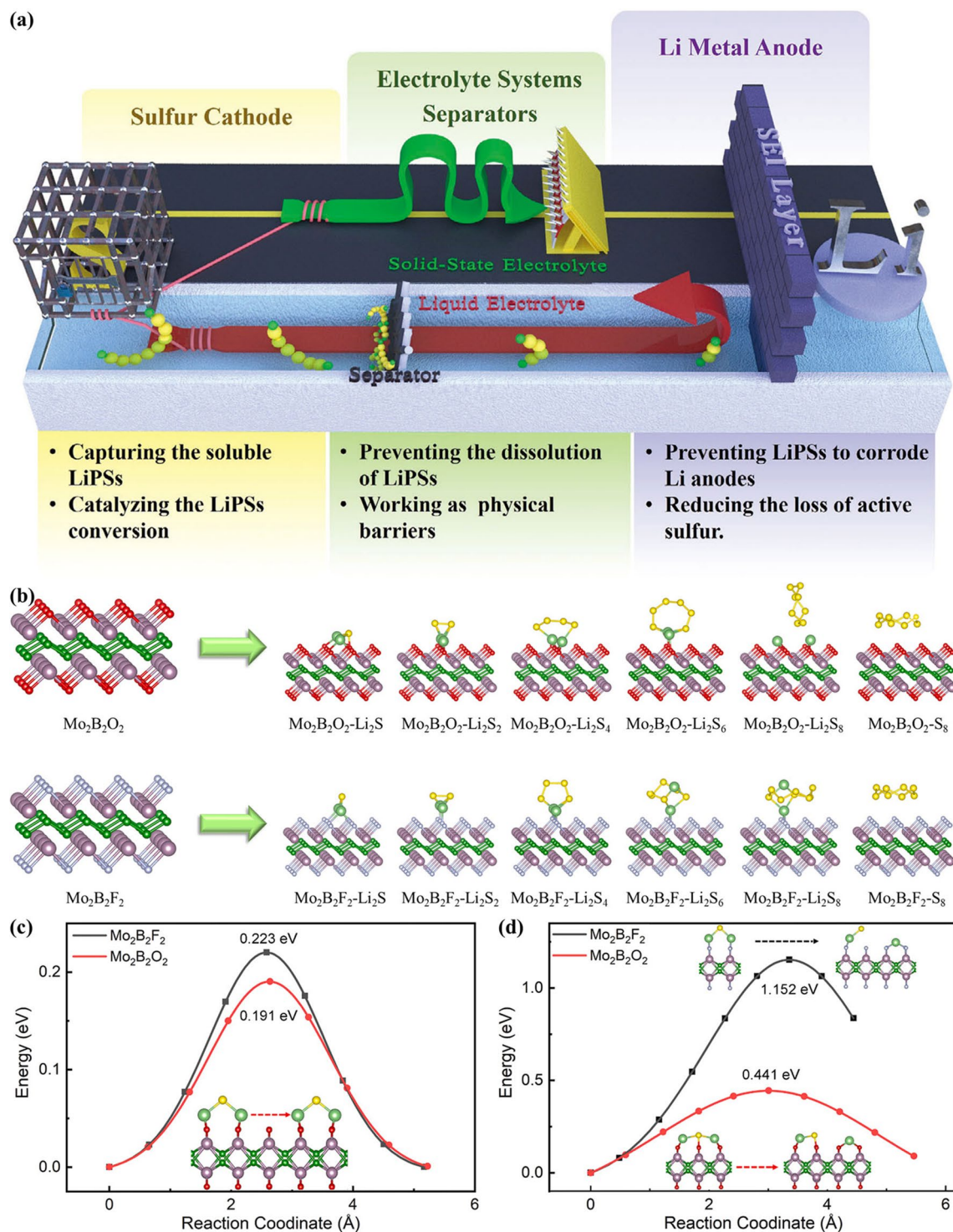


Fig. 24 **a** Schematic illustrations of the strategies and operation mechanisms of the modified sulfur host, electrolyte systems, functional separators, and anode surface engineering for the inhibition of LiPSs shuttle. Reproduced with permission from Ref. [250]. **b** Left: Optimized structures of $\text{Mo}_2\text{B}_2\text{O}_2$ and $\text{Mo}_2\text{B}_2\text{F}_2$. Right: The most energetic favorable adsorption configuration of Li_2S_n ($n = 1, 2, 4, 6$ and 8) and S_8 on the surface of $\text{Mo}_2\text{B}_2\text{O}_2$ MBene and $\text{Mo}_2\text{B}_2\text{F}_2$ MBene. The purple, green, sky blue, red, yellow, and moss green spheres represent Mo, B, F, O, S, and Li atoms, respectively. The calculated energy curves of Li_2S **c** diffusion and **d** decomposition on the surfaces of $\text{Mo}_2\text{B}_2\text{F}_2$ (black line) and $\text{Mo}_2\text{B}_2\text{O}_2$ (red line). Reproduced with permission from Ref. [249]. (Color figure online)

cycle performance, researchers suggested the modification of bare Mo_2B_2 by surface functionalization (F/O atoms), and initial adsorption forms of LiPSs on functionalized MBenes were extensively investigated. The most favorable adsorption conformations of S_8 and LiPSs on MBenes are shown in Fig. 24b. The result showed that $\text{Mo}_2\text{B}_2\text{O}_2$ and $\text{Mo}_2\text{B}_2\text{F}_2$ are significantly weaker in anchoring strength with LiPS and S_8 compared to bare Mo_2B_2 MBene, and the structure is well maintained. Finally, the researchers studied that $\text{Mo}_2\text{B}_2\text{O}_2$ exhibits a lower diffusion barrier (0.191 eV) and decomposition barrier of Li_2S clusters (0.441 eV), which is beneficial for achieving coulombic efficiency of LSBs (Fig. 24c, d).

6 Summary and Perspectives

Since derived by extracting Al from MAB phases, MBenes have received more focus owing to their various chemical and structural types and potential applications. At present, researchers have obtained 2D MBenes through two different methods in experiments. Alameda et al. [87] found that $\text{Mo}_2\text{Al}_2\text{B}_2$ can react with NaOH at room temperature to cause Al deintercalation. In addition, the results of theoretical calculations further confirm the excellent conductivity and high mechanical strength of MBenes. Very recently, Xiong's team [85] prepare MoB by fluorine-free

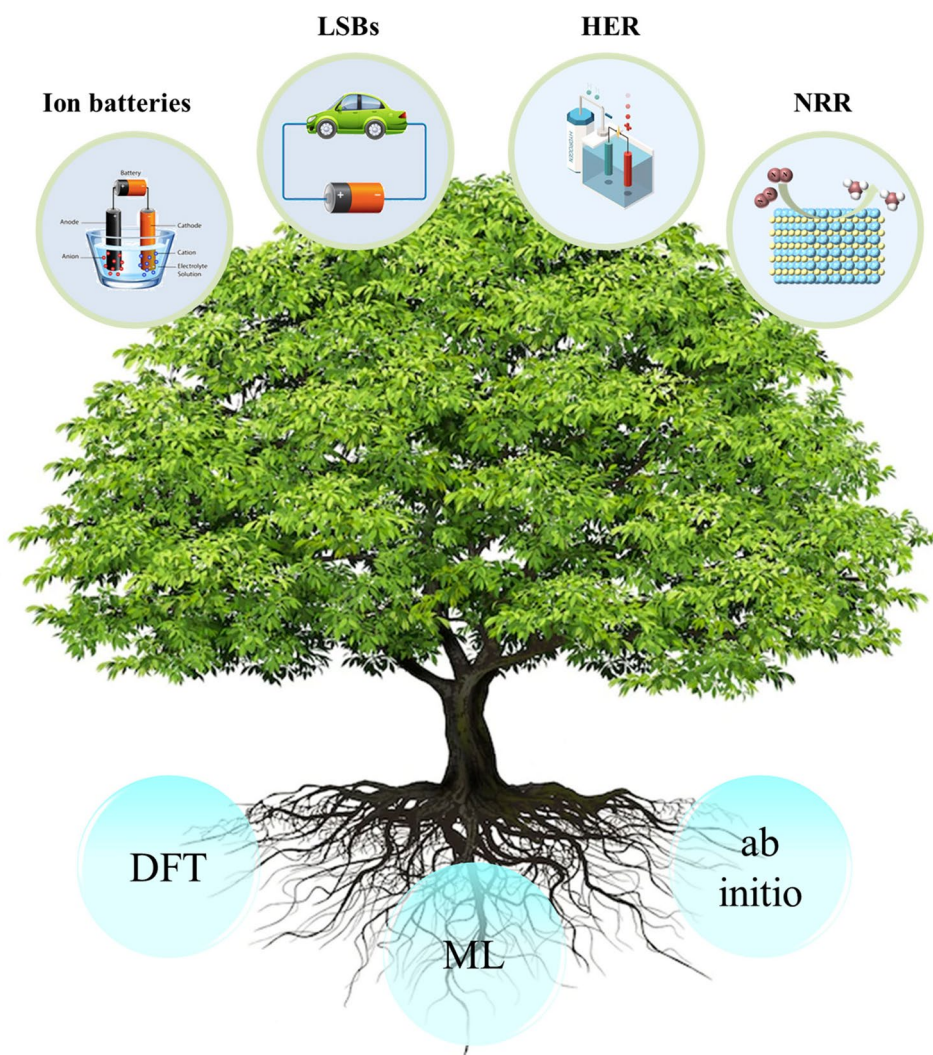


Fig. 25 Main applications of MBenes in energy storage and conversion with theoretical calculation

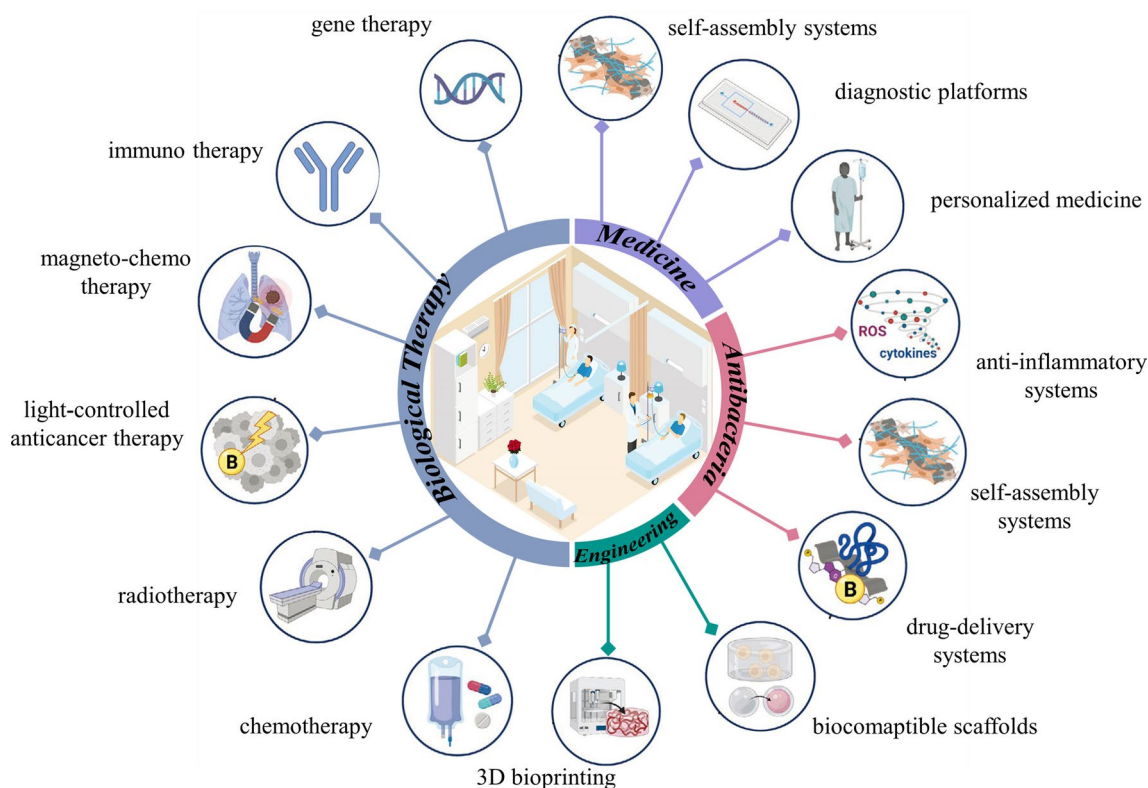


Fig. 26 Envisioned biotechnological potential of 2D MBenes. Reproduced with permission from Ref. [95]

hydrothermal method, and study electrochemical performance of MoB in LIBs.

The main focus is on the energy conversion and energy storage applications in the rechargeable batteries (Fig. 25). As a new class of 2D nanomaterials, MBenes have a broad application prospect as an electrocatalyst for HER and NRR. In addition, it is also an attractive way to modify the structure of MBenes to improve its activity. The review also emphasizes MBenes composites embedded by single metal, which shows fascinating properties due to the electrochemical properties and high activity of MBenes and monatomic respectively. Besides electrocatalytic HER and NRR, MBene catalysts are also new catalysts for carbon dioxide reduction and nitric oxide reduction. Obviously, more efforts need to be made in this field in the future. We also focus on the research progress of MBenes for energy storage applications. It is observed that MBenes show great potential as anode materials in the next generation of batteries. Recently, researchers also found MBenes with the highest biotechnological potential and the lowest cyto- and ecotoxicological threats possess prospective application in biotechnological field [95] (Fig. 26).

Although the enormous potential of MBenes in the application of energy storage (Fig. 27a) and conversion (Fig. 27b) has been theoretically verified so far, there are still some challenges and opportunities for the further development of MBenes, some of which are highlighted as follows. Generally speaking, the synthesis, properties and application of MBenes are still in its infancy. More efforts are needed in the future to conduct a comprehensive and thorough investigation of MBenes.

- i. It is theoretically predicted that many MBenes have good stability, but the corresponding precursors have not been found or produced. It is worth noting that all the existing stable MBenes are early transition metal boron, while MBenes composed of intermediate or late transition metals are expected to be synthesized and explored. In addition, compared with the synthetic route of MXenes, the synthesis of MBenes have great room for improvement and development. In the preparation of MBene nanosheets, ensuring the consistency of morphology and physicochemical properties of the products is the main challenge faced by large-scale preparation. In addition, the researchers focused on

the electronic structure, elasticity and magnetism of M_2AIB_2 phase. The other two groups of MAB (including MAIB and M_3AIB_4 phase) and related MBenes have not been investigated. Therefore, it is necessary to systematically study the structure and properties of MAIB, M_2AIB_2 , M_3AIB_4 and their derived MBenes. At the same time, it is also hoped that the assembly of polymers similar to MXenes will appear (Fig. 27c).

- ii. In order to understand the mechanism of MBene as a catalyst and anode material, and to design new materials and optimize their performance, attention should be paid to theoretical calculation and experimental verification, such as field instrumental characterization, so as to produce practical applications. In addition, the catalytic mechanism of CO_2RR and NRR is still unclear. Because of the complexity of the catalytic reaction process between CO_2RR and NRR, there are many products in CO_2RR with different reaction pathways, and the reaction pathway of NRR is still controversial. So far, it has been challenging to determine the exact mechanism. First of all, it is necessary to understand the actual active sites in 2D MBenes in response to electrocatalysis, which is very important for the application of effective and practical engineer-

ing technology. Although a great deal of theoretical calculation and experimental work has been done, up to now, no exact conclusion has been reached on the actual active center of catalytic reaction. Therefore, systematic research is needed to further clarify the specific active sites of different catalytic reactions. Theoretical prediction and simultaneous measurement of catalytic activity and selectivity under practical working conditions seem to be a promising direction in this field.

- iii. The potential of MBenes in modern biotechnology stems from their unique structure and specific chemical composition. The experience gained from other 2D materials, especially MXenes, can give researchers a reasonable way to explore the biological and biotechnological properties of MBenes. It is essential to study the morphological, structural and physicochemical transformations of MBenes in relevant biological environments. We envisage that 2D MBenes have great biotechnological potential, and its practical biological applications will develop rapidly (Fig. 27d). In the next few years, the interesting biological activity and functional characteristics of MBenes are expected to develop rapidly.

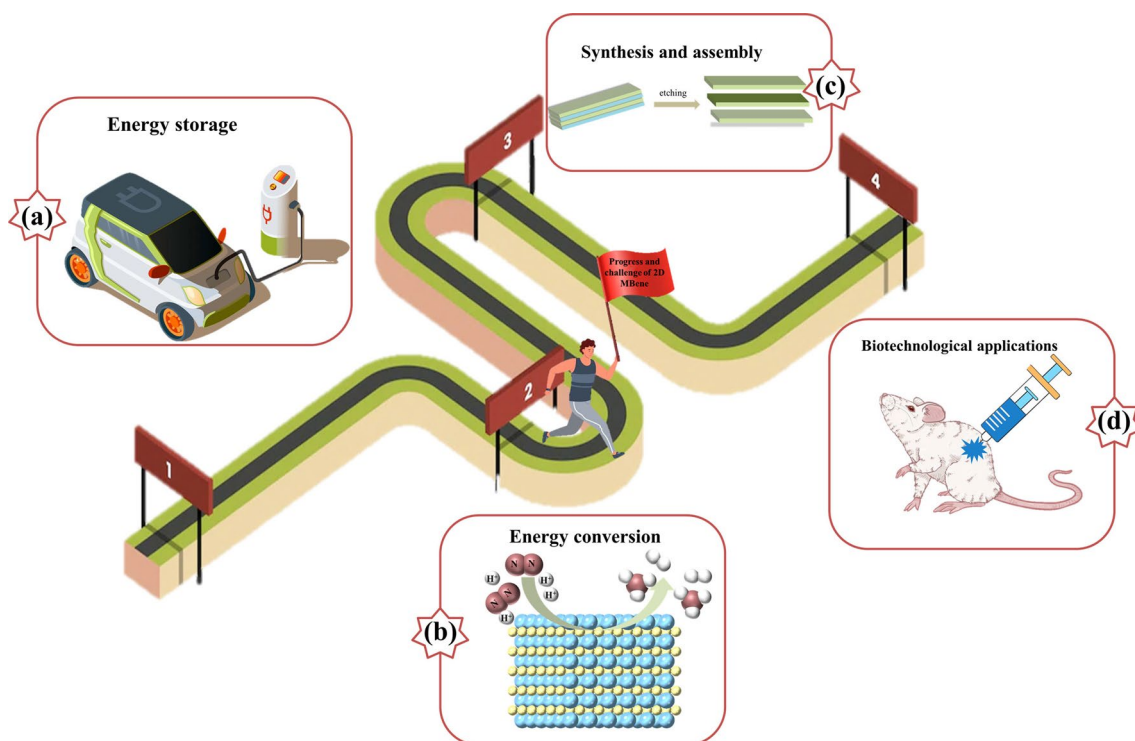


Fig. 27 Progress and challenges of 2D MBene materials. The main progress of MBenes in **a** energy storage and **b** conversion. Prospect of future application of MBenes in **c** synthesis and **d** biotechnology

Two-dimensional MBenes have attracted focus due to their unique structural types and excellent electrical and mechanical properties and have developed into a member of the two-dimensional family. It has also been proven to have great application potential in the field of energy conversion and storage. It is foreseeable that 2D MBenes have the potential to become the brightest material.

Funding Open access funding provided by Shanghai Jiao Tong University.

Open Access This article is licensed under a Creative Commons Attribution 4.0 International License, which permits use, sharing, adaptation, distribution and reproduction in any medium or format, as long as you give appropriate credit to the original author(s) and the source, provide a link to the Creative Commons licence, and indicate if changes were made. The images or other third party material in this article are included in the article's Creative Commons licence, unless indicated otherwise in a credit line to the material. If material is not included in the article's Creative Commons licence and your intended use is not permitted by statutory regulation or exceeds the permitted use, you will need to obtain permission directly from the copyright holder. To view a copy of this licence, visit <http://creativecommons.org/licenses/by/4.0/>.

References

1. V. Dusastre, L. Martiradonna, Materials for sustainable energy. *Nat. Mater.* **16**, 15 (2017). <https://doi.org/10.1038/nmat4838>
2. J. Tian, Q. Xue, Q. Yao, N. Li, C.J. Branes et al., Inorganic halide perovskite solar cells: progress and challenges. *Adv. Energy Mater.* **10**(23), 2000183 (2020). <https://doi.org/10.1002/aenm.202000183>
3. Q.A. Akkerman, M. Gandini, F.D. Stasio, P. Rastogi, F. Palazon et al., Strongly emissive perovskite nanocrystal inks for high-voltage solar cells. *Nat. Energy* **2**(2), 16194 (2017). <https://doi.org/10.1038/nenergy.2016.194>
4. A. Barre, B. Deguilhem, S. Grolleau, M. Gérard, F. Suard et al., A review on lithium-ion battery ageing mechanisms and estimations for automotive applications. *J. Power Sources* **241**, 680–689 (2013). <https://doi.org/10.1016/j.jpowsour.2013.05.040>
5. Y. Wang, B. Liu, Q. Li, S. Cartmell, S. Ferrara et al., Lithium and lithium ion batteries for applications in microelectronic devices: a review. *J. Power Sources* **286**, 330–345 (2015). <https://doi.org/10.1016/j.jpowsour.2015.03.164>
6. L. Jin, C. Shen, A. Shellikeri, Q. Wu, J. Zheng et al., Progress and perspectives on pre-lithiation technologies for lithium ion capacitors. *Energy Environ. Sci.* **13**(8), 2341–2362 (2020). <https://doi.org/10.1039/d0ee00807a>
7. A. Noori, M.F. El-Kady, M.S. Rahmanifar, R.B. Kaner, M.F. Mousavi, Towards establishing standard performance metrics for batteries, supercapacitors and beyond. *Chem. Soc. Rev.* **48**(5), 1272–1341 (2019). <https://doi.org/10.1039/c8cs00581h>
8. M. Soltani, S.H. Beheshti, A comprehensive review of lithium ion capacitor: development, modelling, thermal management and applications. *J. Energy Storage* **34**, 102019 (2021). <https://doi.org/10.1016/j.est.2020.102019>
9. N.S. Choi, Z. Chen, S.A. Freunberger, X. Ji, Y. Sun et al., Challenges facing lithium batteries and electrical double-layer capacitors. *Angew. Chem. Int. Ed.* **51**(40), 9994–10024 (2012). <https://doi.org/10.1002/anie.201201429>
10. F. Bonaccorso, L. Colombo, G. Yu, M. Stoller, V. Tozzini et al., Graphene, related two-dimensional crystals, and hybrid systems for energy conversion and storage. *Science* **347**(6217), 1246501 (2015). <https://doi.org/10.1126/science.1246501>
11. P. Kumar, A. Dey, J. Roques, L. Assaud, S. Franger et al., Photoexfoliation synthesis of 2D materials. *ACS Mater. Lett.* **4**(2), 263–270 (2022). <https://doi.org/10.1021/acsmaterlett.1c00651>
12. W. Qian, S. Xu, X. Zhang, C. Li, W. Yang et al., Differences and similarities of photocatalysis and electrocatalysis in two-dimensional nanomaterials: strategies, traps, applications and challenges. *Nano-Micro Lett.* **13**, 156 (2021). <https://doi.org/10.1007/s40820-021-00681-9>
13. D. Chen, W. Chen, L. Ma, G. Ji, K. Chang et al., Graphene-like layered metal dichalcogenide/graphene composites: synthesis and applications in energy storage and conversion. *Mater. Today* **17**(4), 184–193 (2014). <https://doi.org/10.1016/j.mattod.2014.04.001>
14. M. Houssa, A. Dimoulas, A. Molle, Silicene: a review of recent experimental and theoretical investigations. *J. Phys. Condens. Matter.* **27**(25), 253002 (2015). <https://doi.org/10.1088/0953-8984/27/25/253002>
15. J. Gao, J. Zhang, H. Liu, Q. Zhang, J. Zhao et al., Structures, mobilities, electronic and magnetic properties of point defects in silicene. *Nanoscale* **5**(20), 9785–9792 (2013). <https://doi.org/10.1039/c3nr02826g>
16. V.V. Kulish, O.I. Malyi, C. Persson, P. Wu, Adsorption of metal adatoms on single-layer phosphorene. *Phys. Chem. Chem. Phys.* **17**(2), 992–1000 (2015). <https://doi.org/10.1039/c4cp03890h>
17. L. Kou, T. Frauenheim, C. Chen, Phosphorene as a superior gas sensor: selective adsorption and distinct I-V response. *J. Phys. Chem. Lett.* **5**(15), 2675–2681 (2014). <https://doi.org/10.1021/jz501188k>
18. G. Tai, T. Hu, Y. Zhou, X. Wang, J. Kong et al., Synthesis of atomically thin boron films on copper foils. *Angew. Chem. Int. Ed.* **54**(51), 15473–15477 (2015). <https://doi.org/10.1002/anie.201509285>
19. A.J. Mannix, X.F. Zhou, B. Kiraly, J.D. Wood, D. Alducin et al., Synthesis of borophenes: anisotropic, two-dimensional boron polymorphs. *Science* **350**(6267), 1513–1516 (2015). <https://doi.org/10.1126/science.aad1080>
20. C. Hou, G. Tai, J. Hao, L. Sheng, B. Liu et al., Ultrastable crystalline semiconducting hydrogenated borophene. *Angew.*

- Chem. Int. Ed. **59**(27), 10819–10825 (2020). <https://doi.org/10.1002/anie.202001045>
21. S. Chahal, P. Ranjan, M. Motlag, S.S.R.K.C. Yamijala, D.J. Late et al., Borophene via micromechanical exfoliation. *Adv. Mater.* **33**(34), 2102039 (2021). <https://doi.org/10.1002/adma.202102039>
22. P. Ranjan, J.M. Lee, P. Kumar, A. Vinu, Borophene: new sensation in flatland. *Adv. Mater.* **32**(34), 2000531 (2020). <https://doi.org/10.1002/adma.202000531>
23. M. Ou, X. Wang, L. Yu, C. Liu, W. Tao et al., The emergence and evolution of borophene. *Adv. Sci.* **8**(12), 2001801 (2021). <https://doi.org/10.1002/advsc.202001801>
24. E. Lee, Y.S. Yoon, D.J. Kim, Two-dimensional transition metal dichalcogenides and metal oxide hybrids for gas sensing. *ACS Sens.* **3**(10), 2045–2060 (2018). <https://doi.org/10.1021/acssensors.8b01077>
25. R. Lv, J.A. Robinson, R.E. Schaak, D. Sun, Y. Sun et al., Transition metal dichalcogenides and beyond: synthesis, properties, and applications of single- and few-layer nanosheets. *Acc. Chem. Res.* **48**(1), 56–64 (2015). <https://doi.org/10.1021/ar5002846>
26. S. Chahal, S.M. Kaulzarich, P. Kumar, Microwave synthesis of hematene and other two-dimensional oxides. *ACS Mater. Lett.* **3**(5), 631–640 (2021). <https://doi.org/10.1021/acsmaterialslett.1c00102>
27. H. Xie, Z. Li, L. Cheng, A.A. Haidry, J. Tao et al., Recent advances in the fabrication of 2D metal oxides. *Isience* **25**(1), 103598 (2022). <https://doi.org/10.1016/j.isci.2021.103598>
28. H.S. Gujral, G. Singh, A.V. Baskar, X. Guan, X. Geng et al., Metal nitride-based nanostructures for electrochemical and photocatalytic hydrogen production. *Sci. Technol. Adv. Mater.* **23**(1), 76–119 (2022). <https://doi.org/10.1080/14686996.2022.2029686>
29. P.M. Bodhankar, P.B. Sarawade, P. Kumar, A. Vinu, A.P. Kulkarni et al., Nanostructured metal phosphide based catalysts for electrochemical water splitting: a review. *Small* **18**(21), 2107572 (2022). <https://doi.org/10.1002/smll.202107572>
30. S. Chahal, A. Bandyopadhyay, S.P. Dash, P. Kuma, Microwave synthesized 2D gold and its 2D–2D hybrids. *J. Phys. Chem. Lett.* **13**(28), 6487–6495 (2022). <https://doi.org/10.1021/acs.jpcclett.2c01540>
31. M. Naguib, M. Kurtoglu, V. Presser, J. Lu, J. Niu et al., Two-dimensional nanocrystals produced by exfoliation of Ti_3AlC_2 . *Adv. Mater.* **23**(37), 4248–4253 (2011). <https://doi.org/10.1002/adma.201102306>
32. M. Naguib, O. Mashtalir, J. Carle, V. Presser, J. Lu et al., Two-dimensional transition metal carbides. *ACS Nano* **6**(2), 1322–1331 (2012). <https://doi.org/10.1021/nn204153h>
33. A.L. Ivanovskii, A.N. Enyashin, Graphene-like transition-metal nanocarbides and nanonitrides. *Russ. Chem. Rev.* **82**(8), 735–746 (2013). <https://doi.org/10.1070/RC2013v082n08ABEH004398>
34. T. Hu, J. Wang, H. Zhang, Z. Li, M. Hu et al., Vibrational properties of Ti_3C_2 and $\text{Ti}_3\text{C}_2\text{T}_2$ ($\text{T} = \text{O}, \text{F}, \text{OH}$). Monosheets by first-principles calculations: a comparative study. *Phys. Chem. Chem. Phys.* **17**(15), 9997–10003 (2015). <https://doi.org/10.1039/c4cp05666c>
35. X. Jiang, A.V. Kuklin, A. Baev, Y. Ge, H. Ågren et al., Two-dimensional MXenes: from morphological to optical, electric, and magnetic properties and applications. *Phys. Rep. Rev. Sect. Phys. Lett.* **848**, 1–58 (2020). <https://doi.org/10.1016/j.physrep.2019.12.006>
36. Z. He, H. Xie, H. Wu, J. Chen, S. Ma et al., Recent advances in MXene/polyaniline-based composites for electrochemical devices and electromagnetic interference shielding applications. *ACS Omega* **6**(35), 22468–22477 (2021). <https://doi.org/10.1021/acsomega.1c02996>
37. F. Jamil, H.M. Ali, M.M. Janjua, MXene based advanced materials for thermal energy storage: a recent review. *J. Energy Storage* **35**, 102322 (2021). <https://doi.org/10.1016/j.est.2021.102322>
38. J.C. Lei, X. Zhang, Z. Zhou, Recent advances in MXene: preparation, properties, and applications. *Front. Phys.* **10**(3), 276–286 (2015). <https://doi.org/10.1007/s11467-015-0493-x>
39. H. Lin, X. Wang, L. Yu, Y. Chen, J. Shi, Two-dimensional ultrathin MXene ceramic nanosheets for photothermal conversion. *Nano Lett.* **17**(1), 384–391 (2017). <https://doi.org/10.1021/acs.nanolett.6b04339>
40. K. Zhu, H. Zhang, K. Ye, W. Zhao, J. Yan et al., Two-dimensional titanium carbide MXene as a capacitor-type electrode for rechargeable aqueous Li-ion and Na-ion capacitor batteries. *ChemElectroChem* **4**(11), 3018–3025 (2017). <https://doi.org/10.1002/celec.201700523>
41. D. Wei, W. Wu, J. Zhu, C. Wang, C. Zhao et al., A facile strategy of polypyrrole nanospheres grown on Ti_3C_2 -MXene nanosheets as advanced supercapacitor electrodes. *J. Electroanal. Chem.* **877**, 114538 (2020). <https://doi.org/10.1016/j.jelechem.2020.114538>
42. J. Fu, L. Li, D. Lee, J.M. Yun, B.K. Ryu et al., Enhanced electrochemical performance of $\text{Ti}_3\text{C}_2\text{T}_x$ MXene film based supercapacitors in $\text{H}_2\text{SO}_4/\text{KI}$ redox additive electrolyte. *Appl. Surf. Sci.* **504**, 144250 (2020). <https://doi.org/10.1016/j.apsusc.2019.144250>
43. M.R. Lukatskaya, O. Mashtalir, C.E. Ren, Y. Dall’Agnese, P.L. Taberna et al., Cation intercalation and high volumetric capacitance of two-dimensional titanium carbide. *Science* **341**(6153), 1502–1505 (2013). <https://doi.org/10.1126/science.1241488>
44. Y. Dall’Agnese, P. Rozier, P.L. Taberna, Y. Gogotsi, P. Simon et al., Capacitance of two-dimensional titanium carbide (MXene) and MXene/carbon nanotube composites in organic electrolytes. *J. Power Sources* **306**, 510–515 (2016). <https://doi.org/10.1016/j.jpowsour.2015.12.036>
45. L. Li, J. Wen, X. Zhang, Progress of two-dimensional $\text{Ti}_3\text{C}_2\text{T}_x$ in supercapacitors. *Chemsuschem* **13**(6), 1296–1329 (2020). <https://doi.org/10.1002/cssc.201902679>
46. Y. Tian, Y. An, J. Feng, Flexible and freestanding silicon/MXene composite papers for high-performance lithium-ion

- batteries. *ACS Appl. Mater. Interfaces* **11**(10), 10004–10011 (2019). <https://doi.org/10.1021/acsami.8b21893>
47. J. Jyoti, B.P. Singh, M. Sandhu, S.K. Tripath, New insights on MXene and its advanced hybrid materials for lithium-ion batteries. *Sustain. Energy Fuels* **6**(4), 971–1013 (2022). <https://doi.org/10.1039/d1se01681d>
48. S. Sun, Z. Xie, Y. Yan, S. Wu, Hybrid energy storage mechanisms for sulfur-decorated Ti_3C_2 MXene anode material for high-rate and long-life sodium-ion batteries. *Chem. Eng. J.* **366**, 460–467 (2019). <https://doi.org/10.1016/J.cej.2019.01.185>
49. Y. Zhang, C. Ma, W. He, C. Zhang, C. Zhang et al., MXene and MXene-based materials for lithium-sulfur batteries. *Prog. Nat. Sci. Mater. Int.* **31**(4), 501–513 (2021). <https://doi.org/10.1016/J.pnsc.2021.07.003>
50. M.K. Aslam, Y. Niu, M. Xu, MXenes for non-lithium-ion (Na, K, Ca, Mg, and Al) batteries supercapacitors. *Adv. Energy Mater.* **11**(2), 2000681 (2021). <https://doi.org/10.1002/aenm.202000681>
51. J. Luo, J. Zheng, J. Nai, C. Jin, H. Yuan et al., Atomic sulfur covalently engineered interlayers of Ti_3C_2 MXene for ultra-fast sodium-ion storage by enhanced pseudocapacitance. *Adv. Funct. Mater.* **29**(10), 1808107 (2019). <https://doi.org/10.1002/adfm.201808107>
52. Y. Wang, X. Wang, X. Li, Y. Bai, H. Xiao et al., Scalable fabrication of polyaniline nanodots decorated MXene film electrodes enabled by viscous functional inks for high-energy-density asymmetric supercapacitors. *Chem. Eng. J.* **405**, 126664 (2021). <https://doi.org/10.1016/J.cej.2020.126664>
53. M. Inagaki, F. Kang, Graphene derivatives: graphane, fluorographene, graphene oxide, graphyne and graphdiyne. *J. Mater. Chem. A* **2**(33), 13193–13206 (2014). <https://doi.org/10.1039/c4ta01183j>
54. Y.V. Kaneti, D.P. Benu, X. Xu, B. Yulianto, Y. Yamauchi et al., Borophene: two-dimensional boron monolayer: synthesis, properties, and potential applications. *Chem. Rev.* **122**(1), 1000–1051 (2022). <https://doi.org/10.1021/acs.chemrev.1c00233>
55. B. Kiraly, X. Liu, L. Wang, Z. Zhang, A.J. Brandon et al., Borophene synthesis on Au(111). *ACS Nano* **13**(4), 3816–3822 (2019). <https://doi.org/10.1021/acs.nano.8b09339>
56. N. Liu, G. Bo, Y. Liu, X. Xu, Y. Du et al., Recent progress on germanene and functionalized germanene: preparation, characterizations, applications, and challenges. *Small* **15**(32), 1805147 (2019). <https://doi.org/10.1002/smll.201805147>
57. F. Li, W. Wei, X. Lv, B. Huang, Y. Dai et al., Evolution of the linear band dispersion of monolayer and bilayer germanene on Cu(111). *Phys. Chem. Chem. Phys.* **19**(34), 22844–22851 (2017). <https://doi.org/10.1039/c7cp03597g>
58. M.A. Pamungkas, V.K.R. Sari, Irwansyah, S.A. Putra, Abdurrouf et al., Tuning electronic structure and magnetic properties of flat stanene by hydrogenation and Al/P doping: a first principle DFT study. *Coatings* **11**(1), 47 (2021). <https://doi.org/10.3390/coatings11010047>
59. P.C. Shen, C. Su, Y. Lin, A. Chou, C. Cheng et al., Ultralow contact resistance between semimetal and monolayer semiconductors. *Nature* **593**(7858), 211–217 (2021). <https://doi.org/10.1038/s41586-021-03472-9>
60. M.J. Armstrong, D.M. Burke, T. Gabriel, C. O'Dwyer, N. Petkov et al., Carbon nanocage supported synthesis of V_2O_5 nanorods and $\text{V}_2\text{O}_5/\text{TiO}_2$ nanocomposites for Li-ion batteries. *J. Mater. Chem. A* **1**(40), 12568–12578 (2013). <https://doi.org/10.1039/c3ta12652h>
61. J. Wang, Y. Fu, H. Chen, J. Shen, Effect of supports on the supported Ni_2P catalysts prepared by the phosphidation using triphenylphosphine in liquid phase. *Chem. Eng. J.* **275**, 89–101 (2015). <https://doi.org/10.1016/J.cej.2015.03.129>
62. Y. Li, X. Yang, L. Zhu, H. Zhang, B. Chen et al., Hydrodeoxygenation of phenol as a bio-oil model compound over intimate contact noble metal- $\text{Ni}_2\text{P}/\text{SiO}_2$ catalysts. *RSC Adv.* **5**(98), 80388–80396 (2015). <https://doi.org/10.1039/c5ra11203f>
63. C.T. Crespo, The effect of the halide anion on the optical properties of lead halide perovskites. *Sol. Energy Mater. Sol. Cells* **195**, 269–273 (2019). <https://doi.org/10.1016/J.solmat.2019.03.023>
64. F. Chen, Q. Tang, T. Ma, B. Zhu, L. Wang et al., Structures, properties, and challenges of emerging 2D materials in bioelectronics and biosensors. *Infomat* **4**(5), e12299 (2022). <https://doi.org/10.1002/inf2.12299>
65. Y. Zheng, J. Liu, J. Liang, M. Jaroniec, S.Z. Qiao, Graphitic carbon nitride materials: controllable synthesis and applications in fuel cells and photocatalysis. *Energy Environ. Sci.* **5**(5), 6717–6731 (2012). <https://doi.org/10.1039/c2ee03479d>
66. C.L. Tan, X.H. Cao, X.J. Wu, Q. He, J. Yang et al., Recent advances in ultrathin two-dimensional nanomaterials. *Chem. Rev.* **117**(9), 6225–6331 (2017). <https://doi.org/10.1021/acs.chemrev.6b00558>
67. L.Y. Chen, Q. Xu, Metal-organic framework composites for catalysis. *Matter* **1**(1), 57–89 (2019). <https://doi.org/10.1016/J.matt.2019.05.018>
68. D.H. Ho, Y.Y. Choi, S.B. Jo, J. Myoung, J.H. Cho, Sensing with MXenes: progress and prospects. *Adv. Mater.* **33**(47), 2005846 (2021). <https://doi.org/10.1002/adma.202005846>
69. W.S.V. Lee, T. Xiong, X.P. Wang, J. Xue, Unraveling MoS_2 and transition metal dichalcogenides as functional zinc-ion battery cathode: a perspective. *Small Methods* **5**(1), 2000815 (2021). <https://doi.org/10.1002/smt.202000815>
70. M. Ade, H. Hillebrecht, Ternary borides Cr_2AlB_2 , Cr_3AlB_4 , and Cr_4AlB_6 : the first members of the series $(\text{CrB}_2)_n\text{CrAl}$ with $n = 1, 2, 3$ and a unifying concept for ternary borides as MAB-phases. *Inorg. Chem.* **54**(13), 6122–6135 (2015). <https://doi.org/10.1021/acs.inorgchem.5b00049>
71. Q. Tao, M. Dahlqvist, J. Lu, S. Kota, R. Meshkian et al., Two-dimensional $\text{Mo}_{1.33}\text{C}$ MXene with divacancy ordering prepared from parent 3D laminate with in-plane chemical ordering. *Nat. Commun.* **8**, 14949 (2017). <https://doi.org/10.1038/ncomms14949>
72. M. Dahlqvist, J. Lu, R. Meshkian, Q. Tao, L. Hultman et al., Prediction and synthesis of a family of atomic laminate phases with Kagome-like and in-plane chemical ordering.

- Sci. Adv. **3**(7), 1700642 (2017). <https://doi.org/10.1126/sci-adv.1700642>
73. R. Meshkian, M. Dahlqvist, J. Lu, B. Wickman, J. Halim et al., W-based atomic laminates and their 2D derivative $W_{1.33}C$ MXene with vacancy ordering. *Adv. Mater.* **30**(21), 1706409 (2018). <https://doi.org/10.1002/adma.201706409>
74. I. Persson, A. Ghazaly, Q. Tao, J. Halim, S. Kota et al., Tailoring structure, composition, and energy storage properties of MXenes from selective etching of in-plane, chemically ordered MAX phases. *Small* **14**(17), 1703676 (2018). <https://doi.org/10.1002/sml.201703676>
75. S.K. Kailasa, D.J. Joshi, J.R. Koduru, N. Malek, Review on MXenes-based nanomaterials for sustainable opportunities in energy storage, sensing and electrocatalytic reactions. *J. Mol. Liq.* **342**, 117524 (2021). <https://doi.org/10.1016/J.molliq.2021.117524>
76. M. Pogorielov, K. Smyrnova, S. Kyrylenko, O. Gogotsi, V. Zahorodna et al., MXenes—a new class of two-dimensional materials: structure, properties and potential applications. *Nanomaterials* **11**(12), 3412 (2021). <https://doi.org/10.3390/nano11123412>
77. A.K. Singh, P. Kumbhakar, A. Krishnamoorthy et al., Review of strategies toward the development of alloy two-dimensional (2D) transition metal dichalcogenides. *Iscience* **24**(12), 103532 (2021). <https://doi.org/10.1016/J.isci.2021.103532>
78. B. Ahmed, A. Ghazaly, J. Rosen, i-MXenes for energy storage and catalysis. *Adv. Funct. Mater.* **30**(47), 200894 (2020). <https://doi.org/10.1002/adfm.202000894>
79. M. Dahlqvist, A. Petruhins, J. Lu, L. Hultman, J. Rosen, Origin of chemically ordered atomic laminates (i-MAX): expanding the elemental space by a theoretical/experimental approach. *ACS Nano* **12**(8), 7761–7770 (2018). <https://doi.org/10.1021/acsnano.8b01774>
80. A. Mockute, Q. Tao, M. Dahlqvist, J. Lu, S. Calder et al., Materials synthesis, neutron powder diffraction, and first-principles calculations of $(Mo_xSc_{1-x})_2AlC$ i-MAX phase used as parent material for MXene derivation. *Phys. Rev. Mater.* **3**(11), 113607 (2019). <https://doi.org/10.1103/PhysRevMaterials.3.113607>
81. J. Thornberg, J. Halim, J. Lu, R. Meshkian, J. Palisaitis et al., Synthesis of $(V_{2/3}Sc_{1/3})_2AlC$ i-MAX phase and $V_{2-x}C$ MXene scrolls. *Nanoscale* **11**(31), 14720–14726 (2019). <https://doi.org/10.1039/c9nr02354b>
82. M. Dahlqvist, Q. Tao, J. Zhou, J. Palisaitis, P.O.Å. Persson et al., Theoretical prediction and synthesis of a family of atomic laminate metal borides with in-plane chemical ordering. *J. Am. Chem. Soc.* **142**(43), 18583–18591 (2020). <https://doi.org/10.1021/jacs.0c08113>
83. J. Zhou, J. Palisaitis, J. Halim, M. Dahlqvist, Q. Tao et al., Boridene: two-dimensional $Mo_{4/3}B_{2-x}$ with ordered metal vacancies obtained by chemical exfoliation. *Science* **373**(6556), 801–805 (2021). <https://doi.org/10.1126/science.abf6239>
84. F. Wei, S. Xu, J. Li, S. Yuan, B. Jia et al., Computational investigation of two-dimensional vanadium boride compounds for Na-ion batteries. *ACS Omega* **7**(17), 14765–14771 (2022). <https://doi.org/10.1021/acsomega.2c00134>
85. W. Xiong, X. Feng, Y. Xiao, T. Huang, X. Li et al., Fluorine-free prepared two-dimensional molybdenum boride (MBene) as a promising anode for lithium-ion batteries with superior electrochemical performance. *Chem. Eng. J.* **446**, 137466 (2022). <https://doi.org/10.1016/J.cej.2022.137466>
86. Z. Guo, J. Zhoue, Z. Sun, New two-dimensional transition metal borides for Li ion batteries and electrocatalysis. *J. Mater. Chem. A* **5**(45), 23530–23535 (2017). <https://doi.org/10.1039/c7ta08665b>
87. L.T. Alameda, P. Moradifar, Z.P. Metzger, N. Alem, R.E. Schaak, Topochemical deintercalation of Al from MoAlB: stepwise etching pathway, layered intergrowth structures, and two-dimensional MBene. *J. Am. Chem. Soc.* **140**(28), 8833–8840 (2018). <https://doi.org/10.1021/jacs.8b04705>
88. H. Zhang, H. Xiang, F. Dai, Z. Zhang, Y. Zhou et al., First demonstration of possible two-dimensional MBene CrB derived from MAB phase Cr_2AlB_2 . *J. Mater. Sci. Technol.* **34**(11), 2022–2026 (2018). <https://doi.org/10.1016/J.jmst.2018.02.024>
89. G. Bhaskar, V. Gvozdetskyi, M. Batuk, K.M. Wiaderek, Y. Sun et al., Topochemical deintercalation of Li from layered LiNiB: toward 2D MBene. *J. Am. Chem. Soc.* **143**(11), 4213–4223 (2021). <https://doi.org/10.1021/jacs.0c11397>
90. J. Wang, T.N. Ye, Y. Gong, J. Wu, N. Miao et al., Discovery of hexagonal ternary phase Ti_2InB_2 and its evolution to layered boride TiB. *Nat. Commun.* **10**, 2284 (2019). <https://doi.org/10.1038/s41467-019-10297-8>
91. S. Zhou, X.W. Yang, W. Pei, Z. Jiang, J. Zhao, MXene and MBene as efficient catalysts for energy conversion: roles of surface, edge and interface. *J. Phys. Energy* **3**(1), 012002 (2021). <https://doi.org/10.1088/2515-7655/abb6d1>
92. J. Jia, B. Li, S. Duan, Z. Cui, H. Gao et al., Monolayer MBenes: prediction of anode materials for high-performance lithium/sodium ion batteries. *Nanoscale* **11**(42), 20307–20314 (2019). <https://doi.org/10.1039/c9nr05708k>
93. D. Chen, Z. Jin, B. Zhao, Y. Wang, Q. He, MBene as a therapeutic nanoplatform for photocontrolled intratumoral retention and drug release. *Adv. Mater.* **33**(16), 2008089 (2021). <https://doi.org/10.1002/adma.202008089>
94. Y. Xiao, C. Shen, N. Hadaeghi, Quantum mechanical screening of 2D MBenes for the electroreduction of CO_2 to C1 hydrocarbon fuels. *J. Phys. Chem. Lett.* **12**(27), 6370–6382 (2021). <https://doi.org/10.1021/acs.jpclett.1c01499>
95. M. Jakubczak, A. Szuplewska, A. Rozmysłowska-Wojciechowska, A. Rosenkranz, A.M. Jastrzębska, Novel 2D MBenes—synthesis, structure, and biotechnological potential. *Adv. Funct. Mater.* **31**(38), 2103048 (2021). <https://doi.org/10.1002/adfm.202103048>
96. V. Natu, S.S. Kota, M.W. Barsoum, X-ray photoelectron spectroscopy of the MAB phases, $MoAlB$, M_2AlB_2 ($M = Cr, Fe$), Cr_3AlB_4 and their binary monoborides. *J. Eur. Ceram. Soc.* **40**(2), 305–314 (2020). <https://doi.org/10.1016/J.jeurceramsoc.2019.09.040>



97. D. Music, J.M. Schneider, The correlation between the electronic structure and elastic properties of nanolaminates. *JOM* **59**(7), 60–64 (2007). <https://doi.org/10.1007/s11837-007-0091-7>
98. M.W. Barsoume, M. Radovic, Elastic and mechanical properties of the MAX phases. *Ann Rev. Mater. Res.* **41**, 195–227 (2011). <https://doi.org/10.1146/annurev-matsci-062910-100448>
99. L.T. Alameda, C.F. Holder, J.L. Fenton, J.L. Fenton, R.E. Schaak, Partial etching of Al from MoAlB single crystals to expose catalytically active basal planes for the hydrogen evolution reaction. *Chem. Mater.* **29**(21), 8953–8957 (2017). <https://doi.org/10.1021/acs.chemmater.7b02511>
100. H. Zhang, F.Z. Dai, H. Xiang, X. Wang, Z. Zhang et al., Phase pure and well crystalline Cr₂AlB₂: a key precursor for two-dimensional CrB. *J. Mater. Sci. Technol.* **35**(8), 1593–1600 (2019). <https://doi.org/10.1016/J.jmst.2019.03.031>
101. J. Wang, M. Khazaei, M. Arai, N. Umezawa, T. Tada et al., Semimetallic two-dimensional TiB₁₂: improved stability and electronic properties tunable by biaxial strain. *Chem. Mater.* **29**(14), 5922–5930 (2017). <https://doi.org/10.1021/acs.chemmater.7b01433>
102. M.A. Ali, M.M. Hossain, M.M. Uddin, A.K.M.A. Islam, D. Jana et al., DFT insights into new B-containing 212 MAX phases: Hf₂AB₂. (A = In, Sn). *J. Alloys Compd.* **860**, 158408 (2021). <https://doi.org/10.1016/J.jallcom.2020.158408>
103. R. Khaledialidusti, M. Khazaei, V. Wang, N. Miao, C. Si et al., Exploring structural, electronic, and mechanical properties of 2D hexagonal MBenes. *J. Phys. Condens. Matter* **33**(15), 155503 (2021). <https://doi.org/10.1088/1361-648X/abb0e>
104. P. Li, R. Zhou, X.C. Zeng, Computational analysis of stable hard structures in the Ti-B system. *ACS Appl. Mater. Interfaces* **7**(28), 15607–15617 (2015). <https://doi.org/10.1021/acsami.5b04332>
105. Z. Liu, E. Wu, J. Wang, Y. Qian, H. Xiang et al., Crystal structure and formation mechanism of (Cr_{2/3}Ti_{1/3})₃AlC₂. MAX Phase. *Acta Mater.* **73**, 186–193 (2014). <https://doi.org/10.1016/J.actamat.2014.04.006>
106. E.N. Caspi, P. Chartier, F. Porcher, F. Damay, T. Cabioch et al., Ordering of (Cr, V) layers in nanolamellar (Cr_{0.5}V_{0.5})_{n+1}AlC_n compounds. *Mater. Res. Lett.* **3**(2), 100–106 (2015). <https://doi.org/10.1080/21663831.2014.975294>
107. Q. Tao, J. Lu, M. Dahlqvist, A. Mockute, S. Calder et al., Atomically layered and ordered rare-earth i-MAX phases: a new class of magnetic quaternary compounds. *Chem. Mater.* **31**(7), 2476–2485 (2019). <https://doi.org/10.1021/acs.chemmater.8b05298>
108. H. Pazniak, M. Stevens, M. Dahlqvist, B. Zingsem, L. Kibkalo et al., Phase stability of nanolaminated epitaxial (Cr_{1-x}Fe_x)₂AlC MAX phase thin films on MgO(111) and Al₂O₃ (0001) for use as conductive coatings. *ACS Appl. Nano Mater.* **4**(12), 13761–13770 (2021). <https://doi.org/10.1021/acsanm.1c03166>
109. K. Sobolev, H. Pazniak, M. Farle, V. Rodionova, U. Wiedwald et al., Synthesis, phase purification and magnetic characterization of the (Cr_{1-x}, M_{n-x})₂AlC MAX-phase. *J. Mater. Chem. C* **9**(46), 16516–16522 (2021). <https://doi.org/10.1039/d1tc03092b>
110. J. Yang, R. Liu, N. Jia, K. Wu, X. Fu et al., Novel W-based in-plane chemically ordered (W_{2/3}R_{1/3})₂AlC (R = Gd, Tb, Dy, Ho, Er, Tm and Lu) MAX phases and their 2D W_{1.33}C MXene derivatives. *Carbon* **183**, 76–83 (2021). <https://doi.org/10.1016/J.carbon.2021.07.010>
111. J. Yang, G. Yao, S. Sun, Z. Chen, S. Yuan et al., Structural, magnetic properties of in-plane chemically ordered (Mo_{2/3}R_{1/3})₂AlC (R = Gd, Tb, Dy, Ho, Er and Y) MAX phase and enhanced capacitance of Mo_{1.33}C MXene derivatives. *Carbon* **179**, 104–110 (2021). <https://doi.org/10.1016/J.carbon.2021.03.062>
112. H. Zhang, F. Dai, H. Xiang, Z. Zhang, Y. Zhou et al., Crystal structure of Cr₄AlB₄: a new MAB phase compound discovered in Cr-Al-B system. *J. Mater. Sci. Technol.* **35**(4), 530–534 (2019). <https://doi.org/10.1016/J.jmst.2018.10.006>
113. J. Lu, S. Kota, M.W. Barsoum, L. Hultman, Atomic structure and lattice defects in nanolaminated ternary transition metal borides. *Mater. Res. Lett.* **5**(4), 235–241 (2017). <https://doi.org/10.1080/21663831.2016.1245682>
114. P. Chai, S.A. Stoian, X. Tan, P.A. Dube, M. Shatruk et al., Investigation of magnetic properties and electronic structure of layered-structure borides AlT₂B₂ (T = Fe, Mn, Cr) and AlFe_{2-x}Mn_xB₂. *J. Solid State Chem.* **224**, 52–61 (2015). <https://doi.org/10.1016/J.jssc.2014.04.027>
115. J. Liu, S. Li, B. Yao, S. Hu, J. Zhang et al., Rapid synthesis and characterization of a nanolaminated Fe₂AlB₂ compound. *J. Alloys Compd.* **766**, 488–497 (2018). <https://doi.org/10.1016/J.jallcom.2018.06.352>
116. K. Kadas, D. Iusan, J. Hellsvik, J. Cedervall, M. Sahlberg et al., AlM₂B₂ (M = Cr, Mn, Fe Co, Ni): a group of nanolaminated materials. *J. Phys. Condens. Matter* **29**(15), 155402 (2017). <https://doi.org/10.1088/1361-648X/aa602a>
117. S. Kota, M. Agne, E. Zapata-Solvas, O. Dezellus, D. Lopez et al., Elastic properties, thermal stability, and thermodynamic parameters of MoAlB. *Phys. Rev. B* **95**(14), 144108 (2017). <https://doi.org/10.1103/PhysRevB.95.144108>
118. S. Kota, E. Zapata-Solvas, A. Ly, J. Lu, O. Elkassabany et al., Synthesis and characterization of an alumina forming nanolaminated boride: MoAlB. *Sci. Rep.* **6**, 26475 (2016). <https://doi.org/10.1038/srep26475>
119. F.Z. Dai, H. Xiang, Y. Sun, Y. Zhou, M₂M'AlB₄ (M = Mn, Fe Co, M' = Cr, Mo, W): theoretical predicted ordered MAB phases with Cr₃AlB₄ crystal structure. *J. Mater. Sci. Technol.* **35**(7), 1432–1438 (2019). <https://doi.org/10.1016/J.jmst.2019.03.005>
120. M. Fan, Y. Wen, D. Ye, Z. Jin, P. Zhao et al., Acid-responsive H₂-releasing 2D MgB₂ nanosheet for therapeutic synergy and side effect attenuation of gastric cancer chemotherapy. *Adv. Healthc. Mater.* **8**(13), 1900157 (2019). <https://doi.org/10.1002/adhm.201900157>
121. Z. Jin, D. Chen, P. Zhao, Y. Wen, M. Fan et al., Coordination-induced exfoliation of monolayer Bi-anchored MnB₂ nanosheets for multimodal imaging-guided photothermal

- therapy of cancer. *Theranostics* **10**(4), 1861–1872 (2020). <https://doi.org/10.7150/thno.39715>
122. N. Chen, H. Huang, Z. Xu, Y. Xie, D. Xiong et al., From high-yield Ti_3AlCN ceramics to high-quality Ti_3CNT_x MXenes through eliminating Al segregation. *Chin. Chem. Lett.* **31**(4), 1044–1048 (2020). <https://doi.org/10.1016/J.ccllet.2019.10.004>
123. L.L. Li, X. Chang, X.Y. Lin, Z. Zhao, J. Gong, Theoretical insights into single-atom catalysts. *Chem. Soc. Rev.* **49**(22), 8156–8178 (2020). <https://doi.org/10.1039/d0cs00795a>
124. H.Y. Zhuo, X. Zhang, J.X. Liang, Q. Yu, H. Xiao et al., Theoretical understandings of graphene-based metal single-atom catalysts: stability and catalytic performance. *Chem. Rev.* **120**(21), 12315–12341 (2020). <https://doi.org/10.1021/acs.chemrev.0c00818>
125. M.D. Hossain, Z.J. Liu, M.H. Zhuang, X. Yan, G. Xu et al., Rational design of graphene-supported single atom catalysts for hydrogen evolution reaction. *Adv. Energy Mater.* **9**(10), 1803689 (2019). <https://doi.org/10.1002/aenm.201803689>
126. Y.Y. Qiao, J.Y. Cui, F.R. Qian, X. Xue, X. Zhang et al., Pt_3Fe Nanoparticles on B, N-codoped carbon as oxygen reduction and pH-universal hydrogen evolution electrocatalysts. *ACS Appl. Nano Mater.* **5**(1), 318–325 (2022). <https://doi.org/10.1021/acsanm.1c03046>
127. L. Rakocevic, I.S. Simatovic, A. Maksic, V. Rajić, S. Štrbac et al., PtAu nanoparticles supported by reduced graphene oxide as a highly active catalyst for hydrogen evolution. *Catalysts* **12**(1), 43 (2022). <https://doi.org/10.3390/catal12010043>
128. H.J. Chun, V. Apaja, A. Clayborne, K. Honkala, J. Greeley, Atomistic insights into nitrogen-cycle electrochemistry: a combined DFT and kinetic Monte Carlo analysis of NO electrochemical reduction on Pt(100). *ACS Catal.* **7**(6), 3869–3882 (2017). <https://doi.org/10.1021/acscatal.7b00547>
129. H.G. Shiraz, X. Crispin, M. Berggren, Transition metal sulfides for electrochemical hydrogen evolution. *Int. J. Hydrog. Energy* **46**(47), 24060–24077 (2021). <https://doi.org/10.1016/J.ijhydene.2021.04.194>
130. Q.M. Yu, Y.T. Luo, S.Y. Qiu, Q. Li, Z. Cai et al., Tuning the hydrogen evolution performance of metallic 2D tantalum disulfide by interfacial engineering. *ACS Nano* **13**(10), 11874–11881 (2019). <https://doi.org/10.1021/acsnano.9b05933>
131. Q.M. Yu, Z.Y. Zhang, S.Y. Qiu, Y. Luo, F. Yang et al., A Ta– TaS_2 monolith catalyst with robust and metallic interface for superior hydrogen evolution. *Nat. Commun.* **12**, 6051 (2021). <https://doi.org/10.1038/s41467-021-26315-7>
132. S. Chandrasekaran, C.L. Zhang, Y.Q. Shu, H. Wang, S. Chen et al., Advanced opportunities and insights on the influence of nitrogen incorporation on the physico-/electro-chemical properties of robust electrocatalysts for electrocatalytic energy conversion. *Coord. Chem. Rev.* **449**, 214209 (2021). <https://doi.org/10.1016/J.ccr.2021.214209>
133. B. Ding, W.J. Ong, J.Z. Jiang, X. Chen, N. Li, Uncovering the electrochemical mechanisms for hydrogen evolution reaction of heteroatom doped M_2C MXene ($\text{M} = \text{Ti}, \text{Mo}$) Appl. Surf. Sci. **500**, 143987 (2020). <https://doi.org/10.1016/J.apsusc.2019.143987>
134. J.Z. Jiang, Y.L. Zou, Arramel, F. Li, J. Wang et al., Intercalation engineering of MXenes towards highly efficient photo(electrocatalytic) hydrogen evolution reactions. *J. Mater. Chem. A* **9**(43), 24195–24214 (2021). <https://doi.org/10.1039/d1ta07332j>
135. S. Jin, Z.H. Shi, H.J. Jing, L. Wang, Q. Hu et al., Mo_2C -MXene/CdS heterostructures as visible-light photocatalysts with an ultrahigh hydrogen production rate. *ACS Appl. Energy Mater.* **4**(11), 12754–12766 (2021). <https://doi.org/10.1021/acsaeam.1c02456>
136. Y.Y. Cao, G.B. Zhou, X.L. Chen, Q. Qiao, C. Zhao et al., Hydrogen peroxide synthesis on porous graphitic carbon nitride using water as a hydrogen source. *J. Mater. Chem. A* **8**(1), 124–137 (2020). <https://doi.org/10.1039/c9ta08103h>
137. X.Z. Chen, W.J. Ong, X.J. Zhao, P. Zhang, N. Li, Insights into electrochemical nitrogen reduction reaction mechanisms: combined effect of single transition-metal and boron atom. *J. Energy Chem.* **58**, 577–585 (2021). <https://doi.org/10.1016/J.jchem.2020.10.043>
138. S. Ji, J.X. Zhao, Boron-doped graphene as a promising electrocatalyst for NO electrochemical reduction: a computational study. *New J. Chem.* **42**(19), 16346–16353 (2018). <https://doi.org/10.1039/c8nj03279c>
139. S.B. Tang, Q. Dang, T.Y. Liu, S. Zhang, Z. Zhou et al., Realizing a not-strong-not-weak polarization electric field in single-atom catalysts sandwiched by boron nitride and graphene sheets for efficient nitrogen fixation. *J. Am. Chem. Soc.* **142**(45), 19308–19315 (2020). <https://doi.org/10.1021/jacs.0c09527>
140. X. Sun, J. Zheng, Y. Gao, C. Qiu, Y. Yan et al., Machine-learning-accelerated screening of hydrogen evolution catalysts in MBenes materials. *Appl. Surf. Sci.* **526**, 146522 (2020). <https://doi.org/10.1016/J.apsusc.2020.146522>
141. B. Li, Y. Wu, N. Li, X. Chen, X. Zeng et al., Single-metal atoms supported on MBenes for robust electrochemical hydrogen evolution. *ACS Appl. Mater. Interfaces* **12**(8), 9261–9267 (2020). <https://doi.org/10.1021/acsnami.9b20552>
142. X. Yang, C. Shang, S. Zhou, J. Zhao, MBenes: emerging 2D materials as efficient electrocatalysts for the nitrogen reduction reaction. *Nanoscale Horiz.* **5**(7), 1106–1115 (2020). <https://doi.org/10.1039/d0nh00242a>
143. C. He, J. Wang, L. Fu, C. Zhao, J. Huo, Associative versus dissociative mechanism: electrocatalysis of nitric oxide to ammonia. *Chin. Chem. Lett.* **33**(2), 1051–1057 (2022). <https://doi.org/10.1016/J.ccllet.2021.09.009>
144. X. Liu, X. Ge, Y. Dong, K. Fu, F. Meng et al., First-principle calculations on the structure, electronic property and catalytic activity for hydrogen evolution reaction of 2D transition-metal borides. *Mater. Chem. Phys.* **253**, 123334 (2020). <https://doi.org/10.1016/J.matchemphys.2020.123334>
145. G.P. Gao, A.P. O’Mullane, A.J. Du, 2D MXenes: a new family of promising catalysts for the hydrogen evolution reaction. *ACS Catal.* **7**(1), 494–500 (2017). <https://doi.org/10.1021/acscatal.6b02754>



146. B. Zhang, J. Zhou, Z. Guo, Q. Peng, Z. Sun et al., Two-dimensional chromium boride MBenes with high HER catalytic activity. *Appl. Surf. Sci.* **500**, 144248 (2020). <https://doi.org/10.1016/J.apsusc.2019.144248>
147. Y.W. Cheng, J.H. Dai, Y.M. Zhang, Y. Song et al., Two-dimensional, ordered, double transition metal carbides (MXenes): a new family of promising catalysts for the hydrogen evolution reaction. *J. Phys. Chem. C* **122**(49), 28113–28122 (2018). <https://doi.org/10.1021/acs.jpcc.8b08914>
148. P.K. Li, J.G. Zhu, A.D. Handoko, R. Zhang, H. Wang et al., High-throughput theoretical optimization of the hydrogen evolution reaction on MXenes by transition metal modification. *J. Mater. Chem. A* **6**(10), 4271–4278 (2018). <https://doi.org/10.1039/c8ta00173a>
149. C.Y. Ling, L. Shi, Y.X. Ouyang, J. Wang, Searching for highly active catalysts for hydrogen evolution reaction based on O-terminated mxenes through a simple descriptor. *Chem. Mater.* **28**(24), 9026–9032 (2016). <https://doi.org/10.1021/acs.chemmater.6b03972>
150. Y.Y. Liu, Y.J. Ji, Y.Y. Li, Multilevel theoretical screening of novel two-dimensional MA_2Z_4 family for hydrogen evolution. *J. Phys. Chem. Lett.* **12**(37), 9149–9154 (2021). <https://doi.org/10.1021/acs.jpcclett.1c02487>
151. Z.W. Seh, K.D. Fredrickson, B. Anasori et al., Two-dimensional molybdenum carbide (MXene) as an efficient electrocatalyst for hydrogen evolution. *ACS Energy Lett.* **1**(3), 589–594 (2016). <https://doi.org/10.1021/acsenergylett.6b00247>
152. F. Li, Q. Tang, First-principles calculations of TiB MBene monolayers for hydrogen evolution. *ACS Appl. Nano Mater.* **2**(11), 7220–7229 (2019). <https://doi.org/10.1021/acsanm.9b01718>
153. Y.W. Cheng, J.H. Dai, Y.M. Zhang, Y. Song, Transition metal modification and carbon vacancy promoted Cr_2CO_2 (MXenes): a new opportunity for a highly active catalyst for the hydrogen evolution reaction. *J. Mater. Chem. A* **6**(42), 20956–20965 (2018). <https://doi.org/10.1039/c8ta07749e>
154. P. Helmer, J. Halim, J. Zhou, R. Mahan, B. Wickman et al., Investigation of 2D boridene from first principles and experiments. *Adv. Funct. Mater.* **32**(14), 2109060 (2022). <https://doi.org/10.1002/adfm.202109060>
155. W. Yuan, L. Cheng, Y. An, H. Wu, N. Yao et al., MXene nanofibers as highly active catalysts for hydrogen evolution reaction. *ACS Sustainable Chem. Eng.* **6**(7), 8976–8982 (2018). <https://doi.org/10.1021/acssuschemeng.8b01348>
156. D.A. Kuznetsov, Z. Chen, P.V. Kumar, A. Tsoukalou, A. Kiezkowska et al., Single site cobalt substitution in 2D molybdenum carbide (MXene) enhances catalytic activity in the hydrogen evolution reaction. *J. Am. Chem. Soc.* **141**(44), 17809–17816 (2019). <https://doi.org/10.1021/jacs.9b08897>
157. C. Zamfirescu, I. Dincer, Using ammonia as a sustainable fuel. *J. Power Sources* **185**(1), 459–465 (2008). <https://doi.org/10.1016/J.jpowsour.2008.02.097>
158. Q.Y. Li, L.Z. He, C.H. Sun, X. Zhang, Computational study of MoN_2 monolayer as electrochemical catalysts for nitrogen reduction. *J. Phys. Chem. C* **121**(49), 27563–27568 (2017). <https://doi.org/10.1021/acs.jpcc.7b10522>
159. J.H. Montoya, C. Tsai, A. Vojvodic, X. Zhang, The challenge of electrochemical ammonia synthesis: a new perspective on the role of nitrogen scaling relations. *Chemsuschem* **8**(13), 2180–2186 (2015). <https://doi.org/10.1002/cssc.201500322>
160. T. Kandemir, M.E. Schuster, A. Senyshyn, M. Benrens, The haber-bosch process revisited: on the real structure and stability of “ammonia iron” under working conditions. *Angew. Chem. Int. Ed.* **52**(48), 12723–12726 (2013). <https://doi.org/10.1002/anie.201305812>
161. J.G. Chen, R.M. Crooks, L.C. Seefeldt, K.L. Bren, R.M. Bullcock et al., Beyond fossil fuel-driven nitrogen transformations. *Science* **360**(6391), aar6611 (2018). <https://doi.org/10.1126/science.aar6611>
162. F.Y. Guo, H.W. Li, M.Z. Zhou, Z. Xu, Y. Zheng et al., Electroreduction of nitrogen to ammonia catalyzed by non-noble metal catalysts under ambient conditions. *Prog. Chem.* **32**(1), 33–45 (2020). <https://doi.org/10.7536/pc190606>
163. M. Li, H. Huang, J.X. Low, C. Gao, R. Long et al., Recent progress on electrocatalyst and photocatalyst design for nitrogen reduction. *Small Methods* **3**(6), 1800388 (2019). <https://doi.org/10.1002/smtd.201800388>
164. D.R. MacFarlane, P.V. Cherepanov, J. Choi, B.H.R. Suryanto, R.Y. Hodgetts et al., A roadmap to the ammonia economy. *Joule* **4**(6), 1186–1205 (2020). <https://doi.org/10.1016/j.joule.2020.04.004>
165. G. Qing, R. Ghazfar, S.T. Jackowski, F. Habibzadeh, M.M. Ashtiani et al., Recent advances and challenges of electrocatalytic N_2 reduction to ammonia. *Chem. Rev.* **120**(12), 5437–5516 (2020). <https://doi.org/10.1021/acs.chemrev.9b00659>
166. C. Choi, S. Back, N.Y. Kim, J. Lim, Y. Kim et al., Suppression of hydrogen evolution reaction in electrochemical N_2 reduction using single-atom catalysts: a computational guideline. *ACS Catal.* **8**(8), 7517–7525 (2018). <https://doi.org/10.1021/acscatal.8b00905>
167. K. Liu, J.W. Fu, L. Zhu, X. Zhang, H. Li et al., Single-atom transition metals supported on black phosphorene for electrochemical nitrogen reduction. *Nanoscale* **12**(8), 4903–4908 (2020). <https://doi.org/10.1039/c9nr09117c>
168. W.H. Zhao, L.F. Zhang, Q.Q. Luo, Z. Hu, W. Zhang et al., Single $Mo_1(Cr_1)$ atom on nitrogen-doped graphene enables highly selective electroreduction of nitrogen into ammonia. *ACS Catal.* **9**(4), 3419–3425 (2019). <https://doi.org/10.1021/acscatal.8b05061>
169. C.N. Cui, H.C. Zhang, Z.X. Luo, Nitrogen reduction reaction on small iron clusters supported by N-doped graphene: a theoretical study of the atomically precise active-site mechanism. *Nano Res.* **13**(8), 2280–2288 (2020). <https://doi.org/10.1007/s12274-020-2847-0>
170. Y. Wan, J. Xu, R. Lv, Heterogeneous electrocatalysts design for nitrogen reduction reaction under ambient conditions. *Mater. Today* **27**, 69–90 (2019). <https://doi.org/10.1016/j.mattod.2019.03.002>

171. X. Guo, S. Lin, J. Gu, S. Zhang, Z. Chen et al., Establishing a theoretical landscape for identifying basal plane active 2D metal borides (MBenes) toward nitrogen electroreduction. *Adv. Funct. Mater.* **31**(6), 2008056 (2020). <https://doi.org/10.1002/adfm.202008056>
172. X. Zhu, X. Zhou, Y. Jing, Y. Li, Electrochemical synthesis of urea on MBenes. *Nat. Commun.* **12**, 4080 (2021). <https://doi.org/10.1038/s41467-021-24400-5>
173. Y.J. Gao, Y.Y. Cao, H. Zhuo et al., Mo₂TiC₂ MXene: a promising catalyst for electrocatalytic ammonia synthesis. *Catal. Today* **339**, 120–126 (2020). <https://doi.org/10.1016/j.cattod.2018.12.029>
174. B. Huang, N. Li, W.J. Ong, N. Zhou, Single atom-supported MXene: how single-atomic-site catalysts tune the high activity and selectivity of electrochemical nitrogen fixation. *J. Mater. Chem. A* **7**(48), 27620–27631 (2019). <https://doi.org/10.1039/c9ta09776g>
175. Z.Y. Jin, C.W. Liu, Z.C. Liu, J. Han, Y. Fang et al., Rational design of hydroxyl-rich Ti₃C₂T_x MXene quantum dots for high-performance electrochemical N₂ reduction. *Adv. Energy Mater.* **10**(22), 2000797 (2020). <https://doi.org/10.1002/aenm.202000797>
176. W. Peng, M. Luo, X.D. Xu, K. Jiang, M. Peng et al., Spontaneous atomic ruthenium doping in Mo₂CT_x MXene defects enhances electrocatalytic activity for the nitrogen reduction reaction. *Adv. Energy Mater.* **10**(25), 2001364 (2020). <https://doi.org/10.1002/aenm.202001364>
177. J.X. Xia, S.Z. Yang, B. Wang, P. Wu, I. Popovs et al., Boosting electrosynthesis of ammonia on surface-engineered MXene Ti₃C₂. *Nano Energy* **72**, 104681 (2020). <https://doi.org/10.1016/j.nanoen.2020.104681>
178. X.S. Xu, B.T. Sun, Z.Q. Liang, H. Cui, J. Tian et al., High-performance electrocatalytic conversion of N₂ to NH₃ using 1T-MoS₂ anchored on Ti₃C₂ MXene under ambient conditions. *ACS Appl. Mater. Interfaces* **12**(23), 26060–26067 (2020). <https://doi.org/10.1021/acsami.0c06744>
179. S. Qi, Y. Fan, L. Zhao, W. Li, M. Zhao et al., Two-dimensional transition metal borides as highly efficient N₂ fixation catalysts. *Appl. Surf. Sci.* **536**, 147742 (2021). <https://doi.org/10.1016/j.apsusc.2020.147742>
180. Y. Li, L. Li, R. Huang, Y. Wen, Computational screening of MBene monolayers with high electrocatalytic activity for the nitrogen reduction reaction. *Nanoscale* **13**(35), 15002–15009 (2021). <https://doi.org/10.1039/d1nr04652g>
181. J. Wang, C. He, J. Huo, L. Fu, C. Zhao, A theoretical evaluation of possible N₂ reduction mechanism on Mo₂B₂. *Adv. Theory Simul.* **4**(5), 2100003 (2021). <https://doi.org/10.1002/adts.202100003>
182. L. Lin, P. Shi, L. Fu, C. He, J. Huo et al., First-principles study of two-dimensional material Cr₂B₂ as catalyst for electrochemical nitrogen reduction reaction. *J. Electroanal. Chem.* **899**, 115677 (2021). <https://doi.org/10.1016/j.jelechem.2021.115677>
183. Y. Xiao, C. Shen, T. Long, Theoretical establishment and screening of an efficient catalyst for N₂ electroreduction on two-dimensional transition-metal borides (MBenes). *Chem. Mater.* **33**(11), 4023–4034 (2021). <https://doi.org/10.1021/acs.chemmater.1c00424>
184. C. Chen, X.R. Zhu, X.J. Wen, Y. Zhou, H. Li et al., Coupling N₂ and CO₂ in H₂O to synthesize urea under ambient conditions. *Nat. Chem.* **12**(8), 717–724 (2020). <https://doi.org/10.1038/s41557-020-0481-9>
185. B.M. Comer, P. Fuentes, C.O. Dimkpa, Y. Liu, C.A. Fernandez et al., Prospects and challenges for solar fertilizers. *Joule* **3**(7), 1578–1605 (2019). <https://doi.org/10.1016/J.joule.2019.05.001>
186. L. Celleno, Topical urea in skincare: a review. *Dermato. Therapy* **31**(6), e12690 (2018). <https://doi.org/10.1111/dth.12690>
187. H.M. Huang, J.J.W. McDou, D.J. Procter, Radical anions from urea-type carbonyls: radical cyclizations and cyclization cascades. *Angew. Chem. Int. Ed.* **57**(18), 4995–4999 (2018). <https://doi.org/10.1002/anie.201800667>
188. Y.L. Liu, X.W. Zhao, L. Ye, A novel elastic urea-melamine-formaldehyde foam: structure and properties. *Ind. Eng. Chem. Res.* **55**(32), 8743–8750 (2016). <https://doi.org/10.1021/acs.iecr.6b01957>
189. M. Seneque, F. Can, D. Duprez, X. Courtois, NO_x selective catalytic reduction (NO_x-SCR) by urea: evidence of the reactivity of HNCO, including a specific reaction pathway for NO_x reduction involving NO + NO₂. *ACS Catal.* **6**(7), 4064–4067 (2016). <https://doi.org/10.1021/acscatal.6b00785>
190. F. Barzagli, F. Mani, M. Peruzzini, From greenhouse gas to feedstock: formation of ammonium carbamate from CO₂ and NH₃ in organic solvents and its catalytic conversion into urea under mild conditions. *Green Chem.* **13**(5), 1267–1274 (2011). <https://doi.org/10.1039/c0gc00674b>
191. A.S. Alshehri, F.Q. You, Machine learning for multiscale modeling in computational molecular design. *Curr. Opin. Chem. Eng.* **36**, 100752 (2022). <https://doi.org/10.1016/j.coche.2021.100752>
192. L.T. Chen, X. Zhang, A. Chen, S. Yao, X. Hu et al., Targeted design of advanced electrocatalysts by machine learning. *Chin. J. Catal.* **43**(1), 11–32 (2022). [https://doi.org/10.1016/s1872-2067\(21\)63852-4](https://doi.org/10.1016/s1872-2067(21)63852-4)
193. K. Tran, Z.W. Ulissi, Active learning across intermetallics to guide discovery of electrocatalysts for CO₂ reduction and H₂ evolution. *Nat. Catal.* **1**(9), 696–703 (2018). <https://doi.org/10.1038/s41929-018-0142-1>
194. Z.W. Ulissi, A.J. Medford, T. Bligaard, J.K. Nørskov et al., To address surface reaction network complexity using scaling relations machine learning and DFT calculations. *Nat. Commun.* **8**, 14621 (2017). <https://doi.org/10.1038/ncomms14621>
195. B.R. Goldsmith, J. Esterhuizen, J.X. Liu, C.J. Bartel, C. Sutton, Machine learning for heterogeneous catalyst design and discovery. *AIChE J.* **64**(9), 3553–3553 (2018). <https://doi.org/10.1002/aic.16340>
196. C. Sutton, L.M. Ghiringhelli, T. Yamamoto, Y. Lysogorskiy, L. Blumenthal et al., Crowd-sourcing materials-science challenges with the NOMAD 2018 Kaggle competition. *Npj Comput. Mater.* **5**, 111 (2019). <https://doi.org/10.1038/s41524-019-0239-3>



197. S. Back, K. Tran, Z.W. Ulissi, Toward a design of active oxygen evolution catalysts: insights from automated density functional theory calculations and machine learning. *ACS Catal.* **9**(9), 7651–7659 (2019). <https://doi.org/10.1021/acscatal.9b02416>
198. F. Dinic, K. Singh, T. Dong, M. Rezazadeh, Z. Wang et al., Applied machine learning for developing next-generation functional materials. *Adv. Funct. Mater.* **31**(51), 2104195 (2021). <https://doi.org/10.1002/adfm.202104195>
199. N. Jiang, Z.W. Zhu, W.J. Xue, B.Y. Xia, B. You et al., Emerging electrocatalysts for water oxidation under near-neutral CO₂ reduction conditions. *Adv. Mater.* **34**(2), 2105852 (2022). <https://doi.org/10.1002/adma.202105852>
200. M. Majumder, H. Saini, I. Dedek, A. Schneemann, N.R. Chodankar et al., Rational design of graphene derivatives for electrochemical reduction of nitrogen to ammonia. *ACS Nano* **15**(11), 17275–17298 (2021). <https://doi.org/10.1021/acsnano.1c08455>
201. M. Steiner, M. Reiher, Autonomous reaction network exploration in homogeneous and heterogeneous catalysis. *Top. Catal.* **65**(1–4), 6–39 (2022). <https://doi.org/10.1007/s11244-021-01543-9>
202. N. Zhang, B.P. Yang, K. Liu, H. Li, G. Chen et al., Machine learning in screening high performance electrocatalysts for CO₂ reduction. *Small Methods* (2021). <https://doi.org/10.1002/smt.202100987>
203. M. Zafari, A.S. Nissimagoudar, M. Umer, G. Lee, K.S. Kim et al., First principles and machine learning based superior catalytic activities and selectivities for N₂ reduction in MBenes, defective 2D materials and 2D π -conjugated polymer-supported single atom catalysts. *J. Mater. Chem. A* **9**(14), 9203–9213 (2021). <https://doi.org/10.1039/d1ta00751c>
204. J. Yang, A computational study on the electrified Pt(111) surface by the cluster model. *Phys. Chem. Chem. Phys.* **21**(11), 6112–6125 (2019). <https://doi.org/10.1039/c8cp07241h>
205. J. Long, S. Chen, Y. Zhang, C. Guo, X. Fu et al., Direct electrochemical ammonia synthesis from nitric oxide. *Angew. Chem. Int. Ed.* **59**(24), 9711–9718 (2020). <https://doi.org/10.1002/anie.202002337>
206. Y. Xiao, C. Shen, Transition-metal borides (MBenes) as new high-efficiency catalysts for nitric oxide electroreduction to ammonia by a high-throughput approach. *Small* **17**(24), e2100776 (2021). <https://doi.org/10.1002/sml.202100776>
207. X. Liu, Z. Liu, H. Deng, Theoretical evaluation of MBenes as catalysts for the CO₂ reduction reaction. *J. Phys. Chem. C* **125**(35), 19183–19189 (2021). <https://doi.org/10.1021/acs.jpcc.1c02749>
208. M. Abdinejad, Z. Mirza, X.A. Zhang, H. Kraatz, Enhanced electrocatalytic activity of primary amines for CO₂ reduction using copper electrodes in aqueous solution. *ACS Sustain. Chem. Eng.* **8**(4), 1715–1720 (2020). <https://doi.org/10.1021/acssuschemeng.9b06837>
209. W. Choi, H. Seong, V. Efremov, Y. Lee, S. Im et al., Controlled syngas production by electrocatalytic CO₂ reduction on formulated Au-25(SR)₁₈ and PtAu₂₄(SR)₁₈ nanoclusters. *J. Chem. Phys.* **155**(1), 014305 (2021). <https://doi.org/10.1063/5.0057470>
210. A. Dutta, C.E. Morstein, M. Rahaman, M. Rahaman, A.C. López et al., Beyond copper in CO₂ electrolysis: effective hydrocarbon production on silver-nanofoam catalysts. *ACS Catal.* **8**(9), 8357–8368 (2018). <https://doi.org/10.1021/acscatal.8b01738>
211. M.H. Islam, H. Mehrabi, R.H. Coridan, O.S. Burheim, J. Hihn et al., The effects of power ultrasound (24 kHz) on the electrochemical reduction of CO₂ on polycrystalline copper electrodes. *Ultrason. Sonochem.* **72**, 105401 (2021). <https://doi.org/10.1016/j.ultsonch.2020.105401>
212. N. Rashid, M.A. Bhat, P.P. Ingole, Unravelling the chemistry of catalyst surfaces and solvents towards C–C bond formation through activation and electrochemical conversion of CO₂ into hydrocarbons over micro-structured dendritic copper. *Sustain. Energy Fuels* **6**(1), 128–142 (2021). <https://doi.org/10.1039/d1se01255j>
213. C.J. Chang, S.C. Lin, H.C. Chen, J. Wang, K.J. Zheng et al., Dynamic reoxidation/reduction-driven atomic interdiffusion for highly selective CO₂ reduction toward methane. *J. Am. Chem. Soc.* **142**(28), 12119–12132 (2020). <https://doi.org/10.1021/jacs.0c01859>
214. B.W. Zhou, P.F. Ou, N. Pant, Z. Mi, Highly efficient binary copper-iron catalyst for photoelectrochemical carbon dioxide reduction toward methane. *PNAS* **117**(3), 1330–1338 (2020). <https://doi.org/10.1073/pnas.1911159117>
215. Y.W. Li, Q. Sun, Recent advances in breaking scaling relations for effective electrochemical conversion of CO₂. *Adv. Energy Mater.* **6**(17), 1600463 (2016). <https://doi.org/10.1002/aenm.201600463>
216. A.A. Peterson, J.K. Norskov, Activity descriptors for CO₂ electroreduction to methane on transition-metal catalysts. *J. Phys. Chem. Lett.* **3**(2), 251–258 (2012). <https://doi.org/10.1021/jz201461p>
217. H. Yuan, Z. Li, J. Yang, Transition-metal diboride: a new family of two-dimensional materials designed for selective CO₂ electroreduction. *J. Phys. Chem. C* **123**(26), 16294–16299 (2019). <https://doi.org/10.1021/acs.jpcc.9b04221>
218. T. Zhang, B. Zhang, Q. Peng, J. Zhou, Z. Sun et al., Mo₂B₂ MBene-supported single-atom catalysts as bifunctional HER/OER and OER/ORR electrocatalysts. *J. Mater. Chem. A* **9**(1), 433–441 (2021). <https://doi.org/10.1039/d0ta08630d>
219. M. Yao, Z. Shi, P. Zhang, W. Ong, J. Jiang et al., Density functional theory study of single metal atoms embedded into mbene for electrocatalytic conversion of N₂ to NH₃. *ACS Appl. Nano Mater.* **3**(10), 9870–9879 (2020). <https://doi.org/10.1021/acsnm.0c01922>
220. S. Feng, N. Miao, J. Wang, Hexagonal MBene (Hf₂BO₂): a promising platform for the electrocatalysis of hydrogen evolution reaction. *ACS Appl. Mater. Interfaces* **13**(47), 56131–56139 (2021). <https://doi.org/10.1021/acsnami.1c16449>
221. G. Kucinskis, G. Bajars, J. Kleperis, Graphene in lithium ion battery cathode materials: a review. *J. Power Sources* **240**, 66–79 (2013). <https://doi.org/10.1016/j.jpowsour.2013.03.160>

222. M. Mortazavi, C. Wang, J.K. Deng, V.B. Shenoy, N.V. Medhekar, Ab initio characterization of layered MoS_2 as anode for sodium-ion batteries. *J. Power Sources* **268**, 279–286 (2014). <https://doi.org/10.1016/j.jpowsour.2014.06.049>
223. Q.L. Sun, Y. Dai, Y.D. Ma, T. Jing, W. Wei et al., Ab initio prediction and characterization of Mo_2C monolayer as anodes for lithium-ion and sodium-ion batteries. *J. Phys. Chem. Lett.* **7**(6), 937–943 (2016). <https://doi.org/10.1021/acs.jpcclett.6b00171>
224. D.D. Sun, M.S. Wang, Z.Y. Li, G. Fan, L. Fan et al., Two-dimensional Ti_3C_2 as anode material for Li-ion batteries. *Electrochem. Commun.* **47**, 80–83 (2014). <https://doi.org/10.1016/j.elecom.2014.07.026>
225. K. Persson, V.A. Sethuraman, L.J. Hardwick, Y. Hinuma, Y.S. Meng et al., Lithium diffusion in graphitic carbon. *J. Phys. Chem. Lett.* **1**(8), 1176–1180 (2010). <https://doi.org/10.1021/jz100188d>
226. Q. Tang, Z. Zhou, P. Shen, Are MXenes promising anode materials for Li ion batteries? computational studies on electronic properties and Li storage capability of Ti_3C_2 and $\text{Ti}_3\text{C}_2\text{X}_2$ ($\text{X} = \text{F}, \text{OH}$) Monolayer. *J. Am. Chem. Soc.* **134**(40), 16909–16916 (2012). <https://doi.org/10.1021/ja308463r>
227. R. Li, Y. Liu, H. Deng, C. Yu, Z. Liu, A first-principles study of MBene as anode material for Mg-ion battery. *J. Electrochem. Energy Conversi Storage* **17**(4), 041002 (2020). <https://doi.org/10.1115/1.4046615>
228. T. Bo, P.F. Liu, J. Zhang, F. Wang, B. Wang et al., Tetragonal and trigonal Mo_2B_2 monolayers: two new low-dimensional materials for Li-ion and Na-ion batteries. *Phys. Chem. Chem. Phys.* **21**(9), 5178–5188 (2019). <https://doi.org/10.1039/c9cp00012g>
229. X.H. Zha, P. Xu, Q. Huang, S. Du, R. Zhang et al., Mo_2B , an MBene member with high electrical and thermal conductivities, and satisfactory performances in lithium ion batteries. *Nanoscale Adv.* **2**(1), 347–355 (2020). <https://doi.org/10.1039/c9na00610a>
230. G. Yuan, T. Bo, X. Qi, P. Liu, Z. Huang et al., Monolayer Zr_2B_2 : a promising two-dimensional anode material for Li-ion batteries. *Appl. Surf. Sci.* **480**, 448–453 (2019). <https://doi.org/10.1016/j.apsusc.2019.02.222>
231. R. Li, Y. Wang, L.C. Xu, J. Shen, W. Zhao et al., A boron-exposed TiB_3 monolayer with a lower electrostatic-potential surface as a higher-performance anode material for Li-ion and Na-ion batteries. *Phys. Chem. Chem. Phys.* **22**(39), 22236–22243 (2020). <https://doi.org/10.1039/d0cp04204h>
232. T. Bo, P.F. Liu, J. Xu, J. Zhang, Y. Chen et al., Hexagonal Ti_2B_2 monolayer: a promising anode material offering high rate capability for Li-ion and Na-ion batteries. *Phys. Chem. Chem. Phys.* **20**(34), 22168–22178 (2018). <https://doi.org/10.1039/c8cp03362e>
233. N. Ma, T. Wang, N. Li, Y. Li, J. Fan et al., New phases of MBenes M_2B ($\text{M} = \text{Sc}, \text{Ti}, \text{and V}$) as high-capacity electrode materials for rechargeable magnesium ion batteries. *Appl. Surf. Sci.* **571**, 151275 (2022). <https://doi.org/10.1016/j.apsusc.2021.151275>
234. S. Gao, J. Hao, X. Zhang, L. Li, C. Zhang et al., Two dimension transition metal boride Y_2B_2 as a promising anode in Li-ion and Na-ion batteries. *Comput. Mater. Science* **200**, 110776 (2021). <https://doi.org/10.1016/j.commatsci.2021.110776>
235. Y. Li, T. Zhao, L. Li, R. Huang, Y. Wen, Computational evaluation of ScB and TiB MBenes as promising anode materials for high-performance metal-ion batteries. *Phys. Rev. Mater.* **6**(4), 045801 (2022). <https://doi.org/10.1103/PhysRevMaterials.6.045801>
236. L. Yu, L. Lu, X. Zhou, L. Xu, Z. Alhalili et al., Strategies for fabricating high-performance electrochemical energy-storage devices by MXenes. *ChemElectroChem* **8**(11), 1948–1987 (2021). <https://doi.org/10.1002/celec.202100385>
237. D. Cakir, C. Sevik, O. Gulseren, F.M. Peeters, Mo_2C as a high capacity anode material: a first-principles study. *J. Mater. Chem. A* **4**(16), 6029–6035 (2016). <https://doi.org/10.1039/c6ta01918h>
238. N. Yabuuchi, K. Kubota, M. Dahbi, S. Komaba, Research development on sodium-ion batteries. *Chem. Rev.* **114**(23), 11636–11682 (2014). <https://doi.org/10.1021/cr500192f>
239. M.L. Sun, Y. Yan, U. Schwingenschlogl, Beryllene: a promising anode material for Na- and K-ion batteries with ultrafast charge/discharge and high specific capacity. *J. Phys. Chem. Lett.* **11**(21), 9051–9056 (2020). <https://doi.org/10.1021/acs.jpcclett.0c02426>
240. P. Xiang, X. Chen, B. Xiao, Z.M. Wang et al., Highly flexible hydrogen boride monolayers as potassium-ion battery anodes for wearable electronics. *ACS Appl. Mater. Interfaces* **11**(8), 8115–8125 (2019). <https://doi.org/10.1021/acsami.8b22214>
241. K. Liu, B. Zhang, X. Chen, Y. Huang, P. Zhang et al., Modulating the open-circuit voltage of two-dimensional MoB MBene electrode via specific surface chemistry for Na/K ion batteries: a first-principles study. *J. Phys. Chem. C* **125**(33), 18098–18107 (2021). <https://doi.org/10.1021/acs.jpcc.1c04039>
242. L. Cai, Z. Li, S. Zhang, K. Prenger, M. Naguib et al., Safer lithium-ion battery anode based on $\text{Ti}_3\text{C}_2\text{T}_z$ MXene with thermal safety mechanistic elucidation. *Chem. Eng. J.* (2021). <https://doi.org/10.1016/j.cej.2021.129387>
243. C. Wang, H. Shou, S. Chen, S. Wei, Y. Lin et al., HCl-based hydrothermal etching strategy toward fluoride-free MXenes. *Adv. Mater.* **33**(27), 2101015 (2021). <https://doi.org/10.1002/adma.202101015>
244. J. Wu, Y. Wang, Y. Zhang, H. Meng, Y. Xu et al., Highly safe and ionothermal synthesis of Ti_3C_2 MXene with expanded interlayer spacing for enhanced lithium storage. *J. Energy Chem.* **47**, 203–209 (2020). <https://doi.org/10.1016/j.jechem.2019.11.029>
245. Y. Zhang, H. Geng, W. Wei, J. Ma, L. Chen et al., Challenges and recent progress in the design of advanced electrode materials for rechargeable Mg batteries. *Energy Storage Mater.* **20**, 118–138 (2019). <https://doi.org/10.1016/j.ensm.2018.11.033>
246. F. Liu, T. Wang, X. Liu, L. Fan, Challenges and recent progress on key materials for rechargeable magnesium batteries.



- Adv. Energy Mater. **11**(2), 2000787 (2021). <https://doi.org/10.1002/aenm.202000787>
247. W. Guo, Y. Fu, A perspective on energy densities of rechargeable Li-S batteries and alternative sulfur-based cathode materials. *Energy Environ. Mater.* **1**(1), 20–27 (2018). <https://doi.org/10.1002/eem2.12003>
248. D. Wang, F. Li, R. Lian, J. Xu, D. Kan et al., A general atomic surface modification strategy for improving anchoring and electrocatalysis behavior of $\text{Ti}_3\text{C}_2\text{T}_2$ MXene in lithium-sulfur batteries. *ACS Nano* **13**(10), 11078–11086 (2019). <https://doi.org/10.1021/acsnano.9b03412>
249. Y. Xiao, Y. Li, Z. Guo, C. Tang, B. Sa et al., Functionalized Mo_2B_2 MBenes: promising anchoring and electrocatalysis materials for lithium-sulfur battery. *Appl. Surf. Sci.* **566**, 150634 (2021). <https://doi.org/10.1016/J.apsusc.2021.150634>
250. Y. Huang, L. Lin, C. Zhang, L. Liu, Y. Li et al., Recent advances and strategies toward polysulfides shuttle inhibition for high-performance Li-S batteries. *Adv. Sci.* **9**(12), 2106004 (2022). <https://doi.org/10.1002/advs.202106004>